



universität
wien

DISSERTATION

Titel der Dissertation

„Experimental test of a Bell inequality with nonmaximally entangled states“

Verfasserin

Dipl.-Phys. Alexandra Mech

angestrebter akademischer Grad

Doktorin der Naturwissenschaften (Dr. rer. nat.)

Wien, 2012

Studienkennzahl lt. Studienblatt: A 091 411

Dissertationsgebiet lt. Studienblatt: Physik

Betreuerin / Betreuer: o.Univ.-Prof. Dr. DDr.h.c. Anton Zeilinger

Abstract

A loophole-free violation of a Bell inequality, which would refute local realism, has not been achieved yet. A violation of the Eberhard inequality using nonmaximally entangled states allows closure of the detection loophole with a detection efficiency of $2/3$. In this thesis, nonmaximally entangled photon pairs were investigated with avalanche photodiodes and highly-efficient transition-edge sensors for their implementation in a conclusive Bell experiment based on the Eberhard inequality.

The polarization-entangled photon pairs were generated in nonmaximally entangled states using a Sagnac source. For each of the produced states, a density matrix was reconstructed from measurements performed with avalanche photodiodes. An average purity of $99.26\% \pm 0.02\%$ and an average fidelity with the ideal nonmaximally entangled state $|\psi_r\rangle = \frac{1}{\sqrt{1+r^2}}(|HV\rangle + r|VH\rangle)$ of $99.01\% \pm 0.01\%$ was calculated from these density matrices. A highly-efficient detection system based on superconducting transition-edge sensors read out by superconducting quantum interference devices was installed in an adiabatic demagnetization refrigerator. An unprecedentedly high heralding efficiency was directly observed: $82.2\% \pm 0.3\%$ for a product state and $79.7\% \pm 0.2\%$ for an entangled state. The Eberhard inequality was measured with transition-edge sensors, but the results were not yet adequate for a violation. Further improvements of the setup are required.

This thesis demonstrates the key components needed for a violation of the Eberhard inequality: a highly-efficient detection system including fibre coupling and a high-purity source of nonmaximally entangled photon pairs. Together with a quantum random number generator and additional space-like separation, this work paves the way for a loophole-free Bell experiment, which is important not only to address a fundamental question but also for applications such as device-independent quantum key distribution and certification of device-independent randomness.

Zusammenfassung

Eine den lokalen Realismus widerlegende schlupflochfreie Verletzung einer Bell-Ungleichung wurde bisher nicht erreicht. Eine Verletzung der Eberhard-Ungleichung mit nicht maximal verschränkten Zuständen ermöglicht das Schließen des Detektionsschlupflochs mit einer Detektionseffizienz von $2/3$. In dieser Arbeit wurden Photonenpaare in nicht maximal verschränkten Zuständen mit Lawinenphotodioden und hocheffizienten supraleitenden Phasenübergangsthermistoren, sogenannten “transition-edge sensors” (TESs), für ihre Verwendung in einem endgültigen, auf der Eberhard-Ungleichung basierten Bell-Experiment untersucht.

Polarisationsverschränkte Photonenpaare wurden in einer Sagnac-Quelle in nicht maximal verschränkten Zuständen hergestellt. Für jeden der erzeugten Zustände wurde aus Messungen mit Lawinenphotodioden eine Dichtematrix rekonstruiert. Eine durchschnittliche Reinheit von $99.26\% \pm 0.02\%$ und eine durchschnittliche Güte für einen idealen, nicht maximal verschränkten Zustand $|\psi_r\rangle = \frac{1}{\sqrt{1+r^2}}(|HV\rangle + r|VH\rangle)$ von $99.01\% \pm 0.01\%$ wurden aus diesen Dichtematrizen berechnet. Ein hocheffizientes Detektionssystem basierend auf supraleitenden Phasenübergangsthermistoren, die von supraleitenden Quanteninterferometern ausgelesen werden, wurde in einem adiabatischen Entmagnetisierungskryostat installiert. Eine beispiellos hohe Ankündigungseffizienz von $82.2\% \pm 0.3\%$ für einen Produktzustand und $79.7\% \pm 0.2\%$ für einen verschränkten Zustand wurde direkt beobachtet. Die Eberhard-Ungleichung wurde mit supraleitenden Phasenübergangsthermistoren gemessen, jedoch waren die Ergebnisse noch nicht ausreichend für eine Verletzung. Weitere Verbesserungen des Aufbaus sind erforderlich.

Diese Arbeit demonstriert die Schlüsselkomponenten, die für die Verletzung der Eberhard-Ungleichung benötigt werden: ein hocheffizientes Detektionssystem einschließlich des Einkoppelns in Fasern und eine Quelle hochreiner, nicht maximal verschränkter Zustände. Zusammen mit einem Quantenzufallsgenerator und

IV

zusätzlicher räumlicher Trennung ebnet diese Arbeit den Weg für ein endgültiges, schlupflochfreies Bell-Experiment, das nicht nur als grundsätzliche Fragestellung wichtig ist, sondern auch für Anwendungen wie geräteunabhängige Quantenschlüsselverteilung und die Zertifizierung von geräteunabhängiger Zufälligkeit.

Contents

1	Introduction	1
2	Historical background	3
2.1	EPR	3
2.2	Bell	4
2.3	Previous Bell experiments	6
2.4	Loopholes	8
2.5	Proposals for a conclusive Bell experiment	12
3	Theory of nonmaximally entangled states	17
3.1	Hardy	17
3.2	Eberhard's paper	18
3.3	Comparison to the CH inequality	20
3.4	"Diagonal" basis for pure nonmaximally entangled states	21
3.5	Nonmaximally entangled states produced by a Sagnac source	24
3.6	State optimization	25
4	Tools and techniques	29
4.1	Spontaneous parametric downconversion	29
4.2	Sagnac source	31
4.3	Experimental characterization	33
4.4	Detection system based on transition-edge sensors	35

5	Characterization of nonmaximally entangled states	49
5.1	State preparation	49
5.2	Eberhard with fair sampling	49
5.3	State tomography	51
5.4	Summary	62
6	Highly-efficient heralding	65
6.1	Experimental setup	66
6.2	Results	69
7	Eberhard inequality with transition-edge sensors	71
7.1	Detection system	71
7.2	Experimental setup	74
7.3	Results	74
8	Outlook	79
8.1	Experimental losses	79
8.2	Space-like separation	80
8.3	Conclusion	80
A	Appendix	83
	References	95
	Acknowledgments	109

Introduction

Entanglement is one of the most astonishing features of quantum mechanics. The formalism of quantum mechanics implies that two separate particles can be described as a single entity. This is reflected in correlations between the two, which are not included in the framework of classical physics. At the beginning of the 20th century, Einstein and his coworkers (EPR) found these implications of the then new theory a sign of its incompleteness assuming locality and reality [1]. Today, thanks to John Bell, we have a tool at hand which allows tests of local realistic theories even those including additional parameters unknown to us, called local hidden variables [2]. Since this formulation of the EPR-paradox in the mathematical language of an inequality, it is essential to perform an experiment fulfilling all of the assumptions made in the derivation of the inequality. Only then a violation of the Bell inequality definitely disproves local realism as the correct description of nature; at the same time it favors the quantum mechanical description. Tests of Bell's inequality have exhibited a violation from the early days on [3–11]. Due to experimental imperfections, the assumptions of the derivation have not been ensured experimentally, but were assumed to be valid. A test of Bell's inequality that satisfies the assumptions of its derivation is still missing. Since it is not only a deeply fundamental question but also the basis on which the security of quantum key distribution (QKD) [12–14] and the certification of device-independent randomness rely [15], it is important and topical to perform a conclusive Bell experiment.

One of these fundamental assumptions is that whatever happens to a particle at location A should be independent of the fate of a particle at a different location B. Another assumption is that the choice of the measurement setting at each location is random and independent of the other location and its choice and of the emission of the entangled pair. To guarantee this independence proper space-like separation between the events has to be established. If these assumptions are not complied with,

the experiment is said to have the locality loophole and the freedom-of-choice loophole open. Because of the low interaction of photons with the environment, it is relatively easy to close these loopholes using photons [16–18], but for the contrary reason it is very difficult with non-photon systems. In turn, non-photon systems are detected very efficiently, up to 100%, whereas photons suffer from low overall detection efficiency. For a violation of the Bell inequality without additional assumptions the overall detection efficiency must exceed 83% for maximally entangled states as the well known Bell states [19]. If this is not the case, the experiment is said to have the detection loophole open. Only four experiments using ions [20], Josephson qubits [21] and atoms [22, 23] were able to attain a sufficiently high detection efficiency to exclude local realistic theories that make use of low detection efficiency. Thanks to new detectors based on superconducting materials it has now become possible to detect photons very efficiently as well [24–26]. Still, including optical losses due to reflection and absorption as well as coupling or collection losses, the bound of 83% seems to be out of reach. Possibly surprisingly, for less entangled states a lower bound for detection efficiency of $2/3$ was found by Eberhard [27].

The groundwork for a definite test of local realism using polarization-entangled photon pairs is done in this thesis. The preparation of pure nonmaximally entangled states using a Sagnac source [28] is investigated. A detection system based on transition-edge sensors set up in an adiabatic demagnetization refrigerator is presented. An unprecedentedly high heralding efficiency of 82% was achieved with photon pairs produced in the Sagnac source and detected with transition-edge sensors. This demonstrates the potential overall detection efficiency of the setup, surpassing the required detection efficiency of $2/3$ that would disprove local realism.

Historical background

The history of Bell experiments is already about 50 years old, but a conclusive, loophole-free Bell experiment is topical down to the present day. All experiments performed so far can be explained by local realistic theories. The motivation of this field of research dates back to Einstein who co-founded but also challenged quantum mechanics.

2.1 EPR

In 1935, Einstein, Podolsky and Rosen published their famous paper [1], asking if “quantum-mechanical description of physical reality [can] be considered complete”. According to the authors, a complete theory is defined as one describing all elements of reality with the definition of an element of reality as the possibility of predicting with certainty the value of a physical quantity without disturbing the system. They then describe a quantum mechanical state of two particles, entangled¹ in the degrees of freedom of position and momentum. After the interaction creating the entanglement, there is no further interaction. Depending on which quantity, position or momentum, is measured on the first particle, the respective quantity is determined for the second one as well. Since the particles do not interact anymore, the values for both quantities can in principle be obtained without disturbing the second system. In agreement with the above definition both quantities are elements of reality. This in turn contradicts, that two noncommuting operators, as position or momentum are, cannot have simultaneous reality. Since the quantum mechanical entangled two-particle state disagrees with the introduced criteria they argue that quantum mechanics should be considered incomplete. The paper is known as EPR paper or is referred to as the EPR paradox.

¹ the state was later called “verschränkt” in German or “entangled” in English by Schrödinger [29]

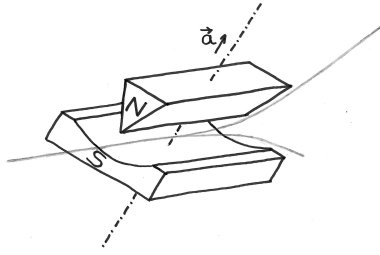


Fig. 2.1: Stern-Gerlach. The apparatus is oriented in direction \vec{a} . A spin- $\frac{1}{2}$ particle entering the device has two possible outputs, either up or down. The component $\vec{a} \cdot \vec{\sigma}$ of the spin $\vec{\sigma}$ is measured.

In 1951, Bohm reformulated their argument for discrete variables, the spin entanglement of two spin- $\frac{1}{2}$ particles, which facilitates the mathematical treatment [30].

2.2 Bell

In 1964, Bell mathematically formulated EPR's idea of completing quantum mechanics with additional variables [2]. These variables are called hidden variables, because they either cannot be measured with present technology or are in principle not accessible by any measurement. Based on realism and locality, he derived an inequality valid for, as it was shown later, both deterministic and stochastic hidden variable theories [31, 32], but which is violated by quantum mechanics. This inequality, known as the Bell inequality, allows testing in experiment, whether nature behaves according to local realistic hidden variable theories or refutes the concept of local realism, confirming the quantum mechanical predictions.

The physical example Bell employed is a system of two spin- $\frac{1}{2}$ particles in a singlet spin state introduced by Bohm. Both particles are moving in opposite directions. The spin component in the direction of the vector \vec{a} is measured by a Stern-Gerlach magnet aligned along \vec{a} (Fig. 2.1). In this thesis, pairs of polarization-entangled photons are used, which are either measured by linear polarizers or a half-wave plate (HWP) and a two-channel polarizer. The transmitted polarization is described by the angle α with respect to the horizontal Cartesian axis. A scheme of such a setup is shown in Fig 2.2. It is common to call the first observer Alice and the second Bob. Further arguments are independent of the physical system, so that the measurement parameters are called a_i and b_j in this section. Since two outcomes are possible for the measurement of each particle, one outcome is assigned the value 1 and the other the value -1 . Based on Einstein's argument additional variables λ

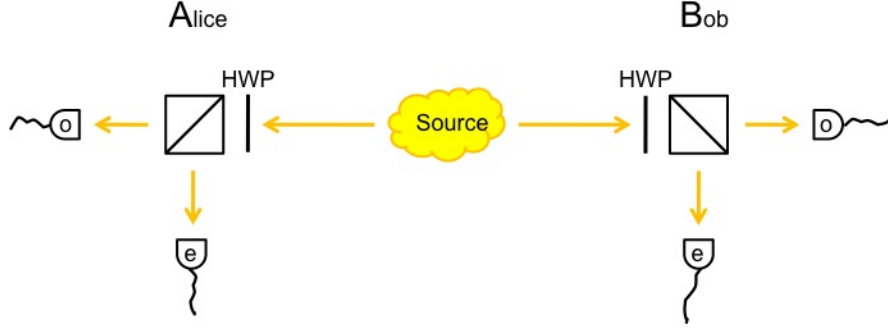


Fig. 2.2: Scheme of a Bell experiment using photons with two-channel polarizers. A source emits photons in different directions, where at the two locations of Alice and Bob the polarization of each photon is analyzed by a half-wave plate (HWP) and a polarizing beam splitter (PBS). Depending on which of the two possible outputs of the PBS the photon is leaving the corresponding detector is clicking.

are introduced to complete the description of the state. A very important assumption in the derivation is locality. It is explicitly assumed that the orientation a of Alice's apparatus does not influence Bob's measurement result B and vice versa (setting independence). The results $A(a_i, \lambda) = \pm 1$ and $B(b_j, \lambda) = \pm 1$ depend only on the orientation of the corresponding measurement device and the hidden variables λ . Hereby it is implicitly assumed that Bob's measurement outcome B is also independent of Alice's measurement result A (outcome independence) and the other way around. The independence of the choice of the measurement setting from the hidden variables (freedom-of-choice) is implicitly assumed as well, resulting in a probability distribution of hidden variables $\int \rho(\lambda) d\lambda = 1$, independent of the settings a and b [18, 31, 33]. The expectation value of the product of the two measurement outcomes is then

$$P(a_i, b_j) = \int A(a_i, \lambda) B(b_j, \lambda) \rho(\lambda) d\lambda. \quad (2.1)$$

Further implicit assumptions of Bell are perfect detection efficiency and perfect correlation for specific measurement parameters [34]. An inequality without the last assumption was derived 1969 by Clauser, Horne, Shimony and Holt [34] and is often called CHSH inequality. A simplified derivation starts with the relation

$$(A(a_1, \lambda) + A(a_2, \lambda))B(b_1, \lambda) + (A(a_2, \lambda) - A(a_1, \lambda))B(b_2, \lambda) = \pm 2. \quad (2.2)$$

After taking the absolute value and integration over the hidden variables λ using the above probability distribution for λ , the triangle inequality is applied. Replacing the

terms of the inequality with Eq. (2.1) results in the CHSH inequality

$$S = |P(a_1, b_1) + P(a_2, b_1) + P(a_2, b_2) - P(a_1, b_2)| \leq 2. \quad (2.3)$$

This inequality is violated by quantum mechanics. The maximal value of the Bell parameter $S = 2\sqrt{2} = 2.828$ is achieved using a maximally entangled state.

In 1974, Clauser and Horne developed a new form of the Bell inequality without any assumptions about detection efficiency [31]. The inequality comprises probabilities p_{12} for counts coincidentally detected at both detectors at setting a or a' for Alice and b or b' for Bob, the coincident counts, as well as the probability p_1 or p_2 for counts detected only by one of the detectors at setting a' for Alice or at b for Bob, the single counts. The upper threshold of the so-called CH inequality

$$-1 \leq p_{12}(a, b) - p_{12}(a, b') + p_{12}(a', b) + p_{12}(a', b') - p_1(a') - p_2(b) \leq 0 \quad (2.4)$$

allows the use of the measured number of counts instead of probabilities. Without additional assumptions this inequality is only violated, if the overall detection efficiency is sufficiently high. The maximal value of a violation using a maximally entangled state is $\frac{\sqrt{2}-1}{2} = 0.2071$.

The CHSH and the CH inequality are equivalent and have the same threshold for detection efficiency for maximally entangled states of $2(\sqrt{2}-1) = 82.84\%$ [19]. In 1993, Eberhard showed that the threshold for a violation of a Bell inequality using nonmaximally entangled states is lower than for maximally entangled states [27]. The threshold of $2/3$ Eberhard calculated numerically was later confirmed analytically by Larsson and Semitecolos [35]. In the same year as Eberhard, Hardy proposed a test of nonlocality using nonmaximally entangled states without an inequality [36]. He formulated contradictions of predicted values, similar to the ‘‘all or nothing’’ test of Greenberger, Horne and Zeilinger (GHZ) [37]. In a real experiment of Hardy’s test, an inequality has to be evaluated, that is equivalent to the Eberhard and to the CH inequality [38, 39].

2.3 Previous Bell experiments

A very good overview of the early experimental tests of a Bell inequality is given by Clauser and Shimony [40]; the overview given by Weihs is going beyond 1978 [41].

Wu and Shaknov measured correlations of γ -photons from electron positron annihilation in 1950 [3]. Seven years later their experiment was interpreted by Bohm and Aharonov as the first experimental proof of the EPR paradox [42].

In 1967, Kocher and Commins used photons emitted in an atomic cascade of calcium to show polarization correlations as an example of EPR [4]. Freedman and Clauser first measured a violation of a Bell inequality with such a photon cascade in 1972 [5]. The next experiment with a photon cascade of mercury by Holt and Pipkin in 1973 did not violate a Bell inequality [43, 44]. However, when the same transition mechanism and excitation were used by Clauser in 1976, it did [6]. Clauser suggested the birefringence of the glass of the bulb containing the mercury vapor due to stress as an explanation for Holt and Pipkin's result. A further measurement with a photon cascade of mercury by Fry and Thompson in 1976 using a different excitation technique confirmed Clauser's violation [7].

The experiment with photon pairs produced by positronium annihilation by Faraci et al. in 1974 failed to violate a Bell inequality [45], but a similar experiment a year later by Kasday, Ullman and Wu was again in agreement with quantum mechanical predictions violating a Bell inequality [8]. A suggested explanation was degradation of correlations over distance, especially for distances larger than the coherence length of the γ -photons. To test this hypothesis photon pairs produced by positronium annihilation were separated up to twenty times the coherence length (2.5 m) by Wilson, Lowe and Butt in 1976 [9] and by ten times the coherence length by Bruno, D'Agostino and Maroni in 1977 [10]. However, the suggested degradation was not observed in these experiments.

In 1976, instead of the usual polarization correlations Laméhi-Rachti and Mittag measured spin correlations of proton pairs prepared by scattering, in agreement with quantum mechanical predictions [11].

A series of experiments using photons emitted in a cascade of calcium were performed by Aspect and colleagues in 1981 and 1982 violating Bell's inequality [16, 46, 47]. Since all previous experiments needed additional assumptions for a violation, an important step towards an experiment free of such assumptions, a loophole-free Bell experiment, was taken by deploying time-varying analyzers to ensure that the measurement events were space-like separated [16]. This experiment addressed the locality loophole for the first time, although the switching was not random. More details can be found in Sec. 2.4.1.

Perrie et al. for the first time violated the Bell inequality with photons emitted simultaneously in a true second-order two-photon decay process of deuterium, in 1985 [48]. Two years later Haji-Hassan et al. from the same group of Kleinpopp experimentally negated enhancement in the detection process, motivated by criticism on the "no-enhancement" assumption used in all experiments because of the low overall detection efficiency [49].

In the following years a new system for the production of photon pairs became dominant: the spontaneous parametric downconversion (SPDC), which is explained in more detail in Sec. 4.1. In 1988, the first two Bell experiments using SPDC were carried out by Shih and Alley [50] and Ou and Mandel [51]. Many more followed, also using other entangled degrees of freedom, such as phase and momentum by Rarity and Tapster in 1990 [52], time and energy by Brendel and coworkers in 1992 [53] and Kwiat et al. in 1993 [54].

Since all these experiments do not fulfill the assumptions of the derivation of Bell's inequality, they cannot refute local realism [55].

2.4 Loopholes

Setting and outcome independence, freedom of choice of the measurement setting and perfect detection efficiency are assumed in the derivation of Bell's inequality. For a conclusive Bell experiment, all these assumptions must be fulfilled in a single experiment, whereby it was shown that for maximally entangled states instead of a perfect detection efficiency a detection efficiency above 83% [19] and for nonmaximally entangled states above $2/3$ is sufficient [27]. Since these assumptions have not been able to be met yet, all experiments performed to the present day must assume locality, freedom of choice, fair sampling or combinations of them. Which additional assumptions are needed depends on the specific setup and each opens a loophole. The most prominent loopholes are the locality loophole, the freedom-of-choice loophole and the detection loophole. All existing Bell experiments can refute only the classes of local realism that are restricted by their respective additional assumptions. Thus, until now, local realism has not been refuted conclusively by any of the performed Bell experiments.

2.4.1 Closing the locality loophole

The assumption of locality in Bell's derivation of his inequality demands that the measurement outcome on Alice's side is independent of Bob's measurement outcome and of the setting of the measurement on Bob's side and vice versa. The independence can be ensured by space-like separation of these events: The measurements at Alice and Bob have to be space-like separated, the setting of Bob has to be space-like separated from Alice and Alice's setting from Bob. Otherwise, information exchange and communication is possible. Without the necessary space-like separation, local realism cannot be excluded by a violation of the Bell inequality, only local realistic

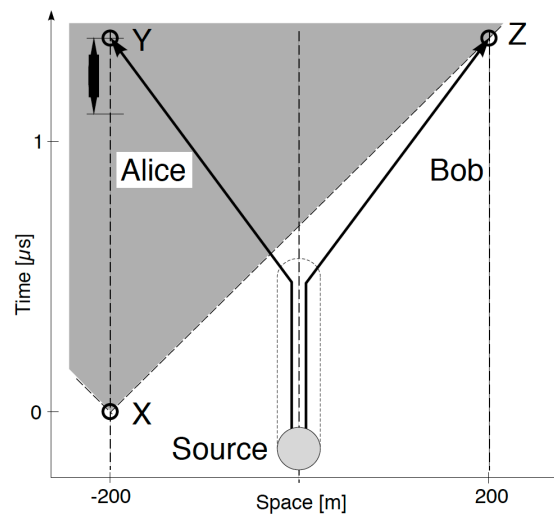


Fig. 2.3: Space-time diagram of the experiment by Weihs et al. [17]. The measurement process of Alice including the choice of a random number is indicated by the black bar. Alice's measurement process is space-like separated from Bob's measurement process. X is the earliest point in time allowing the choice of measurement setting, if the measurement process is finished at the space time points Y and Z. Figure reprinted from [17].

theories that do not exploit information exchange and communication. Such experiments leave open the locality loophole. To ensure the space-like separation, so far, photons are used. They can be transmitted over long distances, because of their low interaction with their environment.

The first experiment that provided space-like separation of the measurement events of both parties violating Bell's inequality was performed by Aspect et al. using time varying measurement settings [16]. The periodicity of the setting choice is non-ideal as the authors point out, stating that “[a] more ideal experiment with random and complete switching would be necessary for a fully conclusive argument against the whole class of supplementary-parameter theories obeying Einstein's causality.” Such an experiment was successfully performed by Weihs et al. using a physical random number generator for the choice of measurement settings and space-like separation of the setting choice of Alice and of the measurement at Alice from Bob's measurement and vice versa [17]. The corresponding space-time diagram is shown in Fig. 2.3. The results were registered on an independent computer on each side. After the experiment was finished, the tabled results with their corresponding time tags were compared to determine coincidences, and the CHSH inequality was evaluated.

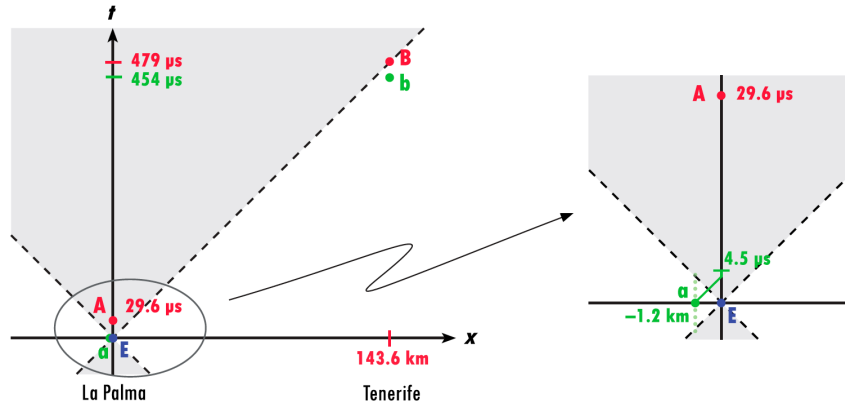


Fig. 2.4: Space-time diagram of the experiment by Scheidl et al. [18]. The random choice of the measurement setting a (b) is respectively space-like separated from the emission of the source E . A and B are measurement events. Figure reprinted from [18].

2.4.2 Closing the freedom-of-choice loophole

In the original Bell paper, nothing is explicitly said about the choice of measurement settings. However, the formulation of the probability distribution of the hidden variables $\int \rho(\lambda) d\lambda = 1$ implies that the measurement settings a and b are independent of the hidden variables λ . Bell formulated this later in more detail in Ref. [33]. There he writes, “The variable a and b can be considered to be *free*, or *random*,” which means that “they are not influenced by the variables λ .” He further argues that since “ a and b do not give any information about λ [...] the probability distribution over λ does not depend on a or b .” This again is what is already implicitly assumed with $\int \rho(\lambda) d\lambda = 1$.

To ensure this assumption, the emission of the source and both random choices of the measurement settings have to be space-like separated. This loophole was closed by choosing the measurement setting by a separate quantum random number generator for each partner and space-like separation of these two choices (a and b in Fig. 2.4) from the emission of the source (E in Fig. 2.4) in an experiment using polarization-entangled photon pairs between the Canary Islands of La Palma and Tenerife [18]. Simultaneously, the locality loophole was also closed by space-like separation of the two measurement events (A and B in Fig. 2.4) and space-like separation of the measurement event (A (B) in Fig. 2.4) on one side from the choice of the measurement setting (b (a) in Fig. 2.4) on the other side.

This experiment and, as already pointed out by others [31, 33, 56], any other experiment cannot exclude a common influence in the backward light cone of the

emission and the choice of measurement settings. In general, such an influence, called “superdeterministic” by Bell [33] or “superrealistic” by Scheidl et al. [18], cannot be tested. However, it is possible to improve on this sort of experiment by excluding larger parts of the backward light cone through separation of the choices of both settings from the source emission by greater distance. This is extendable to astronomical distances by using astronomical signals (e.g. two quasars) coming from opposite sides of the universe for the choice of measurement setting.

2.4.3 Closing the detection loophole

An implicit assumption in the derivation of Bell’s inequality is an overall detection efficiency of 100% [2]. As was shown later by Garg and Mermin, a detection efficiency of $\eta \geq 2(\sqrt{2} - 1) = 82.84\%$ is sufficient for maximally entangled states to refute local realism [19]. However, most experiments testing a Bell inequality have an overall detection efficiency lower than this limit. Either the detectors are not efficient enough or the signal is not collected sufficiently well.

Experiments that accomplished a violation of a Bell inequality without additional assumptions regarding the detection efficiency are using non-photon systems [20–23]. In 2001, the detection loophole was closed for the first time by Rowe et al. in the group of Wineland using a pair of entangled $^9\text{Be}^+$ ions [20]. Ansmann et al. in the group of Martinis violated a Bell inequality using Josephson phase qubits in 2009 [21]. Such qubits consist of electrical superconducting circuits which can be hundreds of nanometers wide and a few micrometers long and comprise trillions of electrons [57]. Although they can be called macroscopic, the circuits can be described by a single degree of freedom and show quantum behavior. In 2008, Matsukevich et al. in the group of Monroe succeeded in demonstrating heralded entanglement of two remote Yb^+ ions, which were 1 m apart, and a violation of the CHSH inequality without any assumptions on detection efficiency [22]. Recently, heralded entanglement and a Bell violation with the detection loophole closed were shown in the group of Weinfurter by Hofmann and colleagues with two ^{87}Rb atoms [23].

For photonics systems, due to the low overall detection efficiency mostly governed by the poor detection efficiencies for single-photon detectors based on silicium for the visible wavelength only a fraction of all produced pairs is detected: For some pairs both partner photons are lost, for some other pairs only one partner photon is lost, for others both are detected. To quantify the pairs where both partner photons are lost, an “event-ready” scheme has to be implemented in the experiment, where the emission of a pair is announced by another event [58]. All photonic Bell experi-

ments have to take only the detected events into account. For an evaluation of a Bell inequality only those pairs are considered that have both partners detected, which constitute the coincidences. It is assumed that those pairs are a representative and fair sample of all produced pairs. That this so-called fair sampling assumption is not evident is shown by hidden-variable models that violate the Bell inequality although they are local realistic [59, 60].

2.5 Proposals for a conclusive Bell experiment

What is a disadvantage of photons for the detection loophole is an advantage for the locality loophole: the low interaction of photons with their environment. On the other hand the contrary is true for particles. Several proposals for loophole-free Bell experiments use asymmetric systems exploiting the advantages of both systems. If the entangled system analyzed in terms of Bell inequalities is a particle entangled with a photon, the detection efficiency in the experiment is near unity for the particle and space-like separation can be achieved by transmission of the photon. The advantage of the asymmetric system is that the minimally required detection efficiency for the photon is as low as 43.7% [61, 62]. Another approach is to perform Bell measurements on a pair of separate particles entangled via entanglement swapping using the photons of the particle-photon entangled system [63]. In this section some of the various proposals for a conclusive Bell experiment using different physical systems are presented.

2.5.1 Entangled atoms

The group of Weinfurter proposed a Bell experiment with a pair of neutral atoms entangled via entanglement swapping using the photons of two separate atom-photon entangled systems [63]. Their space-time diagram is shown in Fig. 2.5. The proposed setup exploits the facts that photons can be transmitted over a distance and that atoms can be detected with a detection efficiency of nearly 100%.

First, the atomic spin of a trapped atom is entangled with the polarization of a photon, emitted by the atom in a spontaneous decay [23]. This process happens independently in two different and separate setups, one setup for each atom respectively. The photons emitted in each trap are measured at a Bell state analyzer (BSA), indicated as Bell state measurement (BSM) in Fig. 2.5, in two of the four Bell states [64–66]. This projects the two atoms, being previously entangled with one of the two photons, in an entangled state [23]. The probability of detecting photons from both traps at

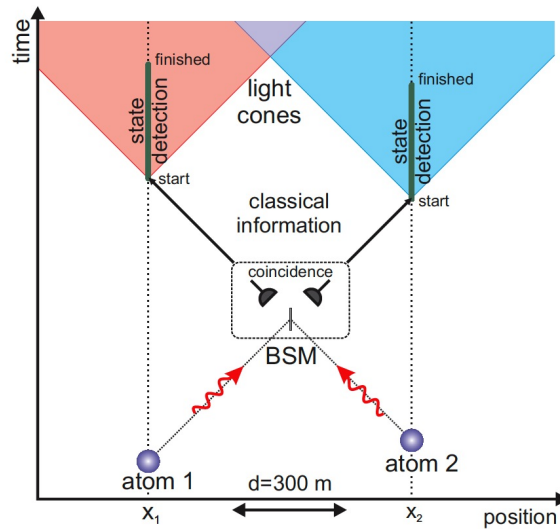


Fig. 2.5: Space-time diagram of the proposal of Rosenfeld et al. [63]. Two separate atoms are each entangled with a photon. A Bell state measurement (BSM) is performed on the two photons each from one of the atom traps. A successful BSM announces the entanglement of the two atoms. The atoms are detected with a detection efficiency of 100%. Figure reprinted from [63].

the BSA is low, but the detection efficiency and losses of the photons only decrease the heralding efficiency, and they do not open any loophole or require any additional assumption. Since the entanglement of the two atoms is heralded by the Bell state measurement of the photons, the scheme is an “event-ready” scheme [40, 58, 67]. The atoms themselves are then detected with a detection efficiency of 100%. Errors in the detection process reduce the visibility of the atom-atom entanglement, but as long as the achieved visibility exceeds the classical limit of $\frac{1}{\sqrt{2}} = 70.7\%$, the Bell inequality can still be violated. Closing the detection loophole is already demonstrated [23]. The two traps have yet to be space-like separated.

Freyberger et al. show how one can use pairs of two-level Rydberg atoms for closing the detection loophole [68] as a further development of the idealized proposal of Oliver and Stroud [69]. They suggest measures needed for the satisfaction of locality conditions as well. The two Rydberg atoms are produced independently: one in an excited state, the other in the ground state. To entangle them, they pass a high quality cavity. For a certain set of parameters of the interaction Hamiltonian, in half the cases the first Rydberg atom emits a photon during passage, which is then absorbed by the other Rydberg atom passing the cavity afterwards. The conditions defining the ensemble to be measured are analyzed in detail.

Fry et al proposed an experiment using two ^{199}Hg atoms, which are entangled during the dissociation of $^{199}\text{Hg}_2$ molecules via stimulated Raman excitation [70]. The entangled degrees of freedom are the components of angular momentum. The two mercury atoms are each spin- $\frac{1}{2}$ and, as the original molecule, spin 0 as a pair. This makes this system the subject of Bohm's Gedankenexperiment [30]: "Suppose that we have a molecule containing two atoms in a state in which the total spin is zero and that of each atom is $\hbar/2$. [...] Now suppose that the molecule is disintegrated by some process that does not change the total angular momentum." ² The spin components are measured using a spin state selective two-photon excitation-ionization.

2.5.2 Photon-atom entanglement

There are also proposals for experiments using photon-atom entanglement itself. The first demonstration of a violation of the CHSH inequality by entanglement between different species was demonstrated by Moehring et al. in the group of Monroe [71]. For asymmetric systems, as a photon and an atom, the detection efficiencies are very different. Atoms are detected with nearly 100% detection efficiency, while in addition to the non-ideal detector efficiency, coupling and transmission losses enter the overall detection efficiency of photons. It was shown that for a detection efficiency of atoms of 100% for an asymmetric system, the detection efficiency of photons can be as low as 70.7% for maximally entangled states in a CHSH inequality [61]. Using nonmaximally entangled states and a three-setting inequality I_{3322} this threshold is 43%. For nonmaximally entangled states and the CHSH inequality a detection efficiency of 50% is sufficient as well [61, 62].

2.5.3 Photon-ion entanglement

Simon and Irvine propose an experiment with entangled ions and photons [72]. The basic idea is similar to the proposal of Ref. [63] using atoms and photons. Two ions are each entangled with a photon. The two photons are measured on a Bell state analyzer in two of the four Bell states, what projects the ions into a Bell state. This allows a violation of a Bell inequality with near-unity detection efficiency of the entangled ions in an "event-ready" scheme.

2.5.4 Homodyne detection of entangled non-Gaussian states

Sangouard et al. in Weinfurter's group consider entanglement between two internal states of an atom with an optical mode, which contains less than a photon on aver-

² [30], edition from 1989, but unabridged and unaltered, p.614, 2nd break

age [73]. They show that a violation of the CHSH inequality with a value of the Bell parameter $S = 2.52$ is possible using homodyne detection and one-photon counting, while a value of $S = 2.26$ is possible using homodyne detection only.

García-Patrón et al. present a scheme for a loophole-free Bell experiment using continuous variables and highly efficient homodyne detection [74] based on previous proposals [75, 76]. A non-Gaussian state is conditionally prepared by subtracting single photons from a squeezed state (two mode squeezed state or two single-mode squeezed states combined on a beamsplitter) using a beamsplitter with high transmittance and a single-photon detector, e.g. an avalanche photodiode (APD). A low detection efficiency of the APDs decreases the success rate while influencing the state very little. For a violation of the Bell inequality the efficiency of the APDs is supposed to be $\geq 1\%$ and the detection efficiency of the homodyne detectors $\geq 90\%$. Both are experimentally feasible.

2.5.5 Qudits

Vértesi et al. show the use of higher dimensional systems has advantages for photon-atom entanglement experiments as well in experiments with hyperentangled photons [77]. For the asymmetric case of photon-atom entanglement the efficiency needed for photons can be reduced from the well known detection efficiency threshold of 43% for the photonics qubits [61] to $1/N$ for N -dimensional photonics qudits. For purely photonic systems, they propose a loophole-free Bell experiment using four-dimensional states with a detection threshold of 61.8% for no background and 69% with 1% noise. A four-setting Bell inequality [78] has to be measured detecting the photons with transition-edge sensors (TES) [25, 26].

2.5.6 Photons

An experiment with a purely photonics system is proposed by Kwiat et al. [56]. Based on Eberhard's paper introduced in detail in Sec. 3 [27], polarization-entangled photon pairs in nonmaximally entangled states produced by spontaneous parametric down-conversion are detected with efficient detectors. The overall detection efficiency in the limit of no background has to exceed $2/3$.

The basic idea of that proposal towards a conclusive Bell test is in principle followed in the presented work, but the nonmaximally entangled photon pairs are produced in a different source design and different, highly-efficient superconducting bolometric detectors are applied.

Theory of nonmaximally entangled states

Since Eberhard's publication, a proposal for a loophole-free Bell experiment based on his paper was written by Kwiat et al. [56]. Nonmaximally entangled states have been measured by Brida et al. testing the equivalent CH inequality under the fair sampling assumption [79]. Only coincidences were taken into account and not the measured singles. Hardy's test of nonlocality does not include an inequality, but since a zero result is experimentally impossible to measure, an inequality has to be tested. Experiments based on his paper have also been performed under the fair sampling assumption, demonstrating a violation [38, 80, 81]. For that purpose seven different nonmaximally entangled states were prepared in Ref. [81].

3.1 Hardy

Hardy proposes a test of local realism without using inequalities [36]. The correlations between two entangled particles are measured at four combinations of two different angles on each side. The joint probability distributions for three of the four combinations of angles yield zero coincidences. For local hidden variable theories, the fourth combination must then be zero as well, whereas quantum mechanics predicts a nonzero outcome. The test is similar to the "all or nothing" test of Greenberger, Horne and Zeilinger (GHZ) [37]. It is worth noting, that the test works for all entangled states except the maximally entangled one. Experimentally, it is not realizable in the form described by Hardy, because the derivation assumes perfect detectors, and what is more important, a zero result has to be measured. As a consequence, an inequality is measured, which for perfect detection efficiency is the CH inequality or Eberhard's inequality, as shown in [38, 39, 82, 83]. Hardy's test of nonlocality was successfully performed experimentally, but an additional assumption about the detection efficiency, the fair sampling assumption, was necessary [80, 81, 84–87].

3.2 Eberhard's paper

To get a lower threshold for the detection efficiency, Eberhard optimized a Bell inequality by changing the measurement settings as well as the state of the entangled particles [27]. The physical system he referred to is a pair of polarization-entangled photons measured with Nicol prisms with an ordinary and extraordinary output. He derived an inequality, which later was shown to be equivalent to the CH inequality [31], as demonstrated in Sec. 3.3. His formulation of the inequality includes coincidence counts as well as counts of photons that lost their partner due to the non-ideal detection efficiency. The states optimized for a maximal violation are pure nonmaximally entangled states. Eberhard's inequality is

$$\begin{aligned}
 J = & n_{oe}(\alpha_1, \beta_2) + n_{ou}(\alpha_1, \beta_2) \\
 & + n_{eo}(\alpha_2, \beta_1) + n_{uo}(\alpha_2, \beta_1) \\
 & + n_{oo}(\alpha_2, \beta_2) - n_{oo}(\alpha_1, \beta_1) \geq 0,
 \end{aligned} \tag{3.1}$$

where n are the coincidence counts with the subscripts o , e , u for the ordinary, extraordinary, and undetected measurement outcomes, the first subscript denoting Alice's measurement outcome and the second Bob's. Within his paper, the polarization is measured with Nicol prisms. Instead a block of calcite can be used as a polarizing beam displacer (BD) or the two o- and e-outputs are translated to s- and p-polarized output ports of a polarizing beam splitter cube (PBS). The undetected coincidence events n_{ou} and n_{uo} are the detected singles at output o of one of the parties with their partner photon not being detected by the second party, labeled u . The lower the overall detection efficiency the higher the number of these undetected events. Since their contribution increases the parameter J , it is impossible to violate the inequality for a detection efficiency lower than $2/3$. The angles of polarization α_1 , α_2 , β_1 , β_2 are measured with a half-wave plate (HWP) and a BD or a PBS³. Eberhard's states are pure states in the form

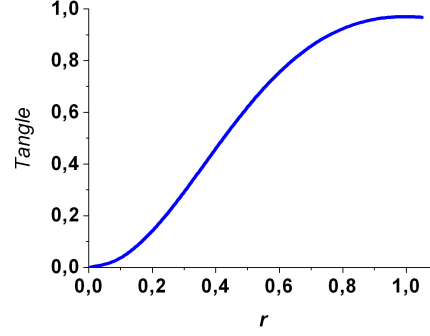
$$|\psi_r\rangle = \frac{1}{\sqrt{1+r^2}}(|HV\rangle + r|VH\rangle), \tag{3.2}$$

H representing a horizontally, V a vertically polarized photon with r being the parameter which can be optimized. For $r = 1$ the state describes a maximally entangled $|\psi_+\rangle$ state, otherwise the state is asymmetric and nonmaximally entangled. As the parameter r of the state $|\psi_r\rangle$ decreases, the entanglement of the state decreases according to Tab. 3.1 with the tangle \mathcal{T} as a measure of entanglement, explained in Sec. 4.3.1. For product states, the tangle is $\mathcal{T} = 0$ and for maximally entangled

³ alternatively, a sheet polarizer, which then has to be rotated by 90° to get the outcome e .

Tab. 3.1: Tangle \mathcal{T} for the ideal states $|\psi_r\rangle$ with different parameters r . The case of $r = 0$ corresponds to the separable state $|HV\rangle$.

η	r	\mathcal{T}
	0	0
66.7%	0.001	$4 \cdot 10^{-6}$
70%	0.136	0.0713
75%	0.311	0.3217
80%	0.465	0.5847
85%	0.608	0.7882
90%	0.741	0.9153
95%	0.871	0.9812
100%	1	1



$\mathcal{T} = 1$. For a given value of the efficiency η the angle Δ between α_1 and α_2 and also between β_1 and β_2 ⁴, the offset angle ω , and the background ζ were optimized to get a violation for the highest background possible. Since the measurement angles α_1 , α_2 , β_1 , and β_2 have the relations

$$\begin{aligned}
 \alpha_1 &= \frac{\omega}{2} - 90^\circ \\
 \alpha_2 &= \alpha_1 - \Delta \\
 \beta_1 &= \frac{\omega}{2} \\
 \beta_2 &= \beta_1 - \Delta
 \end{aligned} \tag{3.3}$$

with the optimized quantities, Eberhard's numerical results can be directly translated to the angles summed up in Tab. 3.2. For each detection efficiency, a specific state determined by the parameter r and a specific set of measurement angles α_1 , α_2 , β_1 , and β_2 violate the inequality with the maximally allowed background ζ . The lower the efficiency the smaller the allowed background and the smaller the violation. The background ζ is assumed to be white noise. The measurement angles are compared to Bell's for an overall detection efficiency of $\eta = 100\%$ in Fig. 3.1. For a violation of a Bell inequality with one of the four maximally entangled Bell states $|\psi_\pm\rangle = \frac{1}{\sqrt{2}}(|HV\rangle \pm |VH\rangle)$ and $|\phi_\pm\rangle = \frac{1}{\sqrt{2}}(|HH\rangle \pm |VV\rangle)$ the measurement angle are often chosen such that α_1 and β_1 enclose 22.5° , and α_1 and α_2 as well as β_1 and β_2 enclose 45° . The measurement angles α_1 and β_1 calculated by Eberhard enclose 90° , and α_1 and α_2 as well as β_1 and β_2 enclose 45° . This may be surprising at first because in the case of a singlet state, which is often used in Bell experiments for rotation invariance,

⁴ $\Delta = \alpha_1 - \alpha_2 = \beta_1 - \beta_2$

Tab. 3.2: Numerical results of Eberhard [27], with the angles α_1, α_2 for a measurement at Alice and β_1, β_2 for Bob. For a violation, the maximally allowed background is ζ .

η	ζ	r	α_1	α_2	β_1	β_2
66.7%	0.0%	0.001	-90.0°	92.2°	0.0°	-2.2°
70%	0.02%	0.136	-88.3°	-109.7°	1.7°	-19.7°
75%	0.31%	0.311	-85.2°	-117.2°	4.9°	-27.2°
80%	1.10%	0.465	-82.55°	-120.45°	7.45°	-30.45°
85%	2.48%	0.608	-80.7°	-122.2°	9.3°	-32.2°
90%	4.50%	0.741	-79.6°	-123.2°	10.5°	-33.2°
95%	7.12%	0.871	-78.95°	-123.65°	11.05°	-33.65°
100%	10.36%	1.000	-78.75°	-123.75°	11.25°	-33.75°

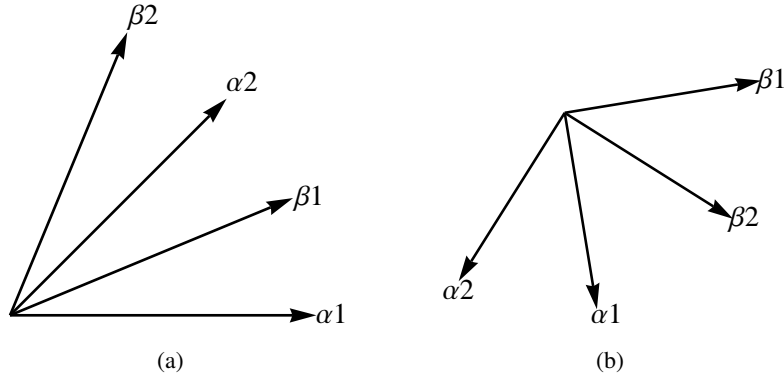


Fig. 3.1: The measurement angles for $\eta = 100\%$ as used for the violation of Bell's inequality (a), and Eberhard's (b).

this would end all correlations. But the state $|\psi_{r=1}\rangle$ corresponds to a triplet state, dissolving this concern. Using both sets of angles, a maximal violation of Eberhard's inequality $J = -0.2071$ is obtained as well as a maximal violation of the CH and CHSH inequality.

3.3 Comparison to the CH inequality

The Eberhard inequality (3.1) in the form of the original paper

$$\begin{aligned}
 J = & n_{oe}(\alpha_1, \beta_2) + n_{ou}(\alpha_1, \beta_2) \\
 & + n_{eo}(\alpha_2, \beta_1) + n_{uo}(\alpha_2, \beta_1) \\
 & + n_{oo}(\alpha_2, \beta_2) - n_{oo}(\alpha_1, \beta_1) \geq 0,
 \end{aligned}$$

includes coincidence count rates at combinations of any of the two outputs of a polarizing beam-splitter on each side (n_{oe} , n_{eo} , n_{oo}) as well as count rates on the ordinary output at Alice (Bob) when none are detected at any output at Bob (Alice) (n_{ou} and n_{uo} respectively). The single count rate at Alice’s detector at the ordinary output of the polarizing beam-splitter is the same as the count rate with the (lossless) polarizer removed. It is

$$S_{o-}(\alpha_1, -) = n_{oo}(\alpha_1, -) + n_{oe}(\alpha_1, -) + n_{ou}(\alpha_1, -) \quad (3.4)$$

for any angle β at Bob’s side, and analogously at Bob’s, it is

$$S_{-o}(-, \beta_1) = n_{oo}(-, \beta_1) + n_{eo}(-, \beta_1) + n_{uo}(-, \beta_1), \quad (3.5)$$

independent of the angle α on Alice’s side. Substituting the $n_{ou}(\alpha_1, \beta_2)$ and $n_{uo}(\alpha_2, \beta_1)$ events in the Eberhard inequality (3.1) results in

$$\begin{aligned} J = & S_{o-}(\alpha_1, \beta_2) - n_{oo}(\alpha_1, \beta_2) \\ & + S_{-o}(\alpha_2, \beta_1) - n_{oo}(\alpha_2, \beta_1) \\ & + n_{oo}(\alpha_2, \beta_2) - n_{oo}(\alpha_1, \beta_1) \geq 0. \end{aligned} \quad (3.6)$$

An important consequence of this form of the inequality is that no polarizing beam-splitter with two outputs is needed, but that instead it is sufficient to detect only the ordinary output of Alice and Bob or use a linear polarizer. This reduces the number of efficient detectors needed for an experimental violation from four to two. The other interesting issue is a comparison with the CH inequality (2.4). Taking the upper bound of the inequality and the number of measured counts, for $a = \alpha_2$, $a' = \alpha_1$, $b = \beta_1$ and $b' = \beta_2$, the two inequalities (3.1) and (2.4) differ only by a multiplication by -1 . This shows the equivalence of the Eberhard inequality with the CH inequality [31], as also shown by [35, 38, 39].

3.4 “Diagonal” basis for pure nonmaximally entangled states

Photon pairs produced by spontaneous parametric downconversion of type II are polarized horizontally and vertically (explained in Secs. 4.1 and 4.2). Hence, the strong correlations between the partners of an entangled photon pair produced in a Sagnac source can be understood classically as well. In the conjugate diagonal basis DA the correlation can only be explained by entanglement. Transforming the Bell states from the HV to the DA basis reveals the entanglement. In the Sagnac source the visibility of the state measured in the HV basis is limited only by the setup itself (PBS,

accidentals, dark or background counts, polarization compensation in fiber). In the DA basis the visibility is additionally determined by the indistinguishability of the two photon emissions in both pump directions of the Sagnac loop. The visibility of the entangled state has to be measured in this diagonal basis. For the Eberhard states $|\psi_r\rangle$ (Eq. (3.2)) the case is less simple. The state itself is nonmaximally entangled but still pure. The HV and VH population is asymmetric. Instead of the diagonal and antidiagonal basis vectors, the “diagonal” basis comprises the diagonal or antidiagonal vector and a vector that depends on the state $|\psi_r\rangle$ itself. To transform the Eberhard state $|\psi_r\rangle$ from the HV to a new basis,

$$\begin{aligned} |\alpha\rangle &= \cos\alpha|H\rangle + \sin\alpha|V\rangle \\ |-\alpha\rangle &= \cos\alpha|H\rangle - \sin\alpha|V\rangle \\ |H\rangle &= \frac{1}{2\cos\alpha}(|\alpha\rangle + |-\alpha\rangle) \\ |V\rangle &= \frac{1}{2\sin\alpha}(|\alpha\rangle - |-\alpha\rangle) \end{aligned} \quad (3.7)$$

are used with a different angle for each subspace: for the first particle $|\alpha\rangle$ and $|-\alpha\rangle$, and for the second $|\beta\rangle$ and $|-\beta\rangle$. By substituting $|H\rangle$ and $|V\rangle$ in Eq. (3.2), the nonmaximally entangled state $|\psi_r\rangle$ is

$$\begin{aligned} |\psi_r\rangle &= \frac{1}{\sqrt{1+r^2}} \left(|HV\rangle + r|VH\rangle \right) \\ &= \frac{1}{\sqrt{1+r^2}} \left(\frac{1}{2\cos\alpha}(|\alpha\rangle + |-\alpha\rangle) \otimes \frac{1}{2\sin\beta}(|\beta\rangle - |-\beta\rangle) \right. \\ &\quad \left. + r \frac{1}{2\sin\alpha}(|\alpha\rangle - |-\alpha\rangle) \otimes \frac{1}{2\cos\beta}(|\beta\rangle + |-\beta\rangle) \right) \\ &= \frac{1}{4\sqrt{1+r^2}} \left(\left(\frac{1}{\cos\alpha\sin\beta} + r \frac{1}{\sin\alpha\cos\beta} \right) (|\alpha\beta\rangle - |-\alpha-\beta\rangle) \right. \\ &\quad \left. + \left(\frac{1}{\cos\alpha\sin\beta} - r \frac{1}{\sin\alpha\cos\beta} \right) (|-\alpha\beta\rangle - |\alpha-\beta\rangle) \right). \end{aligned} \quad (3.8)$$

To get a pure state the condition

$$r = \pm \frac{\tan\alpha}{\tan\beta} \sqrt{\frac{4\cos^2\alpha\sin^2\beta - 1}{1 - 4\sin^2\alpha\cos^2\beta}} \quad (3.9)$$

has to be fulfilled. For the specific choice of $\alpha = 45^\circ$ the angle β becomes $\beta = \arctan\frac{1}{r}$. This leads to the state

$$|\psi_r\rangle = \frac{1}{\sqrt{2}} \left(|45 \arctan(\frac{1}{r})\rangle - | -45 - \arctan(\frac{1}{r})\rangle \right). \quad (3.10)$$

For the choice of $\beta = 45^\circ$ the angle α becomes $\alpha = \arctan r$, which leads to the state

$$|\psi_r\rangle = \frac{1}{\sqrt{2}} \left(|\arctan(r) \ 45\rangle - |-\arctan(r) \ -45\rangle \right). \quad (3.11)$$

As a consequence maximal coincidences can be found at the combination of angles $\alpha = \pm 45^\circ$ and $\beta = \pm \arctan \frac{1}{r}$ or $\alpha = \pm \arctan r$ and $\beta = \pm 45^\circ$. Minimal coincidences can be found at orthogonal states $|\alpha'\beta'\rangle$ for which either $\langle\alpha'|\alpha\rangle = 0$ or $\langle\beta'|\beta\rangle = 0$ because $\langle\alpha'\beta'|\alpha\beta\rangle = \langle\alpha'|\alpha\rangle\langle\beta'|\beta\rangle = 0$. The corresponding angle combinations for minimal coincidence count rates are $\alpha = \mp 45^\circ$ and $\beta = \pm \arctan \frac{1}{r}$ or $\alpha = \pm 45^\circ$ and $\beta = \pm \arctan \frac{1}{r} - \frac{\pi}{2} = \mp \arctan r$ for Eq. (3.10) and $\alpha = \pm \arctan r - \frac{\pi}{2} = \mp \arctan \frac{1}{r}$ and $\beta = \pm 45^\circ$ or $\alpha = \pm \arctan r$ and $\beta = \mp 45^\circ$ for Eq. (3.11).

Alternatively, the angles can be determined by calculating the minimal and maximal measurement results. The first qubit is measured under the angle α and the second qubit under the angle β . Since an arbitrary polarization state of a photon can be described by $|\alpha\rangle = \cos\alpha|H\rangle + \sin\alpha|V\rangle$, a system of two photons is described as a tensor product of the respective states of each photon $|\alpha\rangle \otimes |\beta\rangle = (\cos\alpha|H\rangle + \sin\alpha|V\rangle) \otimes (\cos\beta|H\rangle + \sin\beta|V\rangle)$. As an abbreviation $|\alpha\beta\rangle$ is used and can be written as an vector in the HV basis as

$$|\alpha\beta\rangle = \begin{pmatrix} \cos\alpha\cos\beta \\ \cos\alpha\sin\beta \\ \sin\alpha\cos\beta \\ \sin\alpha\sin\beta \end{pmatrix}. \quad (3.12)$$

The above mentioned measurement is represented by an operator $\hat{A}(\alpha, \beta) = |\alpha\beta\rangle\langle\alpha\beta|$, an outer product of the two photon state vector $|\alpha\beta\rangle$ with its conjugate transpose $\langle\alpha\beta|$. The operator $\hat{A}(\alpha, \beta)$ can be represented as a 4×4 matrix. A measurement result is in general defined as the trace $\text{tr}(\hat{A}(\alpha, \beta)\rho)$ of the product of the measurement operator $\hat{A}(\alpha, \beta)$ and the density matrix ρ . For a pure state it is the same as $|\langle\alpha\beta|\psi_r\rangle|^2$. The result of the polarization measurement on photon 1 under the angle α and on photon 2 under the angle β is

$$\text{tr}(\hat{A}(\alpha, \beta)\rho) = \frac{1}{1+r^2} (\cos\alpha\sin\beta + r\sin\alpha\cos\beta)^2. \quad (3.13)$$

Minimal coincidence rates can be found at α arbitrary and $\beta = -\arctan(r\tan\alpha)$ or $\alpha = -\arctan(\frac{\tan\beta}{r})$ with an arbitrary β . For a fixed α the measurement angles β for maximal and minimal count rates are orthogonal to each other. It is analogous for fixed β .

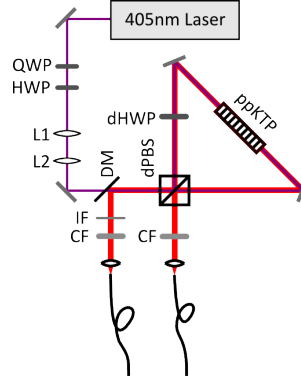


Fig. 3.2: Sagnac-source. The pump beam is focused in the periodically poled KTP (ppKTP) crystal within the Sagnac loop built by the dual-wavelength polarizing beam splitter (dPBS) and the two mirrors. The crystal can be pumped bidirectionally. The photon pairs created by SPDC are split at the dPBS in two modes, which are coupled into fibers.

3.5 Nonmaximally entangled states produced by a Sagnac source

In the presented work, a Sagnac source is used as the source of polarization-entangled photon pairs [28, 88]. A periodically poled KTP (ppKTP) crystal is used as the non-linear crystal within the bidirectionally pumped Sagnac loop. The pump laser has a wavelength of 405nm, and the crystal is kept at a temperature for degenerate spontaneous parametric downconversion (SPDC) at a wavelength of 810nm. (For more information about periodic poling, SPDC and Sagnac source see Chap. 4.) Due to the way the Sagnac source is constructed (see Fig. 3.2) the visibility measured in the HV -basis $\{|HH\rangle, |HV\rangle, |VH\rangle, |VV\rangle\}$ is perfect (when corrected for contributions of accidental coincidences), but less than perfect for any other basis. Instead of the ideal density matrix $\rho_r = |\psi_r\rangle\langle\psi_r|$ the best representation of the produced state of the photon pairs in the HV -basis is the state

$$\rho'_r = \frac{1}{1+r^2} \begin{pmatrix} 0 & 0 & 0 & 0 \\ 0 & 1 & Vr & 0 \\ 0 & Vr & r^2 & 0 \\ 0 & 0 & 0 & 0 \end{pmatrix}, \quad (3.14)$$

where the visibility enters in the off-diagonal elements (coherence terms). For the two photon polarization state produced by the Sagnac source ρ'_r measured at polarization

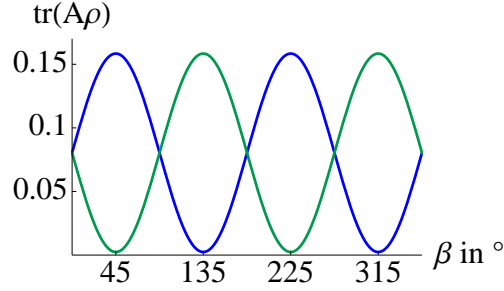


Fig. 3.3: Blue curve: $\alpha = \arctan(\frac{1}{r})$, green curve: $\alpha = -\arctan(\frac{1}{r})$, for both β is varied from 0 to 360° for $r = 0.311$ and $V = 97\%$.

angle α for the first photon and β for the second photon, the result is

$$\begin{aligned} \text{tr}(\hat{A}(\alpha, \beta)\rho'_r) = & \quad (3.15) \\ \frac{1}{1+r^2}(\cos^2 \alpha \sin^2 \beta + 2rV \sin \alpha \sin \beta \cos \alpha \cos \beta + r^2 \sin^2 \alpha \cos^2 \beta). \end{aligned}$$

In order to characterize the visibility of the produced state ρ'_r in the experiment, measurements at special angles have to be performed. For a Bell state prepared by the Sagnac source, $(\rho'_{r=1})$, the measurement is performed at combinations of the diagonal and antidiagonal polarization angles D and A . For a nonmaximally entangled state the visibility is determined by measurements in a corresponding set of angles: the non-orthogonal set of angles $\{|\alpha\beta\rangle, |\alpha-\beta\rangle, |-\alpha\beta\rangle, |-\alpha-\beta\rangle\}$. The visibility is calculated from the maximal (Max) and minimal (Min) number of coincidences as

$$V = \frac{\text{Max} - \text{Min}}{\text{Max} + \text{Min}} = \frac{\text{tr}(\hat{A}(\alpha, \beta)\rho'_r) - \text{tr}(\hat{A}(\alpha, -\beta)\rho'_r)}{\text{tr}(\hat{A}(\alpha, \beta)\rho'_r) + \text{tr}(\hat{A}(\alpha, -\beta)\rho'_r)}. \quad (3.16)$$

Using Eq. (3.15) gives

$$V = \frac{4rV \sin \alpha \cos \alpha \sin \beta \cos \beta}{2r^2 \sin^2 \alpha \cos^2 \beta + 2 \cos^2 \alpha \sin^2 \beta}. \quad (3.17)$$

This results in the condition $r = \frac{\tan \beta}{\tan \alpha}$ which is fulfilled by any set of angles α with $\beta = \arctan(r \tan \alpha)$ or $\alpha = \arctan(\frac{\tan \beta}{r})$ for any β . The minimal coincidence rates can be found at an arbitrary angle $\pm \alpha$ with $\beta = \mp \arctan(r \tan \alpha)$ and $\alpha = \pm \arctan(\frac{\tan \beta}{r})$ with an arbitrary angle $\mp \beta$. The angle $\alpha = \pm \arctan(\frac{1}{r})$ is plotted versus the angle β in Fig. 3.3. Since the set of angles is different for every state specified by a certain r , the angles can be used to prepare the state in the experiment.

3.6 State optimization

The optimal state of the form $|\psi_r\rangle$ as well as the measurement angles for the largest violation of the Eberhard inequality are calculated numerically based on a model,

that accounts for experimental results for dark and background counts, visibility and coincidence window in the way described below.

The dark and background counts d enter the model as additional single counts. They are treated in the same way as $S_{o-}(\alpha_1, \beta_2)$ and $S_{-o}(\alpha_2, \beta_1)$ in Eq. (3.6). This results in an altered Eberhard inequality

$$\begin{aligned} J = & S_{o-}(\alpha_1, \beta_2) + d - n_{oo}(\alpha_1, \beta_2) \\ & + S_{-o}(\alpha_2, \beta_1) + d - n_{oo}(\alpha_2, \beta_1) \\ & + n_{oo}(\alpha_2, \beta_2) - n_{oo}(\alpha_1, \beta_1) \geq 0. \end{aligned} \quad (3.18)$$

The dark and background counts can be determined experimentally by measuring the detected count rates when the source of entangled photon pairs is turned off. Detectors as APDs have intrinsic dark counts, whereas in the case of transition-edge sensors peaks from the noise band or blackbody photons constitute the equivalent. For all types of detectors stray light photons and residual lab lights contribute as well, but can be reduced or eliminated by careful preparation of the lab. The measured dark and background count rate d enters the model as one of the inputs.

Accidental coincidences Acc are produced when two photons, which are not partners of the same entangled pair, are registered within the coincidence window τ . Their contribution is higher for higher count rates and for longer coincidence windows, but lower for a higher ratio between coincidences and singles of Alice or Bob respectively. In the limiting case of detecting all photons in pairs at angles showing maximal correlation ($\frac{n_{oo}}{S_{-o}} = 1$ or $\frac{n_{oo}}{S_{o-}} = 1$), no accidental counts are possible. This dependency is expressed by

$$\begin{aligned} Acc_{oo}(\alpha, \beta) = & \\ = & S_{o-}(\alpha, \beta) \cdot S_{-o}(\alpha, \beta) \cdot \tau \cdot \left(1 - \frac{n_{oo}(\alpha, \beta)}{S_{-o}(\alpha, \beta)}\right) \left(1 - \frac{n_{oo}(\alpha, \beta)}{S_{o-}(\alpha, \beta)}\right). \end{aligned} \quad (3.19)$$

Since the single count rates are angle dependent and the strength of the correlations is different for different angle combinations, the accidental coincidences depend on the angles at which they occur. They are contributing in the same way as the coincidence counts $n_{oo}(\alpha, \beta)$ in the Eberhard inequality, changing it to

$$\begin{aligned} J = & S_{o-}(\alpha_1, \beta_2) + d - n_{oo}(\alpha_1, \beta_2) - Acc_{oo}(\alpha_1, \beta_2) \\ & + S_{-o}(\alpha_2, \beta_1) + d - n_{oo}(\alpha_2, \beta_1) - Acc_{oo}(\alpha_2, \beta_1) \\ & + n_{oo}(\alpha_2, \beta_2) + Acc_{oo}(\alpha_2, \beta_2) - n_{oo}(\alpha_1, \beta_1) - Acc_{oo}(\alpha_1, \beta_1) \geq 0. \end{aligned} \quad (3.20)$$

The accidental count rates depend on the coincidence window τ and the single count rates S_{o-} and S_{-o} . The coincidence window τ has to be predetermined in a measure-

ment of coincident pairs as one of the inputs of the optimization. The single count rates S_{o-} and S_{-o} themselves, as well as the coincidence rate $n_{oo}(\alpha, \beta)$, depend on the overall detection efficiency η and the pair production rate R . These two latter entities are again inputs of the optimization.

For a state described by Eq. (3.14), the visibility V is the last input. As described in Sec. 3.5, the visibility can be measured under specified angles.

To start the optimization the dark and blackbody count rate d , the coincidence window τ , the overall detection efficiency η , the pair production rate R , and the visibility V need to be predetermined experimentally. The resulting state and measurement angles are then optimal for a violation under these specific experimental conditions. In case that these conditions are not sufficient, e.g. $\eta < 2/3$, no optimal settings for a violation are found in the optimization.

The optimization tries to minimize numerically the left hand side of the modified Eberhard inequality Eq. (3.20) varying the measurement angles $\alpha_1, \alpha_2, \beta_1, \beta_2$ and the state defining parameter r .

Tools and techniques

A setup of a Bell experiment based on polarization-entangled photon pairs consists of a source, polarization analyzers and detectors. The source used in the presented work is the Sagnac source where the nonlinear process of spontaneous parametric downconversion is used to generate photon pairs. For the detection of the single photons conventional avalanche photodiodes (APDs) and a novel type of superconducting detectors, the transition-edge sensors, are used. For the understanding of the experimental setup and its characterization, some physical processes, quantities and techniques are introduced in this chapter.

4.1 Spontaneous parametric downconversion

Spontaneous parametric downconversion (SPDC) is a nonlinear process which is nowadays in wide use for the generation of entangled pairs of photons. In a setup such as the Sagnac source, this process is used to produce polarization-entangled photon pairs [28, 88].

4.1.1 Nonlinear optics

In many materials the interaction between light and matter is sufficiently described by a linear dependence of polarization P on the electric field E . In nonlinear materials the polarization can also depend on higher powers of the electric field [89]; the relation can be written as a power series

$$P = \varepsilon_0 \chi_1 E_0 + \varepsilon_0 \chi_2 E_0^2 + \varepsilon_0 \chi_3 E_0^3 + \dots, \quad (4.1)$$

with the i -th order susceptibility χ_i of the medium and the vacuum permittivity ε_0 . The nonlinear effects become important when a high electric field, in the order of the

characteristic atomic field, is applied. This only became available since the invention of the laser 1960 [90].

Light incident on a nonlinear medium consisting of two frequency components ω_1 and ω_2 , represented as $E = E_1 e^{i\omega_1 t} + E_2 e^{i\omega_2 t} + c.c.$, results in

$$\begin{aligned}
P = & \varepsilon_0 \chi_1 (E_1 e^{i\omega_1 t} + E_2 e^{i\omega_2 t} + c.c.) + \\
& \varepsilon_0 \chi_2 \left(2(|E_1|^2 + |E_2|^2) \right. \\
& \quad + (E_1^2 e^{i2\omega_1 t} + E_2^2 e^{i2\omega_2 t} \\
& \quad \left. + 2E_1 E_2 e^{i(\omega_1 + \omega_2)t} + 2E_1 E_2^* e^{i(\omega_1 - \omega_2)t} + c.c.) \right) + \dots
\end{aligned} \tag{4.2}$$

The polarization P not only contains the input frequencies ω_1 and ω_2 , but also the terms of second harmonic generation (SHG) ($2\omega_i$), the terms of sum frequency generation (SFG) ($\omega_1 + \omega_2$), the terms of difference frequency generation (DFG) ($\omega_1 - \omega_2$) and the optical rectification term ($|E_1|^2 + |E_2|^2$), a static electric field.

Spontaneous parametric downconversion (SPDC) is the reversed process to SFG. The output of a beam of photons of single frequency ω_p incident on an appropriate material mainly consists of the input frequency ω_p , but also of photon pairs with the frequencies ω_s and ω_i under conservation of energy $E = \hbar\omega$ and momentum $\vec{p} = \hbar\vec{k}$ with $|\vec{k}| = \frac{n(\omega)\omega}{c}$. The refractive index n in general depends on the frequency ω . This leads to the following conditions

$$\omega_s + \omega_i = \omega_p \tag{4.3}$$

$$n(\omega_s)\omega_s + n(\omega_i)\omega_i = n(\omega_p)\omega_p, \tag{4.4}$$

which are called phasematching conditions. Only when they are fulfilled in birefringent materials or materials with quasi-phasematching (QPM) can the two new frequency components ω_s and ω_i emerge from the nonlinear material.

There is type I and type II phasematching. In the case of type I, an extraordinary polarized pump photon is converted to two photons with ordinary polarization. In a type II crystal, the pump photon is converted to an ordinary and an extraordinary polarized photon.

4.1.2 Quasi-phasematching

The phasematching condition (4.4) can be rewritten as

$$n(\omega_s)\omega_s + n(\omega_i)\omega_i - n(\omega_p)\omega_p = \Delta k, \tag{4.5}$$

with $\Delta k = 0$. Phasematching conditions with $\Delta k \neq 0$ can be achieved by periodical poling of a nonlinear material, as predicted in the early 1960's [91, 92]. One of

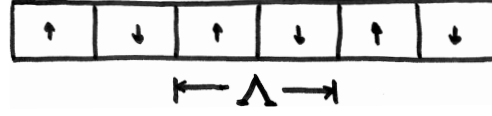


Fig. 4.1: Periodic poling of a nonlinear crystal with the grating period Λ .

the crystalline axes along the material is periodically inverted along the nonlinear material with a grating period Λ , as shown in Fig. 4.1, leading to $\Delta k = \frac{2\pi}{\Lambda}$. This allows to phasematch nonlinear processes independent of their birefringence. The dependency of the refractive index n and the poling period Λ on temperature allows the phasematching to be tuned by temperature.

The refractive index n of a material depends not only on the frequency ω (or wavelength $\lambda = \frac{2\pi c}{\omega}$), but also on the temperature T of the material. An empirical equation for this dependency is the Sellmeier equation with coefficients that must be determined experimentally, as must the coefficients for the temperature dependence. Various equations and empirical coefficients can be found in literature for different materials. The nonlinear crystal used in this work is a periodically poled potassium titanyl phosphate (ppKTP). For KTP, the Sellmeier equation of the form

$$n(\lambda)^2 = a + \frac{b}{\lambda^2 - c} + \frac{d}{\lambda^2 - e} \quad (4.6)$$

together with the respective coefficients a, b, c, d, e of Kato and Takaoka [93] and the description of change of refractive index n with temperature T of the form

$$n(\lambda, T) = \sum_{m=0}^3 \frac{a_m}{\lambda^m} (T - 25^\circ\text{C}) + \sum_{m=0}^3 \frac{b_m}{\lambda^m} (T - 25^\circ\text{C})^2 \quad (4.7)$$

with corresponding coefficients a_i, b_j of Emanuelli and Arie [94] can be used for calculations. The latter also give coefficients and an equation of the form

$$L(T) = L_0(1 + \alpha(T - 25^\circ\text{C}) + \beta(T - 25^\circ\text{C})^2) \quad (4.8)$$

for the thermal expansion of KTP, which can be applied to the poling period Λ .

More details on nonlinear optics and QPM can be found in [89, 95, 96] and more about QPM in ppKTP in [97].

4.2 Sagnac source

The Sagnac source shown in Fig. 4.2 is a source of polarization-entangled photon pairs [28, 88]. It consists of a potassium titanyl phosphate (KTP) crystal periodically



Fig. 4.2: Photograph of the Sagnac source used for the presented experiments.

poled for type II SPDC. It is pumped bidirectionally within a loop built by a polarizing beam splitter (PBS) and two mirrors. At the PBS, the photons of the pump beam are directed in one of the two possible pump directions depending on their polarization (see Fig. 4.3). Horizontally polarized pump photons are transmitted by the PBS. Since the process of spontaneous parametric downconversion (SPDC) is a non-linear effect, the probability of a pump photon being converted into a pair of photons with less energy is very low. The pump beam passes through the crystal, and the polarization of the beam is rotated by the dual-wavelength half-wave plate (dHWP) by 90° from horizontal to vertical polarization. Then the pump beam is reflected at the PBS, back in the direction of the laser. In the crystal a small number of pump photons are converted to pairs of photons, one partner with the same polarization as the pump beam, and the other partner orthogonal to it. The two photons are called signal and idler. At the dHWP the polarization of both downconverted photons is rotated by 90° . As the dHWP the PBS is also designed for the wavelengths of the pump beam and of the downconverted photons — a dual-wavelength PBS (dPBS). The vertically polarized downconversion photons are reflected at the dPBS and take the same output as the pump beam after the Sagnac loop. A dichroic mirror (DM) separates the two wavelengths and the downconversion photons leave output 3. Horizontally polarized photons are transmitted into output 4, as shown in Fig. 4.3. Vertically polarized pump photons are reflected at the dPBS and pass the dHWP becoming horizontally polarized. This is necessary because the ppKTP crystal only converts photons of a certain polarization; in this setup only horizontally polarized ones. As they pass through the

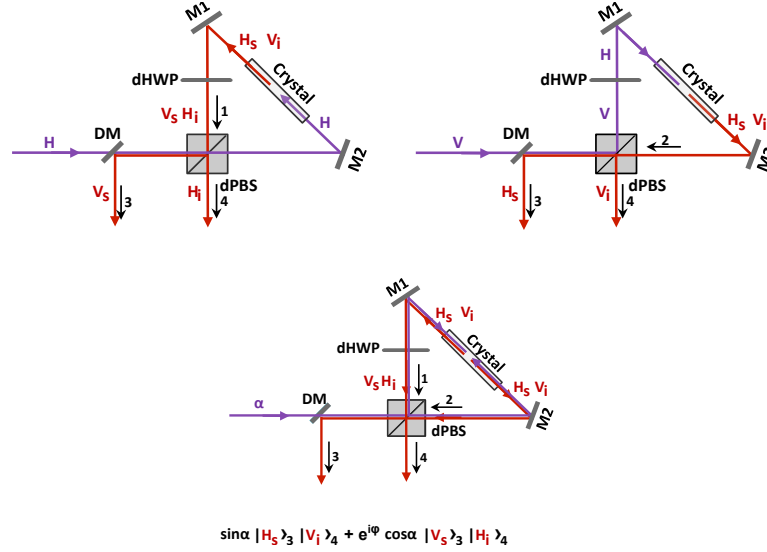


Fig. 4.3: Generation of polarization-entangled photon pairs in a Sagnac loop. Figure adapted from [98].

crystal, some pump photons are downconverted into pairs as described above, with one horizontally and one vertically polarized photon. The horizontal one is transmitted by the PBS so it goes in the same direction as the pump beam after the loop. Both wavelengths are separated by the DM with the downconversion photon leaving at output 3. The vertically polarized photon is reflected on the PBS into output 4. Depending on the polarization of the pump beam, photon pairs are produced in the corresponding pump direction. To get a maximally entangled state, the two pump directions have to be indistinguishable in all degrees of freedom. The probability to detect a downconverted photon from any of the two pump directions has to be equal, which in the ideal case is true for a pump polarization of 45° . Pumping the Sagnac loop in only one direction produces a separable state. When one direction of the Sagnac loop is pumped more than the other, the produced state is nonmaximally entangled, but in principle still pure.

4.3 Experimental characterization

The states of interest for a violation of a Bell inequality without additional assumptions using photons are nonmaximally entangled states. The entanglement of the states can be measured and the states can be fully characterized by the density matrix of the state.

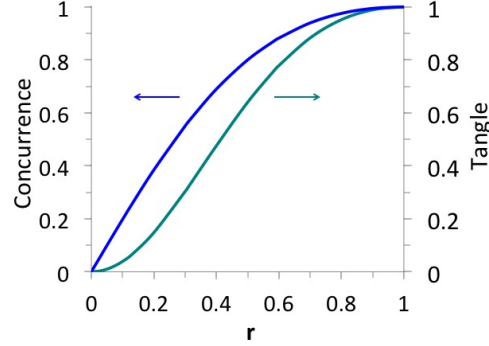


Fig. 4.4: The concurrence \mathcal{C} and the tangle \mathcal{T} of an ideal Eberhard state $|\psi_r\rangle$ are shown for varying r .

4.3.1 Measure of entanglement

To quantify entanglement, different measures of entanglement such as negativity, entanglement of formation (EOF), relative entropy of entanglement were developed (overview given in [99, 100]).

Tangle \mathcal{T} is a measure of entanglement, defined as the concurrence \mathcal{C} squared. For an arbitrary two-qubit state this is

$$\mathcal{T} = \mathcal{C}^2 = \max\{0, \lambda_1 - \lambda_2 - \lambda_3 - \lambda_4\}^2 \quad (4.9)$$

where λ_i^2 are the eigenvalues of the matrix product of the density matrix ρ with its spin-flipped complex conjugated self, $\tilde{\rho} = (\sigma_y \otimes \sigma_y) \rho^* (\sigma_y \otimes \sigma_y)$ [101, 102]. The eigenvalues are sorted in decreasing order such that $\lambda_1 \geq \lambda_2 \geq \lambda_3 \geq \lambda_4$. The spin-flipping operation is performed using the Pauli matrix $\sigma_y = \begin{pmatrix} 0 & -i \\ i & 0 \end{pmatrix}$, with all matrices represented in the basis $\{|HH\rangle, |HV\rangle, |VH\rangle, |VV\rangle\}$. The concurrence \mathcal{C} is also related with the EOF via a binary entropy function, which makes tangle, concurrence and EOF closely related [103]. The tangle \mathcal{T} is zero for separable states and one for maximally entangled states. As an example the concurrence \mathcal{C} and tangle \mathcal{T} of an Eberhard state (see Sec. 3) are shown in Fig. 4.4.

4.3.2 Density matrix reconstruction

In optics an arbitrary state of polarization of a beam can be fully described by the four Stokes-parameters [104]. Therefore, the beam is analyzed in the three mutually

unbiased bases: horizontal/vertical $\{H, V\}$, diagonal/antidiagonal $\{D, A\}$, right-/left-circular $\{R, L\}$. The measured data is processed to four Stokes parameters. Similarly, it is possible to perform a set of 4^n measurement, depending on the number n of photons involved, and process them to reconstruct the density matrix, a description of the state of the multiphoton system. For pairs of photons, the minimal number of measurements needed for a reconstruction is 16. The density matrix is reconstructed using the maximum likelihood method [105]. From this density matrix other quantities such as fidelity and tangle can be calculated; the uncertainties for these quantities can be calculated with a Monte-Carlo routine assuming Poissonian errors.

4.4 Detection system based on transition-edge sensors

For a long time, a problem for a loophole-free Bell experiment using entangled photons was the low detection efficiency of single-photon detectors such as APDs, visible light photon counters (VLPCs) and solid state photomultipliers (SSPMs) with a detection efficiency of 20% to 88% [106, 107]. Including transmission and coupling losses, the threshold of 82.4% for maximally entangled states and even the threshold for nonmaximally entangled states of $2/3$ (in the limit of no noise) is not feasible. A new class of detectors based on superconductivity have developed: superconducting nanowire single-photon detectors (SNSPDs) [108] and transition-edge sensors (TES) [109].

Nanowire detectors are made of thin superconducting wires, which are 30 to a few hundred nanometers wide and are meandered as shown in Fig. 4.5, for example. They are commonly produced from niobium nitride (NbN) and have a reported timing jitter of less than 30ps with a detection efficiency of 25% at 1550nm [112] and a reported timing jitter of less than 50ps with an efficiency of 67% at 1064nm and 57% at 1550nm [113]. Recently, a system detection efficiency of 93% at 1550nm was achieved using tungsten silicide (WSi) with a timing jitter of 150ps operable at 2K [114]. For an on-chip device, where photons are coupled evanescently from the waveguide to the NbN nanowire fabricated on top, an on-chip detection efficiency at 1550nm of 91% with 19ps timing jitter has been reported [115].

TESs are bolometers which operate on the transition from superconductivity to normal conductance. Since the transition edge is very steep, even an energy deposition as small as the energy of a single photon (0.8eV for 1550nm) can be detected with an appropriate readout. TESs are highly efficient and photon-number resolving, but have a relatively high timing jitter of 3ns to 25ns (details in Sec. 4.4.2).

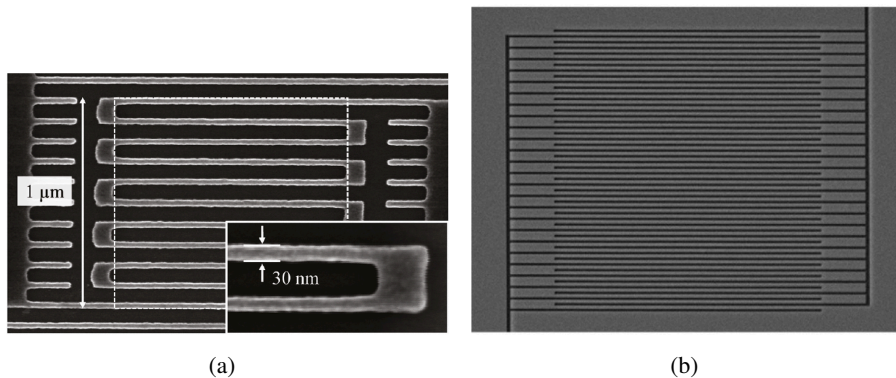


Fig. 4.5: Scanning electron micrographs. (a) SNSPD based on a nanowire 30nm wide, ~ 5 nm thick and a pitch of 100nm [110], (b) SNSPD based on nanowire 150nm wide and a pitch of 250nm, and an active area of the device of $\sim 15 \mu\text{m} \times 15 \mu\text{m}$ [111]. Figures reprinted from [110] and [111].

4.4.1 Superconductivity

In 1911, Onnes discovered that some metals lose their electrical resistance at temperatures around a few Kelvin [116]. The microscopic description of superconductivity was developed by Bardeen, Cooper and Schrieffer in 1957 [117, 118]. Due to electron-phonon interaction, electrons (fermions with spin $1/2$) build Cooper pairs with spin 0. Because of their bosonic nature, Cooper pairs can be described by one quantum mechanical wave function. Phonons are quasiparticles of lattice vibrations in a material, and their number is proportional to temperature. Electrons are scattered by phonons and also by impurities of the material and imperfections of the lattice. This leads to resistivity proportional to temperature, the normal conductance. In contrast to single electrons, Cooper pairs do not interact with phonons, which leads to zero resistivity and a supercurrent [119]. Thermal energy can break the Cooper pairs, having two consequences: (1) Only at low temperatures do Cooper pairs survive and the properties attributed to them become visible; and (2) When thermal energy is deposited on the material, it breaks the Cooper pairs into electrons which experience scattering, producing an increased resistivity.

The temperature of the transition from normal conductivity to superconductivity is called the transition temperature T_c , which is lower when there is an external magnetic field and current in the material. Below T_c , superconducting materials not only lose their resistivity but they also become ideal diamagnets: Magnetic flux is expelled from the material; Flux is trapped within the ring, when the ring becomes

superconducting. This effect, called the Meissner-Ochsenfeld effect, shows that a superconductor magnetically behaves differently from an ideal conductor [120].

4.4.2 Transition-edge sensors

Transition edge sensors (TES) are used in the spectral range from infrared to γ -ray, and the wavelength dictates the superconducting material used: titanium or tungsten for infrared to ultraviolet [24, 121, 122], hafnium for the visible range [123], molybdenum and gold for X-ray [124], and iridium and gold for γ -ray radiation [125]. For optical wavelengths, bare tungsten has a detection efficiency of $\sim 20\%$ [126], bare titanium $\sim 30\%$ [127] and bare hafnium $\sim 40\%$ [123]. The probability of a photon absorption in the superconducting substrate is enhanced by an antireflection coating on the top and a highly reflective mirror below the substrate [128, 129]. The absorbed photon heats up the substrate, which acts as absorber and thermometer at the same time. A specific TES device is optimized for a certain wavelength by the design of this optical structure, which can boost the detection efficiency to nearly 100% [25, 26].

TESs operate in the transition from superconducting to normal conductance. Due to the steep temperature-dependent resistance of the transition edge, the energy deposited by a single photon is sufficient to heat up the substrate and change its resistance. Negative electrothermal feedback keeps the TES at its transition [130]. Figure 4.6 shows a typical readout circuit. To use the Joule heating for the electrothermal feedback the TES is voltage biased. The TES is represented as a variable resistor R_{TES} . When an impinging photon heats up the TES, the resistance increases and current flows through the input coil L_{IN} , which induces magnetic flux in the SQUID. The SQUID works as an amplifier, converting the induced flux into an amplified voltage drop. Room temperature electronics⁵ amplify this signal to the level of tens of mV, which can be processed further with normal electronics.

Although they have the great advantage of being highly efficient, TESs have the disadvantage of being slow. The usual timing jitter for the tungsten devices has long been reported at values around 100ns with recovery time of 2 μ s to 4 μ s, governed by thermal processes [107]. Recently, additional effort has been invested in improving performance speed. For tungsten TESs, additional gold heat sinking has yielded recovery times of 460ns and a timing jitter of 2.5ns, which is a big improvement towards operation of TESs with 80MHz pulsed single photon sources [131, 132]. The detection efficiency for tungsten detectors is 98% to 100% at 805nm and 95% \pm 2%

⁵ XXF-1 from Magnicon

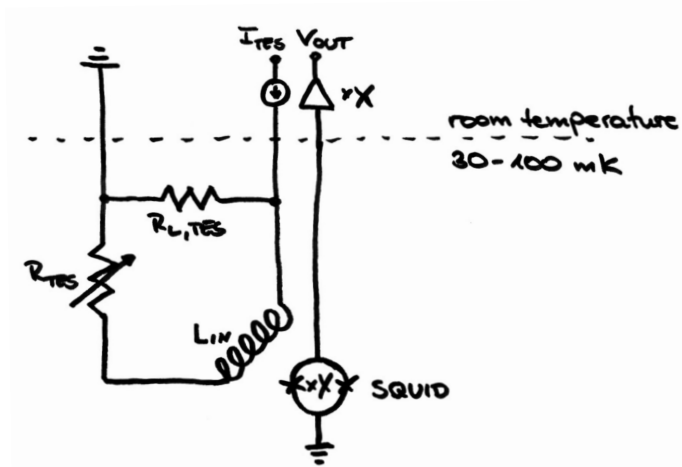


Fig. 4.6: TES read-out circuit. The variable resistor R_{TES} represents the TES, which changes its resistance with temperature. Figure adapted from [24].

at 1550 nm [26]. Titanium TESs have a timing jitter of 25 ns [127] and a recovery time of several hundred nanoseconds [133]. This improvement over tungsten is due to titanium's higher transition temperature of around 400 mK as compared to 100 mK for tungsten TESs. The highest reported detection efficiency for titanium devices for 850 nm is $98\% \pm 1\%$ with an energy resolution of 0.42 eV [25]. For 1550 nm, the detection efficiency is 64% [121]. Research on hafnium TESs promises enhanced detection efficiency in the visible range, because of a layer unnecessary for hafnium but not for tungsten, and faster recovery times due to the higher $T_c \sim 200$ mK. So far only a detection efficiency of 85% and low recovery times are reported, which is attributed to cooling-induced thermal stresses [123]. New materials for the optical structure are explored. To count photons with rates up to GHz at 1550 nm, niobium nano-TESs are proposed [134]. An additional advantage of TESs is that they have no intrinsic dark counts.

The TESs currently used at the presented experiments are made from tungsten, with an optical structure for 850 nm [24, 26]. Images of the TES chip are shown in Fig. 4.7. They are packaged with a single-mode fiber for 1550 nm [135].

4.4.3 Superconducting quantum interference device

The signal from the TES is amplified by an array of superconducting quantum interference devices (SQUID). Details about SQUIDs can be found in Ref. [136, 137]. A dc SQUID, which consists of a superconducting ring with two Josephson junc-

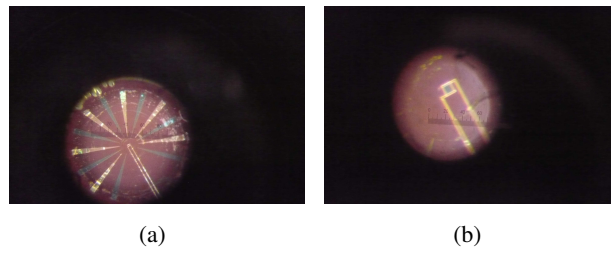


Fig. 4.7: Microscope images of a TES chip (a) and a magnified image of the actual TES with a size of $25\ \mu\text{m} \times 25\ \mu\text{m}$ (b) [24].

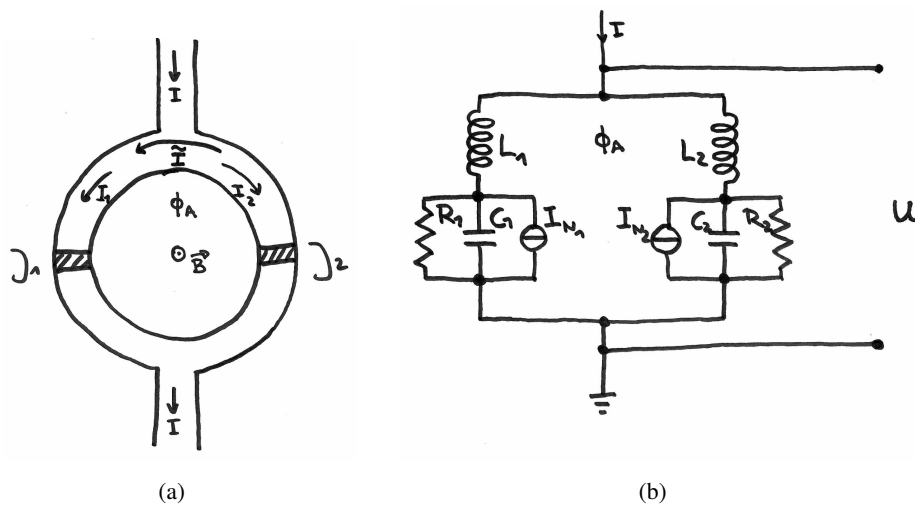


Fig. 4.8: Scheme (a), equivalent circuit (b) of a dc SQUID. Figures adapted from [136].

tions, was first demonstrated by Jaklevic et al. [138]; the first rf SQUID, with only one Josephson junction, was first demonstrated by Silver and Zimmerman [139]. As SQUIDs are susceptible to magnetic field gradients, they are often used as magnetometers and gradiometers. The following provides an overview of dc SQUIDs as these are used for the signal amplification of the TESs.

A SQUID consists of a ring with two Josephson junctions J_1 and J_2 , as shown in Fig. 4.8(a). A Josephson junction is a barrier between two superconductors through which Cooper pairs can tunnel [140–142]. The current I through the junction is described by

$$I = I_0 \sin \delta, \tag{4.10}$$

with I_0 the maximal supercurrent and δ the phase difference between the wave functions of the two superconductors. A second Josephson equation,

$$\frac{\partial \delta}{\partial t} = \frac{2\pi}{\phi_0} U \quad (4.11)$$

relates the voltage U across the junction with the change in phase difference δ over time, where $\phi_0 = \frac{h}{2e} \approx 2.07 \times 10^{-15}$ Vs is the magnetic flux quantum, e the charge of an electron, and h Planck's constant. The SQUID is biased with current I . The magnetic flux ϕ_A of an external magnetic field H enclosed by the ring modulates the current through the junction with a period of the magnetic flux quantum ϕ_0 . Here, the currents through the two Josephson junctions interfere quantum mechanically similar to a double slit experiment [138, 143]. The modulated current is either measured directly or as a voltage U across the SQUID. In this configuration the SQUID works as a flux-to-voltage converter. To work as an amplifier of the TES signal, the input coil L_{IN} of the TES input circuit of Fig. 4.6 induces a magnetic flux ϕ_A through the SQUID. The coupling between the the input coil L_{IN} and the SQUID is called mutual inductance M_{IN} and for practical reasons is characterized as $\frac{1}{M_{IN}} = \frac{i}{\phi_0}$, where i is the current in μ A needed per magnetic flux quantum ϕ_0 . In the presented detection system the TES signal was amplified by a two-stage SQUID, which consists of a single SQUID in the first stage and an array of SQUIDs in the second stage [144]. Instead, a single-stage SQUID array can be used as well [145], but in tests crosstalk from the SQUID working points to the TES working points was observed. The output voltage across the SQUID array is read out by room-temperature electronics⁶ [146, 147].

The operating principle of a SQUID can be also described by the resistively and capacitively shunted junction model (RCSJ-model). Such an equivalent circuit of a dc SQUID is shown in Fig. 4.8(b), with resistance R_i , self-capacitance C_i , current noise source I_{N_i} , and inductance L_i . This model is valid for the simplification to point-like junctions.

4.4.4 Adiabatic demagnetization refrigerator

A detector system consisting of TESs and SQUIDs requires an ambient temperature around 100 mK. To reach those temperatures a dilution refrigerator (DR) or an adiabatic demagnetization refrigerator (ADR) can be used (for description of a DR see [148], for an ADR [149]). The adiabatic demagnetization is an effect also known

⁶ XXF-1 from Magnicon

as magnetocaloric effect [150–152]. In an ADR, paramagnetic salt pills together with a strong superconducting electromagnet exploit this effect. As paramagnets, the molecules of the salt pills have magnetic moments which, due to thermal energy, are aligned randomly. When an external magnetic field is applied, the magnetic moments align along the field direction and the magnetic entropy of the salt pills decreases. This entropy transfers to the thermal degrees of freedom, which increases the temperature of the pills. When the heat is removed from the system, the temperature of the salt pills is brought back to their base temperature. The next step of the cooling cycling is the insulation of the pills and the adiabatic demagnetization. With decreasing external magnetic field the magnetic moments of the salt pills go increasingly out of order, which increases the magnetic entropy. Since the total entropy stays constant, the magnetic degrees of freedom absorb entropy from the thermal degrees of freedom, and the temperature decreases. Slowly, energy from the mounted detectors, the weak thermal link due to the mounting of the salt pills, radiation, and electrical cables leading to the detector heats up the pills which then must repeat the cycle of magnetizing, cooling, and demagnetizing.

The double-stage ADR used for the presented experiment was built by Entropy⁷. All descriptions apply to ADRs in general, but numbers and some details might be specific to the system used. A schematic layout is shown in Fig. 4.9 and pictures of the ADR used are in Fig. 4.10.

The ADR consists of a 70K-stage, a 4K-stage and the paramagnetic salt pills: Gallium Gadolinium Garnet (GGG) at 1K and Ferric Ammonium Alum (FAA) at 100mK. The base temperature at the 4K-stage and the salt pills of ~ 3 K is achieved with a pulse tube cooler⁸. (The 4K-stage is named as such for historical reasons when instead of a pulse tube cooler liquid helium was used for the precooling.) The thermal contact between the two pills and the 4K-stage is provided by a heat switch. When the heat switch is turned off, the pills are mounted in such a way that they are in principle thermally insulated from each other and from the 4K-stage to prevent heating-up from the 4K-stage at the low temperatures of the pills below 1K.

Starting from room temperature, the ADR is first cooled by the pulse tube cooler. The 70K-stage arrives at a temperature of ~ 53 K and, thanks to the thermal contact between pills and 4K-stage provided by the heat switch, the 4K-stage as well as the pills are cooled to the base temperature of ~ 3 K. At this point, the current in the superconducting coil installed around the pills is slowly ramped up to 40 A. The resulting magnetic field of 6 T aligns the spins of the paramagnetic salt which release

⁷ Entropy GmbH, Gmunder Str. 37a, 81379 München, Germany, <http://www.entropy-cryogenics.com>

⁸ SRP-062B-F50H from Sumitomo

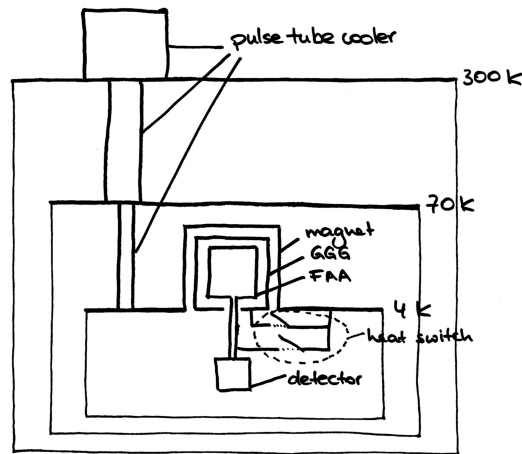


Fig. 4.9: Scheme of an ADR. The ADR stage has to be precooled to a temperature of around 3 K by a two-stage pulse tube cooler. The two salt pills (GGG and FAA) are enclosed by a superconducting magnet. The pills are mounted thermally insulated. The required thermal contact during the cooling cycle is provided by a controllable heat switch.

entropy as heat. The temperature of the pills is increased by a few Kelvin. Using the heat switch, a thermal contact to the 4K-stage is established and the pills in the magnetic field are cooled back to the base temperature. Once there, the heat switch is opened and the current in the magnet is ramped down. This brings the temperature of the GGG pill down to 600mK and the FAA pill to 30mK. The detectors, which are mounted on the FAA pill, perform well for temperatures below 110mK–120mK. When the temperature of the detectors drifts up to 110mK over 8–20 hrs, a new cooling cycle, a recharge, has to be performed. The current in the magnet is ramped up, bringing the pills to temperatures of 5K–6K. Closing the heat switch and thus establishing thermal contact between the 4K-stage and both pills allows the pulse tube cooler to cool down the pills in the magnetic field. When the base temperature is reached and the heat switch is opened, the magnet is ramped down, and the pills reach 600mK and 30mK, respectively.

4.4.5 Counting photons in continuous mode

The counting methods for detection of continuously emitted photons are only sketched here. More details will be explained in Ref. [153] and the PhD thesis of Marissa Giustina who wrote the programs for analysis.

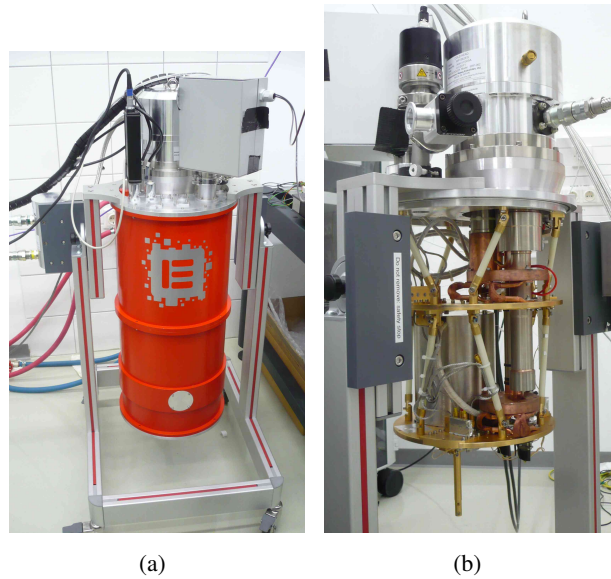


Fig. 4.10: Photographs of the adiabatic demagnetization refrigerator (ADR) in use: (a) closed, (b) opened.

The detector system consisting of TES, SQUID, and room temperature electronics has an analog output signal. The signal has a falling edge with a fall time of 200 ns to 400 ns and a recovery time of 1 μ s to 4 μ s. A representative signal of single 810 nm photons detected by the TES detector system is shown in Fig. 4.11. The signal exhibits a noise band, consisting of electronic noise, the noise of the TES, and the noise of the SQUID; and peaks of detected single photons with the typical shape shown in Fig. 4.11(b). The peak height is proportional to the energy of the absorbed photon, but with a finite energy resolution. Between the noise band and the peaks of 810 nm photons are a few smaller peaks which originate from photons of the blackbody radiation. To make these relations more visible, peak height distributions are calculated from digitized data. To do this, a threshold is set below the zero line but still within the noise band. In between the two crossings of the signal with the threshold, the lowest point is recorded. The absolute values of these extreme points between two crossings are shown in a histogram. A representative histogram for a signal of single photons at 810 nm is shown in Fig. 4.12. The width of the 810 nm peak at 0.07 mV corresponds to the energy resolution of the detection system.

4.4.5.1 Threshold method

For efficient detection of entangled single photon pairs at 810 nm it is required that only 810 nm photons are counted without losing any of them. In the case of an out-

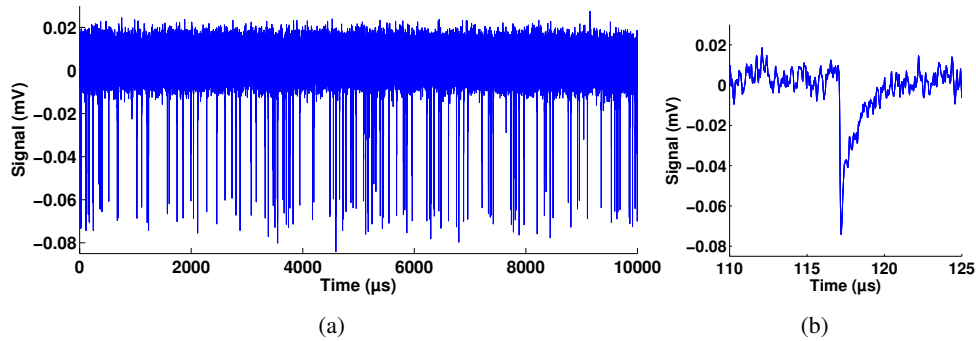


Fig. 4.11: Typical output signal of the TES detector system produced by single 810 nm photons, taken for 10 ms (a) and 15 μ s (b).

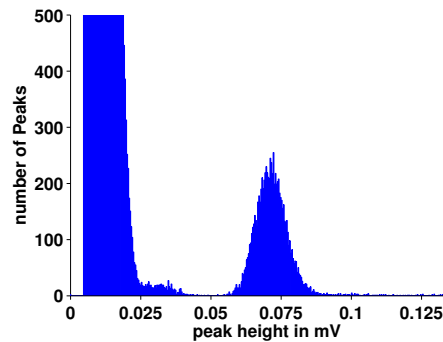


Fig. 4.12: A peak height distribution of a typical output signal of the TES detector system produced by single photons at a wavelength of 810 nm. From the threshold below 0 mV to 0.025 mV is the noise band, from 0.025 mV to 0.045 mV are photons from blackbody radiation and from 0.05 mV to 0.1 mV are detected 810 nm photons.

put signal as shown in Fig. 4.11 and 4.12 the task is relatively easy: the simplest approach is to set a threshold above the noise band, around 0.051 mV according to Fig. 4.12. Anything crossing this threshold is an 810 nm photon. In the case of a less perfect output signal where the noise band is so broad that no blackbody photons can be distinguished and the 810 nm peak overlaps with the noise band, the threshold can only be set at a trade-off point. Some low-height 810 nm peaks are lost, in principle decreasing detection efficiency, and some noise peaks are counted as 810 nm photons. These background counts correspond to dark counts in the case of APDs. One disadvantage of this method is the loss of pulses which are piled up on the recovery edge of a preceding pulse while the signal is still below the threshold. This effect is count rate dependent: for low count rates it is negligible. The other disadvantage

is retriggering, caused by noise on the recovery edge as exhibited on the pulse in Fig. 4.11(b). If such a wiggle crosses the threshold, the same pulse is counted twice. It is possible to avoid that by introducing an artificial dead time which is related to the recovery time. A consequence is the loss of photons at high count rates.

This method can be implemented in realtime using electronics like a leading edge discriminator and a logic module or with self-written programs on digitized data.

4.4.5.2 Subtraction method

To circumvent the problem of photon loss due to pile-up of pulses, a more elaborate method is used in the post-processing of the digitized data. For this method the trace is first scanned for pulses with a fixed threshold and an average pulse is calculated. (In the presence of very high count rates the recovery edge might be distorted.) With the threshold from the peak height distribution, the trace is scanned again and each time a threshold crossing occurs, the previously calculated average pulse is subtracted from the trace. When searched for the next threshold crossing, pile-upped photons will be missed because they are superposed on top of a recovery edge and are too low for the threshold. At the next threshold crossing the procedure is repeated. With this method not all photons are counted in the first round. The trace obtained after the first round of subtractions contains only photons which were previously piled up on a recovery edge of a preceding photon (see Fig. 4.13(b)). On this residual trace the same method is applied (see Fig. 4.13(c)). Depending on the count rates, this can be repeated a few times until no photons are found in a trace. An advantage is that the noise on the recovery edge is immaterial in this method.

4.4.5.3 Coincidences

The presented detection system based on TESs is set up for detection of single photons produced in pairs. Therefore coincidences between two detectors are of interest. In the post-processing of the recorded data, each photon is attributed a time stamp. For both counting methods each photon gets the time stamp of the threshold crossing at which it is counted. Coincidences are found by comparing the time stamps of the traces of the two detectors with a varying delay between them. An example is shown in Fig. 4.14. The width of the curve represents the combined timing jitter of both detectors and the digitizer card. This jitter determines the coincidence window for the experiment. The timing jitter is given as full width at half maximum (FWHM), which corresponds to $2\sqrt{2\ln 2}\sigma$, with σ the standard deviation. Since for a Gaussian distribution $\pm 4\sigma$ cover 99.99 % of the set, the coincidence window for $1\sigma = 42.5$ ns

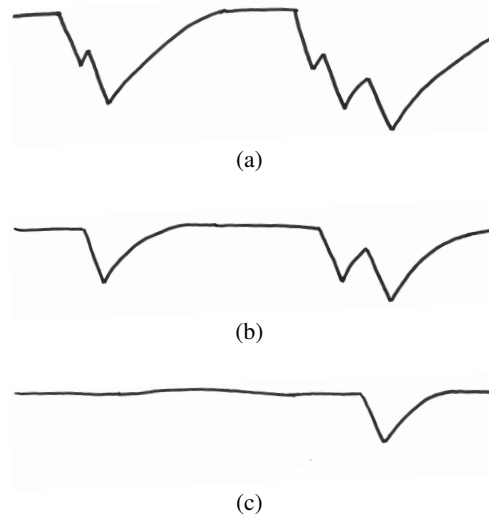


Fig. 4.13: Sketch of the subtraction method: starting with the original trace (a), residual trace after first round of subtraction of photons (b), residual trace after second round of subtraction of photons (c). Each subtracted photon is counted.

corresponding to a timing jitter of 100 ns is $2 \cdot 4\sigma = 339.7$ ns. Compared to the coincidence windows of 4.5 ns used with APDs, a timing jitter of 100 ns results in a coincidence window almost two orders of magnitude longer. As shown in Sec. 3.6, a longer coincidence window causes a higher accidental rate, which is increasingly significant as the count rates increase. However, the error systematically introduced by accidental counts can be corrected in the post-processing. In view of space-like separation for a loophole-free Bell experiment, a longer coincidence window also leads to a larger distance between the source of polarization-entangled photon pairs and their detection. Consequently, the higher losses diminish the overall detection efficiency. That is why any improvement on timing jitter of the TESs is favorable. Improvements of the timing jitter are also conceivable using new methods for the determination of a proper time stamp.

When counted in realtime using analog electronics, the coincidences can be generated with the coincidence (AND) function of a logic module, with the coincidence window determined by the pulse length of the processed input pulses.

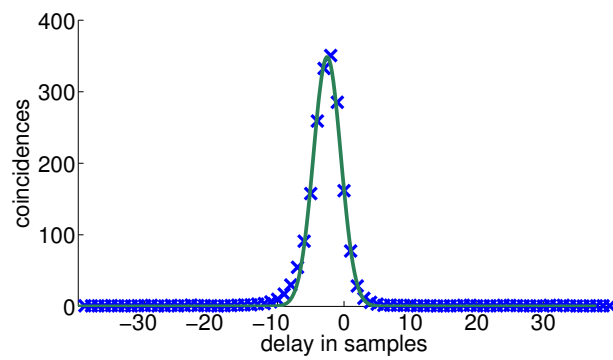


Fig. 4.14: Coincidences plotted over the delay (in samples) between the two detectors. The result of the comparison of the time stamps is shown in blue and a Gaussian fit in green. The calculated curve deviates from the Gaussian fit, because the curve represents the combined timing jitter of two TESs. Due to a sampling rate of 50 MS per second, one sample represents 20 ns.

Characterization of nonmaximally entangled states

The operating principle of the Sagnac source allows the production of nonmaximally entangled states. Since the Sagnac source can produce maximally entangled states with high purity [28], the preparation of pure nonmaximally entangled states is one of the steps that enables a Bell experiment without the need of the commonly used assumption of fair sampling and of locality. The nonmaximally entangled states are characterized by a measurement using conventional avalanche photodiodes.

5.1 State preparation

For the preparation of a certain nonmaximally entangled state in the form of Eq. (3.14) a similar procedure is used to that of the case of maximally entangled states. In that procedure, the angles of minimal coincidences in the basis $\{|DD\rangle, |DA\rangle, |AD\rangle, |DD\rangle\}$ are set for the polarization analysis at Alice and Bob depending on the state, $|\psi_+\rangle$ or $|\psi_-\rangle$. The polarization of the pump beam is adjusted to the minimal coincidence rate using at least one half-wave plate (HWP) and one quarter-wave plate (QWP). The better the overlap of the two pump directions within the Sagnac loop, the lower the minimal coincidence rate and the better the visibility. As described in Secs. 3.4 and 3.5, each nonmaximally entangled state has a unique combination of angles of polarization measurement for minimal and maximal coincidences. For these angles listed in Tab. 5.1, analogously to the preparation of maximally entangled states, minimal coincidence count rates have to be set by changing the polarization of the pump.

5.2 Eberhard with fair sampling

The prepared nonmaximally entangled states are first measured at the polarization angles required for the Eberhard inequality for pure states. Since the detection of the avalanche photodiodes is too low for a violation, fair sampling must be assumed.

Tab. 5.1: The angles for preparation, as the angles of minimal coincidence rates, of the ideal state $|\psi_r\rangle$ as well as of the state ρ'_r . Bob's angle was calculated numerically. It is also defined as $\mp \arctan r$ as described in Secs. 3.4 and 3.5.

η	r	Alice	Bob
66.7%	0.001	$\pm 45.0^\circ$	$\mp 0.06^\circ$
70%	0.136	$\pm 45.0^\circ$	$\mp 7.7^\circ$
75%	0.311	$\pm 45.0^\circ$	$\mp 17.3^\circ$
80%	0.465	$\pm 45.0^\circ$	$\mp 24.9^\circ$
85%	0.608	$\pm 45.0^\circ$	$\mp 31.3^\circ$
90%	0.741	$\pm 45.0^\circ$	$\mp 36.5^\circ$
95%	0.871	$\pm 45.0^\circ$	$\mp 41.1^\circ$
100%	1	$\pm 45.0^\circ$	$\mp 45.0^\circ$

5.2.1 Experimental setup

Seven of the eight states listed in Tabs. 3.2 and 5.1 are prepared using the Sagnac source. The polarization measurement at Alice and Bob is performed with a HWP and a polarizing beam splitter (PBS) within a fiber bridge, as shown in Fig. 5.1. In this setup, avalanche photodiodes (APDs) with roughly 40% detection efficiency are used as detectors. Together with the losses from coupling into the single mode fiber at the source, the coupling from single mode to multimode fiber through wave plates and a PBS in the fiber bridge, as well as reflections on surfaces add up to an overall detection efficiency of 9%–11%. This is far below the threshold of $2/3$ needed for a violation of the Bell inequality with nonmaximally entangled states. For each state, the four outputs (two outputs of two PBSs) were measured in all combination of angles α_i and β_j required for an evaluation of the Eberhard inequality (3.1), but also their orthogonal angles α_i^\perp and β_j^\perp . To ensure the same detection efficiency for all count rates, the data listed in Tab. 5.2 was measured at one output of each PBS. For the counts n_{oe} and n_{eo} the half-wave plate in front of the PBS was rotated by additional 45° . The data was taken for 20s for each setting.

5.2.2 Results

A way to evaluate data with a detection efficiency too low for a violation of the Eberhard inequality is to only consider coincidences as was done by Brida et al. in [79]. Instead of the inequality (3.1) only the detected events are used: $J_{det} = n_{oe}(\alpha_1, \beta_2) + n_{eo}(\alpha_2, \beta_1) + n_{oo}(\alpha_2, \beta_2) - n_{oo}(\alpha_1, \beta_1) \geq 0$. As already shown

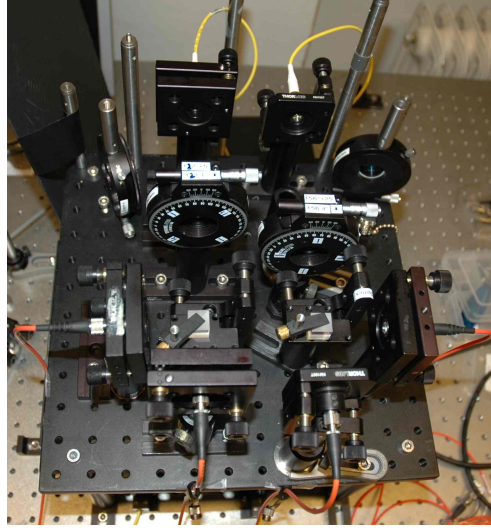


Fig. 5.1: Fiber bridge. Photons are coupled out of a single mode fiber, pass a HWP and a PBS for polarization analysis and exit the two outputs of the PBS. There they are coupled into multimode fibers which are connected to APDs. For state tomography an additional QWP has to be inserted in front of the PBS.

in Sec. 3.3 this is equal to the negative of the CH inequality assuming fair sampling. To make the violation comparable independent of the actual count rates, the value for J_{det} is normalized by the detected single count rates N to $J_{\text{det}}^{\text{norm}} = J_{\text{det}}/N$. The detected count rates N are calculated as the average of the sum of Alice's singles at angles α_i and α_i^\perp and of Bob's singles at angles β_j and β_j^\perp . This quantity is independent of the state and is closely related to the pair production rate of the source. The value J_{det} is plotted versus the detection efficiency in Fig. 5.2. The violation of the inequality $J_{\text{det}}^{\text{norm}} \geq 0$ is larger for higher efficiencies, for which the parameters r , α_1 , α_2 , β_1 , and β_2 were optimized, although all data was measured using the same setup. Since fair sampling is assumed and no space-like separation was established, only a class of hidden-variables can be refuted that exploits neither the low detection efficiency of the experiment nor communication between Alice and Bob or the setting choice nor the choice of measurement setting.

5.3 State tomography

For characterization of the prepared nonmaximally entangled states, state tomography is performed. The reconstructed density matrices allow the calculation of quantities, such as fidelity \mathcal{F} , tangle \mathcal{T} and purity \mathcal{P} .

Tab. 5.2: Number of coincidence counts (cc) and single counts of Alice (S_1) and Bob (S_2) measured in 20s. The uncertainty can be calculated as Poissonian errors. The data is measured at one of the outputs of each PBS. The efficiency η represents the state and the measurement angles for the Eberhard inequality, not the actual overall detection efficiency. To measure the setting $\alpha_1\beta_{2oe}$ for example, the wave-plates were set to $\alpha_1/2$ and $\beta_2/2 + 45^\circ$.

η	setting	cc	S_1	S_2	η	setting	cc	S_1	S_2
70 %					75 %				
	$\alpha_1\beta_{1oo}$	1010	29923	35547		$\alpha_1\beta_{1oo}$	4937	67794	69884
	$\alpha_1\beta_{2oe}$	134	29626	482523		$\alpha_1\beta_{2oe}$	430	69243	377304
	$\alpha_2\beta_{1eo}$	147	461041	35436		$\alpha_2\beta_{1eo}$	496	381948	70122
	$\alpha_1\beta_{1oo}$	50	84714	105402		$\alpha_1\beta_{1oo}$	95	150084	164552
80 %					85 %				
	$\alpha_1\beta_{1oo}$	8157	105875	108804		$\alpha_1\beta_{1oo}$	18244	208100	217821
	$\alpha_1\beta_{2oe}$	738	107554	367277		$\alpha_1\beta_{2oe}$	2189	207553	460387
	$\alpha_2\beta_{1eo}$	904	364154	111682		$\alpha_2\beta_{1eo}$	2392	450389	216272
	$\alpha_1\beta_{1oo}$	270	189230	213848		$\alpha_1\beta_{1oo}$	925	297313	325192
90 %					95 %				
	$\alpha_1\beta_{1oo}$	17348	195382	207357		$\alpha_1\beta_{1oo}$	28988	314000	330149
	$\alpha_1\beta_{2oe}$	2687	201373	323793		$\alpha_1\beta_{2oe}$	4989	310399	402636
	$\alpha_2\beta_{1eo}$	2715	308261	212343		$\alpha_2\beta_{1eo}$	5065	384743	329981
	$\alpha_1\beta_{1oo}$	1673	243462	263420		$\alpha_1\beta_{1oo}$	3551	346821	366042
100 %									
	$\alpha_1\beta_{1oo}$	24530	263750	278049					
	$\alpha_1\beta_{2oe}$	4458	262576	291822					
	$\alpha_2\beta_{1eo}$	3781	276271	276254					
	$\alpha_1\beta_{1oo}$	3556	266391	285597					

5.3.1 Experimental setup

The state of a quantum system is in general described by a density matrix $\rho = \sum_i p_i |\psi_i\rangle\langle\psi_i|$. For a pure quantum system the density matrix simplifies to $\rho = |\psi\rangle\langle\psi|$, such that the state vector $|\psi\rangle$ is a sufficient description. The density matrix of a state prepared by the Sagnac source, as any other state, can be reconstructed from a set of measurements in the H/V -, D/A -, and R/L -bases. For measurements in the R/L -basis (right and left circular), in addition to the HWP and the PBS a QWP is needed within the fiber bridge, which is shown in Fig. 5.1. The coincidence counts listed in Tab. 5.4 were detected at both outputs of the two PBSs at nine settings of the wave

Tab. 5.3: J_{det} is the parameter of the inequality (3.1) when only detected events are taken into account. It is the negative value of the CH inequality under the fair sampling assumption. N is the detected number of singles, J_{det}^{norm} is the parameter J_{det} normalized to N . Data was taken for 20s. The inequality is violated for $J < 0$.

η	r	J_{det}	N	J_{det}^{norm}
70%	0.136	-679 ± 37	560877 ± 176	-0.00121 ± 0.00007
75%	0.311	-3916 ± 77	534796 ± 176	-0.0073 ± 0.0001
80%	0.465	-6245 ± 100	560727 ± 176	-0.0111 ± 0.0002
85%	0.608	-12738 ± 154	762196 ± 205	-0.0167 ± 0.0002
90%	0.741	-10273 ± 156	563480 ± 176	-0.0182 ± 0.0003
95%	0.871	-15383 ± 206	747800 ± 203	-0.0206 ± 0.0003
100%	1	-12735 ± 191	559025 ± 175	-0.0228 ± 0.0003

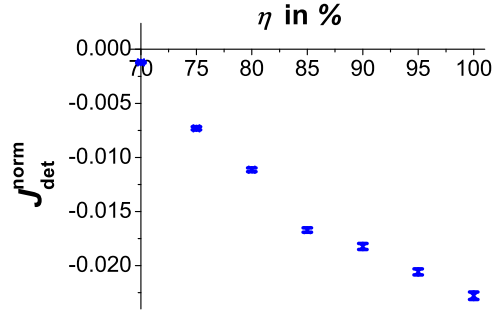


Fig. 5.2: The normalized parameter J_{det}^{norm} from Tab. 5.3 is plotted against the detection efficiency η for which the state and the measurement angles were optimized for.

plates. The data was measured for 20s. From these 32 coincidence counts a density matrix ρ_{meas} is reconstructed using the maximum likelihood method [105] and plotted in Fig. 5.3. For orientation, the respective ideal pure state $|\psi_r\rangle\langle\psi_r|$ is shown together with the measured density matrix ρ_{meas} in the same chart. From the reconstructed density matrices of the prepared states, quantities characterizing the state can be derived. The uncertainties of these quantities are calculated with a Monte Carlo routine assuming Poissonian noise.

Tab. 5.4: Coincidence counts used for the reconstruction of the density matrix.

The settings of each the row (such as HD) indicate the angles of the measured polarization (H for Alice, D for Bob). The combinations of o s and e s in the columns (oo, oe, eo and ee) specify at which outputs of the PBS the counts were detected. The output in transmission is labeled o , the output in reflection, where the measured polarization is orthogonal to the original setting, is labeled e . The number of counts for VD is written at row HD and column eo . Data was taken for 20s. The uncertainties can be calculated as Poissonian errors.

setting	oo	oe	eo	ee	setting	oo	oe	eo	ee
70%					75%				
HH	58	61430	1061	337	HH	77	59098	5695	307
HD	26044	31282	338	1100	HD	24948	29788	2369	4145
HR	25523	32174	716	620	HR	24242	30486	3297	3009
DH	407	30313	664	40692	DH	2709	28903	3004	36763
DD	16338	11145	12883	25240	DD	21214	6063	7571	31165
DR	13263	15324	16545	21776	DR	12326	16423	16797	19768
RH	473	31973	576	33758	RH	2383	30612	3045	31379
RD	13675	16622	14475	17361	RD	15298	16538	13655	18621
RR	17071	12955	10628	22787	RR	22534	7968	6096	28444
80%					85%				
HH	97	65936	12065	355	HH	113	63071	20987	394
HD	27893	31978	5181	8591	HD	28130	30691	9444	13976
HR	26860	34077	6693	6835	HR	25602	33059	11634	11577
DH	5977	32105	6225	41537	DH	10248	32731	11251	39110
DD	28738	4407	6176	41611	DD	36043	2215	3724	49923
DR	18148	17928	17902	27264	DR	17344	25345	24290	25487
RH	5225	34407	6295	35540	RH	9044	33679	11258	34055
RD	16005	20937	18510	20640	RD	18925	22217	19679	24828
RR	28880	5934	4380	37777	RR	35327	3419	2341	46162
90%					95%				
HH	82	38035	19475	194	HH	138	48522	34415	307
HD	16975	18469	8997	12485	HD	21523	23245	16114	22370
HR	16113	20181	10288	10839	HR	19793	25535	18357	19699
DH	10221	18929	9837	23404	DH	17593	24705	17326	31336
DD	25513	427	1182	32856	DD	38333	116	725	51644
DR	13719	14560	14527	17832	DR	18487	23676	22260	24817
RH	8902	20742	10268	21097	RH	14958	25868	18547	26217
RD	12618	16068	14992	16032	RD	19217	20870	19178	25482
RR	25903	1149	790	32950	RR	36541	509	299	48181
100%									
HH	90	26357	30818	183					
HD	14947	12570	14176	16761					
HR	13151	14383	16020	14997					
DH	15260	13538	15914	19656					
DD	30398	223	139	37364					
DR	14821	15207	16106	18104					
RH	13106	14595	16921	16377					
RD	13605	13742	15244	16009					
RR	27706	134	261	32879					

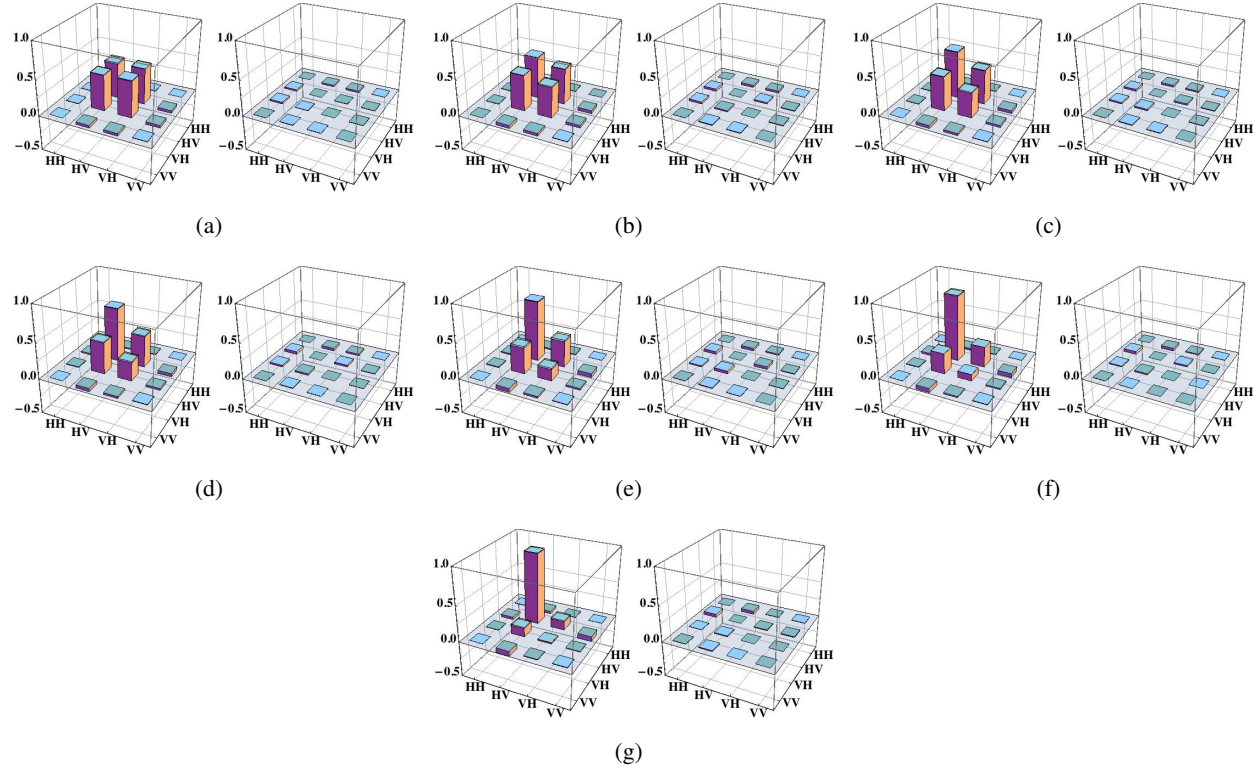


Fig. 5.3: The real part and the imaginary part of the reconstructed density matrix for the target states $|\psi_{r=1}\rangle$ designed for $\eta = 100\%$ (a), $|\psi_{r=0.871}\rangle$ designed for $\eta = 95\%$ (b), $|\psi_{r=0.741}\rangle$ designed for $\eta = 90\%$ (c), $|\psi_{r=0.608}\rangle$ designed for $\eta = 85\%$ (d), $|\psi_{r=0.465}\rangle$ designed for $\eta = 80\%$ (e), $|\psi_{r=0.311}\rangle$ designed for $\eta = 75\%$ (f), and $|\psi_{r=0.136}\rangle$ designed for $\eta = 70\%$ (g) are shown. For comparison the respective ideal matrices $|\psi_r\rangle\langle\psi_r|$ are included in transparent yellow.

5.3.2 Results

To assess the quality of the state preparation, the fidelity \mathcal{F} is calculated. It is a distance measure defined as

$$\mathcal{F} = \left(\text{tr} \left(\sqrt{\sqrt{\rho} \sigma \sqrt{\rho}} \right) \right)^2 \quad (5.1)$$

for two arbitrary density matrices ρ and σ with the square root of the density matrix defined as $\sqrt{\rho} \sqrt{\rho} = \rho$ [154]. When the fidelity is $\mathcal{F} = 1$, the prepared state ρ is equal to the target state σ . For a pure state $|\psi\rangle$ and an arbitrary state ρ the formula simplifies to

$$\mathcal{F} = \langle \psi | \rho | \psi \rangle. \quad (5.2)$$

The fidelities of the reconstructed density matrices ρ_{meas} are calculated for three different types of states: the ideal pure state $|\psi_r\rangle$ of Eq. (3.2), the mixed Werner state ρ_W , and the mixed state ρ'_r introduced in Sec. 3.5. Werner states

$$\rho_W = (1 - V) |\psi_r\rangle \langle \psi_r| + V \frac{1}{4} \mathbb{1}_4, \quad (5.3)$$

with $|\psi_r\rangle$ of Eq. (3.2), visibility V , and a 4×4 identity matrix $\mathbb{1}_4$ are used for the description of the produced state when the noise in the experiment is white noise [155]. The states of Eq. (3.14),

$$\rho'_r = \frac{1}{1 + r^2} \begin{pmatrix} 0 & 0 & 0 & 0 \\ 0 & 1 & Vr & 0 \\ 0 & Vr & r^2 & 0 \\ 0 & 0 & 0 & 0 \end{pmatrix},$$

are used in the optimization routine of the state and the measurement angles described in Sec. 3.5. Both the Werner state ρ_W and the states ρ'_r are more mixed with decreasing visibility V . The fidelities listed in Tab. 5.5 and plotted in Fig. 5.4 are calculated for these three states with an assumed visibility of $V = 99\%$. The average preparation fidelities are $\bar{\mathcal{F}} = 99.01\% \pm 0.01\%$ for the pure ideal state $|\psi_r\rangle$, $\bar{\mathcal{F}} = 98.90\% \pm 0.01\%$ for the Werner state ρ_W , and $\bar{\mathcal{F}} = 99.00\% \pm 0.01\%$ for the state ρ'_r . These are very high values, which indicate that all three states describe the produced state very well, with the largest distance for the Werner state. The fidelities of the three states weakly depend on the parameter r : the fidelity increases with increasing r . Either the states prepared for lower values of r are more sensitive to preparation or neither of the three states offers a sufficient description for the produced states determined by the parameters r . To explore how sensitive fidelity is to a

Tab. 5.5: Fidelities \mathcal{F} of the reconstructed states are calculated for the pure ideal state $|\psi_r\rangle$, the mixed Werner state ρ_W , and the mixed state ρ'_r for a visibility of $V = 99\%$.

η	r	$\mathcal{F}_{ \psi_r\rangle}$	\mathcal{F}_{ρ_W}	$\mathcal{F}_{\rho'_r}$
70%	0.136	98.70% \pm 0.02%	98.61% \pm 0.02%	98.81% \pm 0.02%
75%	0.311	98.86% \pm 0.04%	98.80% \pm 0.02%	99.04% \pm 0.02%
80%	0.465	98.90% \pm 0.03%	98.70% \pm 0.01%	98.80% \pm 0.03%
85%	0.608	99.03% \pm 0.03%	98.89% \pm 0.01%	98.82% \pm 0.03%
90%	0.741	99.24% \pm 0.03%	99.05% \pm 0.01%	99.15% \pm 0.05%
95%	0.871	99.23% \pm 0.02%	98.97% \pm 0.01%	99.02% \pm 0.02%
100%	1	99.11% \pm 0.02%	99.27% \pm 0.05%	99.36% \pm 0.03%

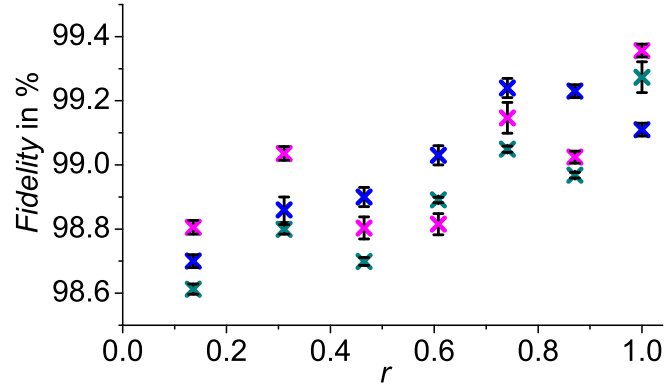


Fig. 5.4: Fidelities \mathcal{F} listed in Tab. 5.5 are plotted against the parameter r for which they were prepared: the fidelity for the pure ideal state $|\psi_r\rangle$ in blue, for the Werner state ρ_W in green, and for the state ρ'_r in magenta.

preparation of a wrong nonmaximally entangled state determined by its parameter r , the fidelities of two ideal states $|\psi_r\rangle$ each with a different parameter r are calculated as $|\langle\psi_{r_1}|\psi_{r_2}\rangle|^2$ and listed in Tab. 5.6. In this table the states with adjacent parameters r have high fidelities ranging from 97.26% up to nearly 100%, although the states have very different parameters r and tangle \mathcal{T} . The fidelity of the state $|\psi_{r=0.311}\rangle$ (optimized for the expected overall detection efficiency of the setup of 75%) with the neighboring state $|\psi_{r=0.136}\rangle$ (optimized for 70%) is 97.26%. The fidelity of the state $|\psi_{r=0.311}\rangle$ with the state $|\psi_{r=0.465}\rangle$ (optimized for 80%) is 98.22%. The measured fidelity of the state $|\psi_{r=0.311}\rangle$ with all three target states $|\psi_r\rangle$, ρ_W and ρ'_r ranges in the region between 98.8% and 99.1%. This demonstrates, that the fidelity \mathcal{F} is not a very sensitive measure for the purpose of qualifying the preparation.

Tab. 5.6: Fidelities \mathcal{F} calculated between two ideal states $|\psi_r\rangle$ with each a different parameter r specific to a detection efficiency η . Two states with neighboring parameters r have fidelities ranging from 97.3 % to 100 % despite their very different magnitude of entanglement measured as tangle \mathcal{T} (see Tab. 3.1).

η	r	0	66.7%	70%	75%	80%	85%	90%	95%	100%
		0	0.001	0.136	0.311	0.465	0.608	0.741	0.871	1
	0	1	0.999999	0.98184	0.911809	0.822216	0.730106	0.645544	0.568621	0.5
66.7%	0.001	0.999999	1	0.982106	0.912375	0.822298	0.730993	0.6465	0.569611	0.501
70%	0.136	0.98184	0.982106	1	0.972583	0.912619	0.840298	0.768006	0.698395	0.63353
75%	0.311	0.911809	0.912375	0.972583	1	0.98222	0.941278	0.891165	0.837407	0.783573
80%	0.465	0.822216	0.822298	0.912619	0.98222	1	0.987724	0.959568	0.922934	0.882331
85%	0.608	0.730106	0.730993	0.840298	0.941278	0.987724	1	0.991663	0.971284	0.943904
90%	0.741	0.645544	0.6465	0.768006	0.891165	0.959568	0.991663	1	0.993797	0.978348
95%	0.871	0.568621	0.569611	0.698395	0.837407	0.922934	0.971284	0.993797	1	0.995269
100%	1	0.5	0.501	0.63353	0.783573	0.882331	0.943904	0.978348	0.995269	1

Tab. 5.7: The parameter r_{meas} calculated from the reconstructed density matrix shown in Fig. 5.3 in comparison to r_{ideal} , the ideal parameter r .

η	r_{ideal}	r_{meas}
70 %	0.136	0.131
75 %	0.311	0.316
80 %	0.465	0.438
85 %	0.608	0.585
90 %	0.741	0.722
95 %	0.871	0.853
100 %	1	1.028

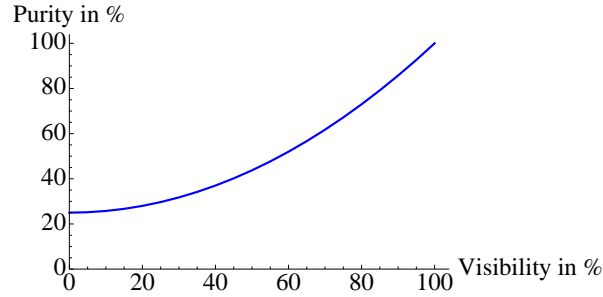
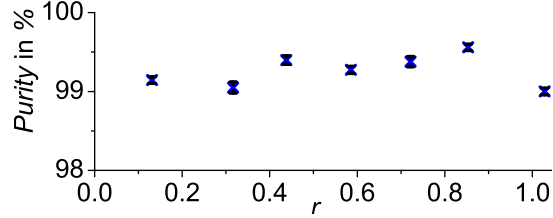
Another approach to qualify the state preparation is to compare the parameter r of the reconstructed density matrix ρ_{meas} , labeled r_{meas} , to the parameter r of the ideal state. For a pure state $|\psi_r\rangle$, the parameter r can be calculated from the ratio of the population of the $|VH\rangle\langle VH|$ and $|HV\rangle\langle HV|$ entries of the density matrix $\rho = |\psi_r\rangle\langle\psi_r|$ as

$$r = \sqrt{\frac{\text{tr}(|VH\rangle\langle VH|\rho)}{\text{tr}(|HV\rangle\langle HV|\rho)}}. \quad (5.4)$$

The parameter r_{meas} listed in Tab. 5.7 are calculated in the same way according to Eq. (5.4), with uncertainties of less than $2 \cdot 10^{-15}$ for all values calculated with the Monte Carlo routine. Since for a given experimental situation defined by the overall detection efficiency η an optimal parameter r of the state and the angles for the measurement of the correlations α_1 , α_2 , β_1 and β_2 are optimized for a maximal violation of the Eberhard inequality, it is interesting to investigate what the consequences are, if a state with a different parameter is prepared instead. Therefore, a set of measurement angles is optimized for a given experimental situation and states with a deviating, less-than-ideal parameter r are evaluated. The theoretical experimental setting is a source that produces states with a visibility of 98 %, no dark or background counts, a rate of 1 and a short coincidence window of 0.04 ns to avoid accidental counts. The optimal parameter r for the assumed detection efficiency of 80 % is $r = 0.450$. The states with the deviating parameter $r = 0.4$ and $r = 0.5$ have fidelities with the ideal state of $\mathcal{F} = 98.82\%$ and $\mathcal{F} = 98.83\%$, respectively. These states violate the inequality 5 % less, whereas the reconstructed density matrix with a parameter $r = 0.438$ exhibits a violation decreased by 25 %. In the same way, deviations from the ideal parameters $r = 1$ for a detection efficiency of 100 % by 10 % was evaluated. In this case, the violation is decreased by less than 1 %, showing that the lower the

Tab. 5.8: The purity \mathcal{P} of the reconstructed density matrices of Fig. 5.3 are listed, with uncertainties of all \mathcal{P} below 0.07 %.

η	r	\mathcal{P}
70 %	0.136	99.1 %
75 %	0.311	99.1 %
80 %	0.465	99.4 %
85 %	0.608	99.3 %
90 %	0.741	99.4 %
95 %	0.871	99.6 %
100 %	1	99 %

**Fig. 5.5:** The purity of Werner states ρ_W as a function of visibility V . It depends on the visibility, but remains the same value independent of the parameter r .

parameter r , the stronger the decrease of the violation due to a deviating parameter r . These investigations imply that the decreased violation cannot be attributed to a preparation of a state with a different parameter r , but might result from other imperfections, such as noise.

Since the target states of the preparation are pure states, the purity is an important quantity for the characterization of the prepared states. Purity \mathcal{P} is defined as $\mathcal{P} = \text{tr}(\rho^2)$: for a pure state $\text{tr}(\rho^2) = 1$, for a mixed state $0 \leq \text{tr}(\rho^2) < 1$. From the reconstructed density matrix ρ_{meas} it is calculated as $\mathcal{P} = \text{tr}(\rho_{meas}^2)$ and summarized for all seven states in Tab. 5.8. The measured purities scatter more than their uncertainties independent of the parameter r , but with a trend to higher purities for higher parameters r . The average purity is $\bar{\mathcal{P}} = 99.26 \% \pm 0.02 \%$. For a comparison the purity of the two mixed states is calculated. The purity of a Werner state ρ_W is independent of the parameter r , but it increases with increasing visibility V as shown in Fig. 5.5. For states ρ'_r of Eq. (3.14) used in the simulation described in Sec. 3.5, the purity depends on both the visibility V and the parameter r , which is plotted in

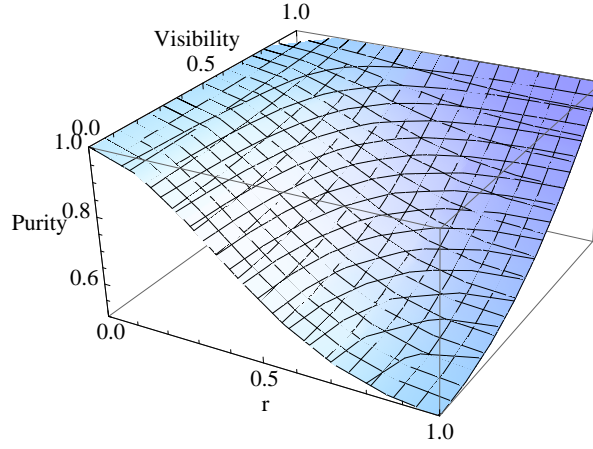


Fig. 5.6: Purity as a function of the parameter r and visibility for the state ρ'_r .

Tab. 5.9: For the reconstructed density matrices the tangle \mathcal{T}_{meas} is calculated and compared to the tangle of the ideal state \mathcal{T} .

η	r	\mathcal{T}	\mathcal{T}_{meas}	$\frac{\mathcal{T}_{meas}}{\mathcal{T}}$
70 %	0.136	0.0713	0.0526 ± 0.0007	$73.80 \% \pm 0.99 \%$
75 %	0.311	0.3217	0.3123 ± 0.0013	$97.09 \% \pm 0.40 \%$
80 %	0.465	0.5847	0.5228 ± 0.0011	$89.41 \% \pm 0.19 \%$
85 %	0.608	0.7882	0.7414 ± 0.0008	$94.07 \% \pm 0.10 \%$
90 %	0.741	0.9153	0.8811 ± 0.0013	$96.26 \% \pm 0.14 \%$
95 %	0.871	0.9812	0.9566 ± 0.0005	$97.49 \% \pm 0.05 \%$
100 %	1	1	0.9741 ± 0.0008	$97.41 \% \pm 0.08 \%$

Fig. 5.6. It decreases with increasing parameter r and increases with increasing visibility V . For a visibility of $V = 98\%$ the purity decreases from $\mathcal{P} = 100\%$ for a product state with $r = 0$ to $\mathcal{P} = 98.02\%$ for a maximally entangled state with $r = 1$. The decreasing behavior for higher values of the parameter r of the states ρ'_r is in contradiction to the observed behavior of the measured data of Tab. 5.8.

For a characterization of the prepared nonmaximally entangled states, it is also interesting to measure the entanglement. The calculated values of the tangle \mathcal{T} of the reconstructed density matrices are compared to the tangle of the ideal target states $|\psi_r\rangle$ in Tab. 5.9. The reconstructed density matrices are all less entangled than the respective ideal states $|\psi_r\rangle$, although not all measured states have a lower value of the parameter r than their target states (see Tab. 5.7).

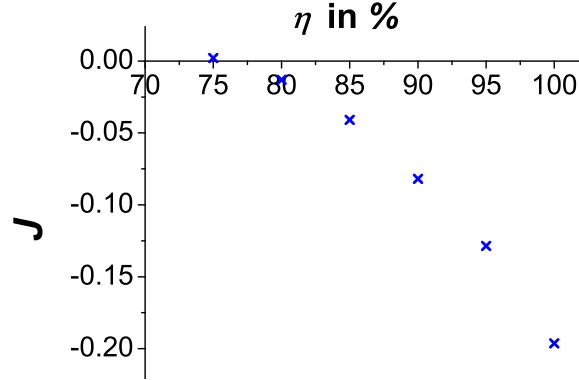


Fig. 5.7: The parameter J of Eberhard's version of the CH inequality calculated from reconstructed density matrix ρ_{meas} plotted versus the efficiency η .

Measurement values of an observable M , represented by the operator \hat{M} , can be calculated from a density matrix ρ by the operation $\text{tr}(\hat{M}\rho)$. Using the measurement operators required for the evaluation of the Eberhard inequality the value J of Eq. (3.20) can be calculated for the prepared states represented by the reconstructed density matrices ρ_{meas} . In Fig. 5.7 the normalized values for the parameter J are plotted versus the detection efficiency η for which these states were prepared. The same value of η is assumed as the overall detection efficiency for the respective evaluation of the value J . The calculations are motivated by a measurement with TESs including dark and background counts and accidental coincidences. The assumed parameters of the calculation are therefore a coincidence window of 400 ns, a dark and background count rate of 10 Hz, and a pair production rate of 30 kHz, with which J is normalized. The measurement angles used for this evaluation are those optimized for the corresponding ideal states $|\psi_r\rangle$ of Eq. (3.2). The non-ideal density matrix ρ_{meas} and the experimental imperfections of the TES detection system built in by the long coincidence window and the dark and background rate cause a diminished violation. As a consequence, the Eberhard inequality cannot be violated for an overall detection efficiency of $\eta = 75\%$. To achieve a violation in an experimental setup with states prepared in the same quality either the overall detection efficiency has to be above 75% or the experimental imperfections of the detection system need to be improved.

5.4 Summary

The highest values of the fidelity of the prepared states were achieved for both the ideal state $|\psi_r\rangle$ and the state with the reduced visibility in the coherence terms ρ'_r as used for the optimization routine. The average fidelities for both states are over-

lapping within their uncertainties. The prepared states have a high average purity of $\bar{\mathcal{P}} = 99.26\% \pm 0.02\%$, but it indicates that they should be described by a mixed state. The behavior of the purity as a function of the parameter r for the state ρ'_r deviates from the measurement while the ideal state and the Werner state give an agreeing description. The measured data violates the Bell inequality when only coincidences are taken into account. For nonmaximally entangled states prepared in the same quality as presented in this chapter, a violation is predicted by the calculation on the reconstructed density matrices for a detection efficiency above 75% .

Highly-efficient heralding

To enable a Bell experiment without the assumption of fair sampling, not only highly efficient detectors are needed, but also a highly efficient setup. Therefore low-loss components with antireflection (AR) coating are used. The overall efficiency for a setup with TESs as single-photon detectors is mainly determined by the ability of coupling both partners of a photon pair in the respective fibers leading to the detectors (output 3 and 4 in Fig. 4.3). The fibers used in the packaging of the TES are single-mode fibers for 1550 nm (SMF28)⁹ with a core diameter of 8.2 μm . The core diameter is chosen according to the size of the TES and the ability to center the fiber core and the TES.

The overall detection efficiency, including all losses from pair production to detection, can be determined using the process of SPDC. In this process the photons are only produced in pairs. In the ideal case of perfect overall detection efficiency, with the detection of a photon at Alice the partner photon will be detected at Bob as well. The ratio of the coincident counts n_{oo} and Alice's single counts S_{o-} determines the overall detection efficiency of Bob η_B as $\eta_B = \frac{n_{oo}}{S_{o-}}$. For a detection efficiency of 100% the same number of coincidences n_{oo} as singles S_{o-} at Alice is registered. When photons are lost at Bob, the number of coincidence counts n_{oo} is decreased and with it decreases the ratio between coincidence counts and Alice's single counts, the overall detection efficiency η_B . When photons are lost at Alice's channel the number of her single counts S_{o-} and the coincidence counts n_{oo} are decreased by the same factor, such that their ratio, Bob's detection efficiency η_B , is unchanged. For a realistic setup, not only the overall detection efficiencies are not 100%, but also both the photons detected at Alice and the photons detected in coincidence at Bob might be false counts due to background light or intrinsic dark count photons of the single-photon detectors. These modify the determined detection efficiency η_B to η'_B . Of

⁹ SMF-28e from Corning

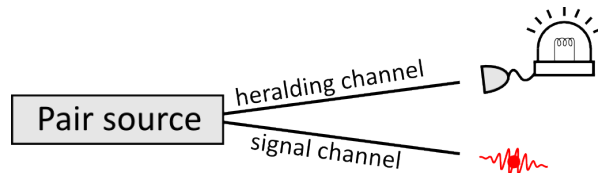


Fig. 6.1: Heralded single-photon source based on SPDC.

course the reverse is also true: A photon detected at Bob heralds its partner photon at Alice and allows the determination of Alice’s detection efficiency $\eta_A = \frac{n_{oo}}{S_{-o}}$. For a violation of a Bell inequality without additional assumptions on detection, the overall detection efficiencies of Alice and Bob have to exceed the detection threshold of $2/3$ for nonmaximally entangled states in the ideal case of any noise sources. With additional background counts the required efficiency is even higher.

An efficient heralding of one of the channels can be achieved with an asymmetric setup, where only the heralded channel is highly efficient. Such a setup can be used as a heralded single-photon source. Single-photon sources [107, 156, 157] are a useful resource for quantum key distribution [158, 159], quantum computation [160–162], random number generation [163, 164] and metrology [165, 166]. An ideal single-photon source should emit truly single photons on demand. A single-photon source based on SPDC is probabilistic, but the presence of a photon in one channel is heralded by the detection of its partner photon, which allows the construction of an on-demand source using additional techniques, such as single-photon storage or multiplexing of sources [167–170]. With increased pump power the signal channel (defined as shown in Fig. 6.1) can contain multiple photons from higher order contribution, where two or more photon pairs are produced instead of only one photon pair. Most single-photon detectors, such as APDs, do not have the capability of resolving the number of photons hitting the detector. In the case of an emission of multiple pairs, a click in the APD of the heralding channel would herald two or more photons instead of one. These higher order contributions are negligible for low pump powers, but they have the consequence of limited count rates. Some single-photon detectors, such as TESs, do resolve photon-number. This can be used to ignore events where more than one photon was detected in the heralding channel.

6.1 Experimental setup

A scheme of the used setup is shown in Fig. 6.2. The Sagnac source as presented in Sec. 5 is used for the production of pairs. For heralding it is sufficient to pump in

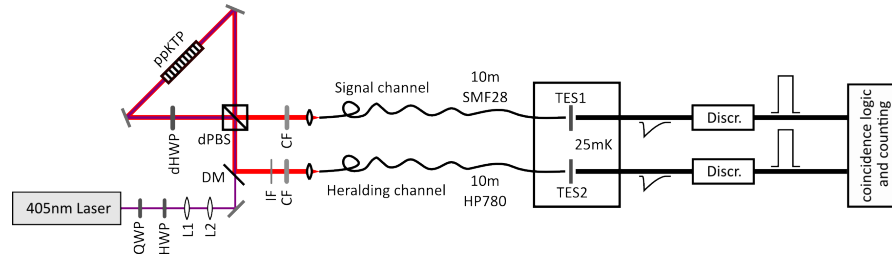


Fig. 6.2: Setup of the heralding experiment. L1, L2 – lens, DM – dichroic mirror, dPBS – dual-wavelength polarizing beam splitter, dHWP – dual-wavelength half-wave plate, IF – interference filter, CF – cut-off filter. Photon pairs produced within the Sagnac-loop are coupled into fibers (SMF28 – single-mode fiber for 1550nm, HP780 – single-mode fiber for 810nm) which lead to the dilution refrigerator to the TESs. The produced signal is discriminated at room temperature and further processed with a coincidence logic and then counted.

one direction only producing a product state. At both outputs of the Sagnac loop a cut-off filter for suppression of 405 nm pump light is used. In the heralding channel additional spectral and spatial filtering is implemented to make sure that only down-conversion photons with a partner in the signal channel are detected. The photons in the heralding channel are filtered spectrally with an interference filter with a full width half maximum of 1 nm and spatially by coupling into a single-mode fiber for 810 nm (HP780)¹⁰ with an AR coating for 850 nm. The inefficiency of the heralding channel decreases the heralding rate but not the overall efficiency of the heralding of photons in the signal channel. The photons of the signal channel are coupled in a telecom single-mode fiber (SMF28) with AR coating for 850 nm, the same fiber that is used in the TES packaging. The fibers in which photons are coupled are spliced to the SMF28 fibers which lead to the dilution refrigerator [171], the cooling system which keeps the TESs at a temperature of 25 mK [148, 172]. These fibers are again spliced to the SMF28 fibers used in the TES packaging. The total length of both fibers is around 10 m. The photons coupled into the fiber impinge on the TES and produce an analog signal (see also Secs. 4.4.2 and 4.4.3). Since the detector of the signal channel had a small output signal, the signal was additionally amplified and filtered to get a better signal-to-noise ratio¹¹. The output signals of both channels can then be analyzed. For the heralding two methods of counting were used: a real time analysis by analog electronics and post-processing digitized data.

¹⁰ 780-HP from Nufern

¹¹ SR650 from Stanford Research Systems

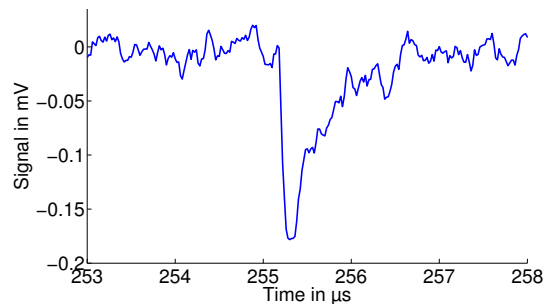


Fig. 6.3: Typical pulse of a single photon at 810nm plotted from digitized data.

For the first method (method 1), the resulting signals are discriminated using a leading edge discriminator¹² and converted by a logic¹³ to transistor-transistor logic (TTL) pulses, which can be counted. Since the pulses have a shape as shown in Fig. 6.3 the signal of a single photon can cross the threshold set at the discriminator more than once due to its wiggles. That would retrigger a count even though only one photon was detected. To prevent this multiple counting of the same photon the negative analog signals from the discriminator were transformed to TTL pulses with a pulse length that depends on the recovery time of the detectors. This pulse length has the same consequences as a dead time. During that time no new photon will be counted. For high count rates this can also mean that photons which were detected are not counted when they fall in the pulse duration. As mentioned in Sec. 4.4.5, a related mechanism reduces the counted number of detected photons at high count rates: The analog pulses pile up and do not cross the threshold. The coincidences are generated in the same logic module using the coincidence (AND) function. It produces a coincidence when the pulses of both detectors overlap for at least 3 ns. The coincidence window is then defined by the sum of the pulse width of the two pulses after the pulse stretching, around 0.95 μ s and 0.05 μ s, corrected by the 3 ns. The coincidences are output as positive TTLs which are counted together with the single counts of both detectors with a module based on field programmable gate array (FPGA). The scheme of the electronics is shown in Fig. 6.4.

The second method (method 2) is to digitize the analog signal with a PCI card¹⁴ and to post-process with further developing counting programs. The subtraction method outlined in Sec. 4.4.5 was used for analysis.

¹² 4608C from LeCroy

¹³ CO4020 from Ortec

¹⁴ ATS460 from AlazarTech

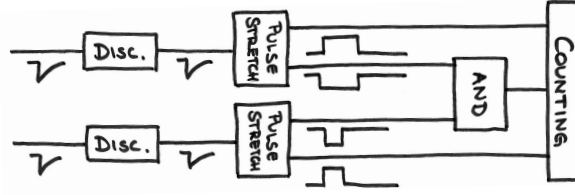


Fig. 6.4: Scheme of counting electronics using nuclear instrumentation modules (NIM). Disc. – leading edge discriminator, Pulse stretch – logic module setting a pulse length for a positive and a negative TTL pulse, AND – coincidence function of the logic module, Counting – FPGA based counting module for positive TTL pulses.

Tab. 6.1: Count rates measured by analog electronics analysis (method 1) of 100s and by post-processing digitized data (method 2) of 40s. Uncertainties are given as Poissonian errors. S_h – single count rate of the heralding channel, S_s – single count rate of the signal channel, C – coincidence rate.

	S_h in Hz	S_s in Hz	C in Hz
method 1	46855 ± 22	6525 ± 8	5419 ± 7
method 2	49882 ± 35	7696 ± 14	6278 ± 13

6.2 Results

The measurement was taken for 100s in real-time using the analog electronics. The count rates shown in Tab. 6.1 result in a directly observed efficiency of the heralding channel of $83.0\% \pm 0.2\%$. It is calculated as the ratio of the measured number of coincidences and the number of singles of the heralding channel. This is the highest value reported for heralding efficiency. The previous record value of 62% was also achieved with a Sagnac source and TESs [173].

The directly observed heralding efficiency has to be corrected for accidental coincidences, which enhances the efficiency and effects due to the pulse length with consequences similar to a dead-time of a detector. Further details are presented in the appendix of the prepared publication in Sec. A.0.1. The corrected value of the heralding efficiency for the numbers measured in real-time are $82.2\% \pm 0.3\%$. This is confirmed by the analysis of 40s of digitized data using the subtraction method with a value of the heralding efficiency of $81.6\% \pm 0.2\%$. The count rates are shown in Tab. 6.1. In the post-processing a shorter coincidence window of 650ns is used and an accidental correction similar to the method described in Sec. A.0.1 is included.

The estimated losses on the way from the pair production in the crystal to the detector is estimated with 6.2%, the detector efficiency is given as $95\% \pm 2\%$ [24]. In consequence that means that the coupling efficiency of the signal channel is $92\% \pm 2\%$. This agrees with the measured coupling loss of $89\% \pm 1\%$, where the heralding efficiency into a SFM28 fiber was compared to coupling into a multimode fiber with a core diameter of $50\mu\text{m}$. If argued the other way around, namely correcting the measured heralding efficiency by the estimated losses from production to detection and by the estimated coupling efficiency from the measurement of SMF28 and multimode fiber, we can estimate the detection efficiency of the TES detectors as $98.3\% \pm 1.3\%$.

Additionally, a measurement of the CHSH-inequality with a maximally entangled state was performed with a value of $S = 2.509 \pm 0.008$ with a directly observed heralding efficiency of $79.7\% \pm 0.2\%$ and a corrected heralding efficiency of $78.6\% \pm 0.1\%$. In a Sagnac source entangled photon pairs are produced by bidirectional pumping of the Sagnac loop. The heralding efficiency is reduced by a non-ideal overlap of both pump directions. The clear violation of the Bell inequality with comparably high heralding efficiency confirms the single-photon nature of the heralded photons.

Eberhard inequality with transition-edge sensors

The next step after the characterization of nonmaximally entangled states produced in the Sagnac source with conventional APD detectors is the measurement of nonmaximally entangled states with the highly-efficient detection system based on transition-edge sensors. As soon as the Eberhard inequality is violated, local realistic theories that exploit low detection efficiency are refuted. An even further step towards the first loophole-free Bell experiment is the space-like separation of Alice and Bob together with their choices of the measurement setting.

In this chapter, the detection system installed in an adiabatic demagnetization refrigerator is used for a measurement of the Eberhard inequality using nonmaximally entangled states.

7.1 Detection system

The application of a detection system based on transition-edge sensors (TESs) constitutes a much more complicated task than the operation of conventional APDs for example. Some specifics for an installation in an adiabatic demagnetization refrigerator (ADR) are presented in the following.

In the ADR sketched in Fig. 4.9 the TESs are mounted to the “cold finger” of the FAA-stage. Since the next shield has a temperature of ~ 3 K, the blackbody photons impinge on the TES and are detected at such a high rate that the TES is saturated and becomes blind to additional single photons. To prevent that, an additional shield mounted at the temperature of the FAA is required. When a superconducting material such as aluminium (Al with a critical temperature of $T_c = 1.2$ K) is used, the TES and SQUID detector unit is additionally magnetically shielded. Without magnetical shielding, stray fields from magnetizable metal tools and movables effect the output signal during operation. Independent of these stray fields, the field of the magnet

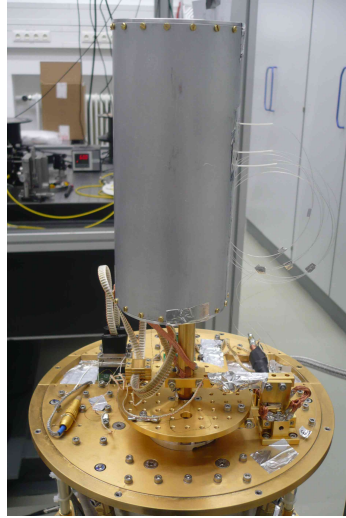


Fig. 7.1: TESs within the Al-shield installed in the ADR. The Al-shield mounted at the FAA's temperature below 100mK shields the TESs from blackbody photons emitted from the 4K-shield. Since Al is a superconducting material, it also serves as a magnetic shield at low temperatures.

of the ADR as well as the Earth's magnetic field ($25\ \mu\text{T}$ to $65\ \mu\text{T}$) can manifest a trapped flux in the SQUID array, which dephases the individual SQUIDS. Due to its planar structure, the SQUID chip is most notably sensitive to fields orthogonal to its surface. Since the performance of the SQUID array is compromised when not all of its SQUIDS are in phase, the device needs to be defluxed by heating it beyond the transition temperature of the SQUID material niobium (Nb with $T_c = 9.2\ \text{K}$) for a time varying from 0.1 ms to a few milliseconds without the presence of a magnetic field. The critical temperature of the Al-shield is passed during the demagnetization of the magnet of the ADR, such that the remaining field of the ADR's magnet and the magnetic fields of the environment are trapped within the shield. To compensate the normal components of this trapped field, a superconducting coil is mounted near the detectors. Both the heater and the current in the compensation coil can be addressed with the software of the room temperature electronics¹⁵. The installed Al-shield is shown in Fig. 7.1. Despite a design less sensitive to magnetic fields of the SQUIDS used as amplifiers, a careful magnetic shielding in the design of the ADR by the manufacturer enables the operation of TESs in an ADR in the first place.

The size of the TES chip of $25\ \mu\text{m} \times 25\ \mu\text{m}$ limits the size of the mode field that can be absorbed and thereby detected by the TES chip with near-unity probability.

¹⁵ SQUIDViewer from Magnicon

The precision of the alignment of the fiber core in respect to the TES chip sets an additional limit. Therefore, the TES chips are packaged with a telecom single-mode fiber¹⁶ with a core diameter of $8.2\ \mu\text{m}$ [135]. The mode field diameter for $1550\ \text{nm}$ is $10.4\ \mu\text{m}$ and smaller for shorter wavelengths. For detection of single photons, they first need to be coupled into a fiber. The photon pairs at $810\ \text{nm}$ produced in the Sagnac source are either coupled into a single-mode fiber¹⁷ or a telecom single-mode fiber. This fiber is then spliced to a bare telecom fiber leading into the ADR via a feedthrough, where the bare fiber is threaded through a $300\ \mu\text{m}$ -hole drilled in a teflon piece which is then compressed by a Swagelok fitting to be vacuum tight [171]. This piece of fiber is installed in the fridge from the room-temperature stage to the 4K-stage where it is spliced to the fiber of the TES packaging. The use of core diameters larger than $8.2\ \mu\text{m}$ would be advantageous for coupling purposes, but would require a bigger TES area. This in turn would slow down the temporal performance.

The voltage across the SQUID array can be read out by the room temperature electronics¹⁸ either in amplifier (Amp) mode or in flux-locked loop (FLL) mode. In contrast to the Amp mode, in FLL mode the system transfer function is linearized, which allows an increased dynamical range [174]. The feedback loop from room temperature to the 4K-stage required for the FLL mode limits the bandwidth of the detection system by the length of the cables. The room temperature electronics are delivered with a control software¹⁹, which allows the control of the whole detection system installed within low temperatures including the working points of the SQUIDS and TESs, the heater, and the compensation coil [175]. In case an additional amplifier is needed for further analysis, a low noise preamplifier²⁰ should be used.

The output signal can be analyzed in realtime using analog electronics (as described in Chap. 6) or by analyzing digitized data either in realtime or in post-processing. The analysis of digitized data allows more control over the parameters used in the analysis. Post-processing on recorded data has the additional advantage that the data can be (re-)analyzed with an improved algorithm. For adjustment purposes, preferably, a realtime program is run on permanently digitized data. For important experimental data, the signal of the detection system is digitized, written to a hard drive and later post-processed with a program shortly sketched as subtraction

¹⁶ SMF-28e from Corning

¹⁷ 780-HP from Nufem

¹⁸ XXF-1 from Magnicon

¹⁹ SQUIDViewer from Magnicon

²⁰ SR560 or SIM910 from Stanford Research Systems

Tab. 7.1: For each setting, data was recorded for 10min using a digitizer card with a sampling rate of 50MS/s and analyzed in the post-processing. Due to a timing jitter of 65ns, the coincidence window is 11 samples or 220ns. The resulting value for the Eberhard inequality is $J = 684.0 \pm 2.6$. The inequality is not violated by the presented measurement.

angles	S1 in Hz	S2 in Hz	CC in Hz
$\alpha_1\beta_1$	1056.5 ± 1.3	1353.0 ± 1.5	601.6 ± 1.0
$\alpha_1\beta_2$	1051.0 ± 1.3	6438.0 ± 3.3	612.0 ± 1.0
$\alpha_2\beta_1$	4834.0 ± 2.8	1355.9 ± 1.5	541.7 ± 0.9
$\alpha_2\beta_2$	4825.0 ± 2.8	6421.2 ± 3.2	32.5 ± 0.2

method in Sec. 4.4.5. The digitizer card²¹ is used with a sampling rate of 20MS/s for realtime applications and 50MS/s for the post-processing.

7.2 Experimental setup

Nonmaximally entangled states are prepared in the Sagnac source and measured with the described detection system based on TESs. The photon pairs are filtered using a longpass filter for rejection of the pump photons together with bandpass filters with a full width at half maximum of 3 nm. For the polarization analysis a half-wave plate (HWP) and a beam displacer (BD) were utilized. Polarization-entangled photon pairs at the ordinary outputs of the BDs are coupled into telecom single-mode fibers spliced to the telecom single-mode fibers of the ADR. The data was digitized for 10min per setting with a sampling rate of 50MS/s and then post-processed using the subtraction method described in Sec. 4.4.5.

7.3 Results

The resulting count rates are listed in Tab. 7.1 with a coincidence window of 220ns. With the fair sampling assumption, where only coincidences are taken into account as done in Sec. 5.2.2, the data is violating the Eberhard inequality with $J_{det} = -1722.8 \pm 1.7$. Without the fair sampling assumption, the value J of the Eberhard inequality calculated from the listed values according to Eq. (3.6) is $J = 684.0 \pm 2.6$. This value does not violate the inequality and the measured correlations agree with

²¹ UF2e-4032 from Strategic Test

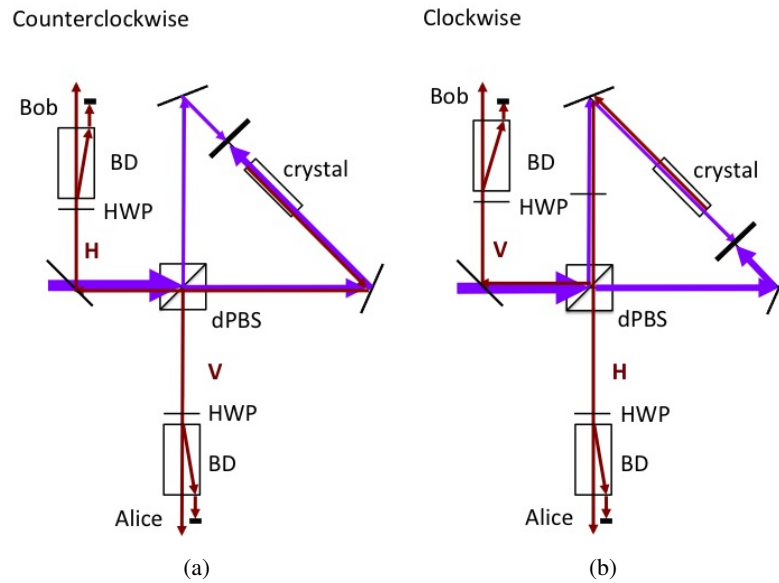


Fig. 7.2: Measurement of the fluorescence photons to be subtracted from total counts. Half-wave plate (HWP), beam displacer (BD), dual-wavelength polarizing beam splitter (dPBS), pump beam (purple), beam of single photons (red). The beam path is blocked after the crystal in counterclockwise direction (a) or clockwise (b). Photons emitted backwards to the respective pump direction are registered. Since the dPBS is polarizing the emitted photons, they arrive vertically polarized at Alice and horizontally polarized at Bob (a), or horizontally polarized at Alice and vertically polarized at Bob (b).

local realism. The possible reasons are twofold: (1) The overall detection efficiency was not high enough, which is mainly attributed to coupling losses; (2) An increased background rate was measured compared to the background rate measured with the laser switched off. The coupling can be further improved by more careful alignment or by application of better components, such as polished aspheric lenses instead of molded aspheres or a new custom-made dPBS. To quantify the background counts, the pump beam was blocked within the Sagnac loop. In this setup (shown in Fig. 7.2), no additional photons should be registered at Alice and Bob. When the beam path is blocked in counterclockwise direction after the crystal, the photon pairs produced in counterclockwise direction in the process of SPDC are blocked as well as the pump beam in clockwise direction. Yet, photons are registered in this configuration and are listed in Tab. 7.2. They originate from the crystal and are emitted in backward direction to the pump beam. Since no coincidences were detected, the process of SPDC from a reflected pump beam can be excluded as the origin of these photons. The

Tab. 7.2: Measured count rates with a blocked beam path within the Sagnac source. Either the beam path was blocked in counterclockwise direction after the crystal (as shown in Fig. 7.2(a)) or in clockwise direction after the crystal (as shown in Fig. 7.2(b)). The subscript VH or HV represent the angles of polarization analysis at Alice and Bob.

	S1 in Hz	S2 in Hz	CC in Hz
counterclockwise _{VH}	175.6 ± 0.5	186.7 ± 0.5	0 ± 0
counterclockwise _{HV}	7.0 ± 0.3	27.9 ± 0.6	0 ± 0
clockwise _{VH}	10.0 ± 0.4	25.4 ± 0.6	0 ± 0
clockwise _{HV}	12.6 ± 0.1	25.2 ± 0.2	0 ± 0
laser _{blocked}	8.3 ± 0.4	14.8 ± 0.4	0 ± 0

background photons emitted from the crystal are polarized at the dPBS. In the setup of Fig. 7.2(a), photons transmitted by the dPBS are horizontally polarized, photons reflected by the dPBS are vertically polarized. When the analyzers are set to vertical polarization at Alice and to horizontal polarization at Bob (VH), all photons after the dPBS should be transmitted; when set to horizontal polarization at Alice and vertical polarization at Bob (HV), no photons should be measured. The analog applies when the beam path is blocked in clockwise direction after the crystal. As can be seen in Tab. 7.2, the number of counts in the configurations of the polarizers where no photons should be measured is higher than in the case of a blocked pump laser. This increased number of counts could be due to photons scattered at the beam block or photons due to the non-perfect extinction ratio of the dPBS. As expected from the unequal laser power in the two pump directions, more background photons are measured from the counterclockwise direction than from the clockwise direction. A measurement of the spectrum of the background photons emitted in backward pump direction is shown in Fig. 7.3 for three different operating temperatures of the ppKTP crystal. The same spectrum was measured in forward direction as well. The spectrum is broadband from 750 nm to 900 nm and the number of background counts decreases with increasing operating temperature of the crystal. Accounted for the observed behavior, the process in which the background photons are produced is expected to be fluorescence in defect centers of the crystal induced by the 405 nm pump laser. To understand how the background counts contribute in the normal (unblocked) setup, the effect of the dPBS on photons from both the backward and forward pump direction has to be considered. When the crystal is pumped in counterclockwise direction, vertically polarized background photons are expected from the backward direction at Alice's output, and horizontally polarized photons from the forward direction. As-

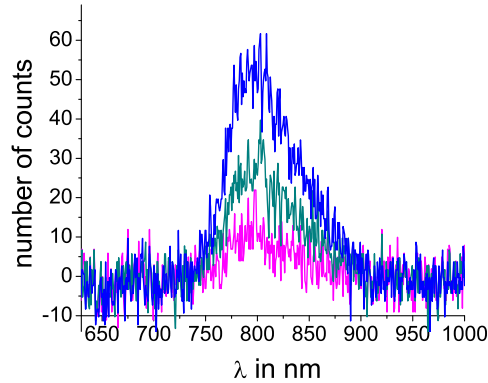


Fig. 7.3: Spectrum of the fluorescence background photon. The number of counts varies with temperature of the ppKTP crystal: 70°C (blue), 40°C (green), 20°C (magenta). Data taken by Bernhard Wittmann.

suming that the same number of background photon is emitted in both directions, the number of measured background photons in the measurement setup without any blocking of the beam path is expected to be independent of the measurement angle at the polarization analysis. The analog applies to Bob and to the background photons induced by the clockwise pump beam. The number of background counts at any angle of the analyzer in the unblocked setup is the same as the sum of the measured background counts of both pump directions, counterclockwise v_H and clockwise H_V , in Tab. 7.2.

For the measurement of a Bell inequality, entangled photon pairs constitute the system of experimental interest. The background photons which are uncorrelated and have a different spectrum than the SPDC photons are not part of that system. Therefore, only the detection efficiency of the entangled photon pairs is significant for the detection loophole. The Eberhard inequality can be corrected for these background counts by subtraction from the single count rates of the measured data. This leads to an Eberhard parameter of $J = 283.9 \pm 2.8$, which is yet in agreement with local realism.

For a violation several experimental parameters can be improved. An increased pair production rate for example can compensate a high dark and background count rate, but also cause accidental counts. These in turn set an upper limit on the pair production rate as a function of the coincidence window. The increased pair production rate does not help in the case of the measured uncorrelated background counts produced in the crystal, because their number was measured to scale linearly with the pump power in the same way as the pair production rate. A reduction of the back-

ground photons can be achieved with a pulsed laser or by application of a crystal with a smaller periodic poling for an increased operating temperature of the crystal for degenerate SPDC at 810 nm. Improvements of the coupling are also possible as demonstrated by the achieved heralding efficiency. An overall detection efficiency equal to the demonstrated heralding efficiency of Chap. 6 for both Alice and Bob would allow a violation of the Eberhard inequality despite the high number of background counts. Further investigations of the background photons and further improvements of the source could not be performed in the framework of this thesis and are left for the future.

Outlook

The long term goal of the work on nonmaximally entangled states is the completion of a conclusive Bell experiment, without the need for additional assumptions. This demands a high purity source of entangled photon pairs which need to be fiber-coupled highly efficiently for the detection by the TES detectors. The overall detection efficiency needs to surpass the limit of $2/3$ for nonmaximally entangled states in the limit of no background. To additionally guarantee the proper space-like separation of the measurement events, the choices of measurement settings and the photon pair emission of the source, fast switching of the measurement settings needs to be implemented with a sufficient distance between Alice, Bob and the source, as well as the respective generation of the setting choices.

8.1 Experimental losses

Based on the heralding experiment described in Chap. 6 it is possible to calculate the expected overall detection efficiency for a measurement of a Bell inequality with nonmaximally entangled states. The measured heralding efficiency was $81.6\% \pm 0.2\%$ which can be corrected for the losses on the components estimated from the specifications of the manufacturers as 4.9% to 6.1% depending on the pump direction. For the Bell experiment more components are used and both channels, Alice and Bob, have to be taken into account. The losses for the two pump directions and the two polarizations of the single photons are not the same, since they pass different paths. Losses on AR-coated surfaces including the components of a local polarization measurement and mirrors are estimated as 2.9% to 3.4% . Optical fibers have an attenuation of around -3.8 dB/km for light at a wavelength of 810 nm . For a fiber length of around 10 m from source to the TES less than 0.9% of photons are lost. The dual wavelength polarizing beam splitter (dpBS) in the Sagnac loop has differ-

ent transmittivity for the two polarizations. In the transmitted output, more photons are lost: for the dPBS utilized in the heralding setup the loss was 1%, and with a new dPBS adjusted for extinction ratio 0.2% are lost. For an ideal setup no pump photons should be detected at Alice and Bob, but since the components are nonperfect it is necessary to use a long pass filter cutting off short wavelength including the pump wavelength of 405 nm. These filters have a loss of 2% for single photons at 810 nm. When additionally band pass filters are used 2% more are lost. All the losses cause only 92.0% of produced photons to be transmitted so they can impinge on the detector. When the measured heralding value is corrected for the estimated losses of the heralding measurement and for the expected losses for a local measurement of a Bell inequality, the overall detection efficiency that can be expected to be achieved, is 78.9% to 80.0%.

8.2 Space-like separation

Similarly to the way the required space-like separations was assured in Refs. [17, 18, 176], the measurement settings must be chosen randomly and the polarization measurement must be switched. Based on the figures of Wittmann et al. [176], who demonstrated EPR-steering loophole-free for the first time, the setting can be produced in 90 ns by the quantum random number generator (QRNG) and the polarization measurement can be switched using fast Pockels cells in 80 ns including the signal conversion [176, 177]. The photon impinging on the TES is absorbed and heats up the superconducting material, producing a measurable increase of resistance. To overcome the distance from the Sagnac source to Alice and Bob, one possible setup is to free-space couple the single photons into the fiber of the TES detection system after the passage of the required distance and the Pockels cells. A different scenario is the coupling of the single photons directly at the source into fibers leading to the detectors. For the polarization analysis either in-fiber components are used or the photons need to be coupled out of fiber to pass the Pockels cell and PBS in free space and then be coupled into the fiber of the TES detection system. These different possible setups each have their own challenges and lead to a significant additional loss from pair emission to single photon detection of 5% to 10%.

8.3 Conclusion

The main ingredients for a conclusive, loophole-free Bell experiment are a source of pure nonmaximally entangled states for the use of the Eberhard inequality for its low

detection efficiency of $2/3$, a highly-efficient detection system, space-like separation of Alice and Bob and a random choice of the measurement setting for Alice space-like separated from Bob and for Bob space-like separated from Alice. If the detection system requires fiber coupling, also a highly-efficient coupling of single-photon pairs has to be achieved. Thanks to the novel technology of the transition-edge sensors, all the necessary components are available nowadays. At the beginning of this work the expertise of space-like separation and the Sagnac source were at hand [18, 28]. For the first time a Sagnac source was used to prepare nonmaximally entangled states within the scope of this work. These states were first characterized with commercial avalanche photodiodes and were theoretically shown to be able to violate the Eberhard inequality. As a step towards the violation of the Eberhard inequality, a heralding efficiency of 82% was achieved using the Sagnac source and transition-edge sensors. This value is unprecedentedly high. The first measurements of the Eberhard inequality using the transition-edge sensors were also performed after their installation in an adiabatic demagnetization refrigerator. At the time the work was finished, the setup was not sufficiently efficient and not well enough aligned yet to violate the Eberhard inequality locally. It has to be improved further to reach for both Alice and Bob a comparable overall detection efficiency to the heralding efficiency achieved in heralding experiment. The next step is the space-like separation of the respective components. A loophole-free Bell experiment demands two separate cooling systems equipped with efficient detectors, but in derogation from Eberhard's original formulation of his inequality only one efficient detector is necessary on each side of the experiment Alice and Bob. This agrees with the usual formulation of the equivalent CH inequality. The additional space-like separation of 50m to 100m remains a challenge due to the additional losses for a space-like separated measurement compared to a local measurement. However, based on the demonstrated heralding efficiency an overall detection efficiency of 71% to 76% can be expected to be attained in a space-like separated setup. According to the calculation of the state optimization, this allows a violation of the Bell inequality in the presence of at most 0.35% dark and background counts, assuming a visibility of $V = 98.5\%$ and a coincidence window of 160ns is achieved. A higher value for the visibility will increase the level of the allowed noise.

A

Appendix

A.0.1 Prepared publication about heralding efficiency

A publication is prepared on the highly efficient heralding of single photons using the Sagnac source described in Sec. 6.

Highly Efficient Heralding of Entangled Single Photons

Sven Ramelow*,^{1,2} Alexandra Mech*,^{1,2} Marissa Giustina*,^{1,2} Simon Groeblacher,² Witłef Wieczorek,² Adriana Lita,³ Brice Calkins,³ Thomas Geritts,³ Sae Woo Nam³, Anton Zeilinger^{1,2} and Rupert Ursin¹

¹*Institute for Quantum Optics and Quantum Information, Austrian Academy of Sciences, Boltzmannngasse 3, Vienna, Austria*

²*University of Vienna, Faculty of Physics, Boltzmannngasse 5, Vienna, Austria*

³*NIST, Boulder, USA*

* *These authors contributed equally to this work*

sven.ramelow@univie.ac.at, marissa.giustina@univie.ac.at

Abstract: Single photons are an important prerequisite for a broad spectrum of quantum optical applications. We experimentally demonstrate a heralded single-photon source based on spontaneous parametric down-conversion in collinear bulk optics, and fiber-coupled bolometric transition-edge sensors. Without correcting for background, losses or detection inefficiencies we measure an overall heralding efficiency of 83%. By violating a Bell inequality, we confirm the single-photon character and high-quality entanglement of our heralded single photons which, in combination with the high heralding efficiency, are a necessary ingredient for advanced quantum communication protocols like one-sided device-independent quantum key distribution.

© 2012 Optical Society of America

OCIS codes: (270.5585) Quantum information and processing; (040.5570) Quantum Detectors; (040.3780) Low light level;

References and links

1. J. G. Rarity, K. D. Ridley, and P. R. Tapster. Absolute measurement of detector quantum efficiency using parametric downconversion. *Applied Optics*, 26(21):4616–4619, November 1987.
2. P. G. Kwiat, A. M. Steinberg, R. Y. Chiao, P. H. Eberhard, and M. D. Petroff. Absolute efficiency and time-response measurement of single-photon detectors. *Applied Optics*, 33(10):1844–1853, April 1994.
3. A. L. Migdall, R. U. Datla, A. Sergienko, J. S. Orszak, and Y. H. Shih. Absolute detector quantum-efficiency measurements using correlated photons. *Metrologia*, 32(6):479–483, December 1995.
4. Nicolas Gisin, Gregoire Ribordy, Wolfgang Tittel, and Hugo Zbinden. Quantum cryptography. *Reviews of Modern Physics*, 74(1):145, March 2002.
5. Valerio Scarani, Helle Bechmann-Pasquinucci, Nicolas J. Cerf, Miloslav Duscarnonek, Norbert Lütkenhaus, and Momtchil Peev. The security of practical quantum key distribution. *Reviews of Modern Physics*, 81(3):1301, 2009.
6. Pieter Kok, W. J. Munro, Kae Nemoto, T. C. Ralph, Jonathan P. Dowling, and G. J. Milburn. Linear optical quantum computing with photonic qubits. *Reviews of Modern Physics*, 79(1):135, January 2007.
7. T. D. Ladd, F. Jelezko, R. Laflamme, Y. Nakamura, C. Monroe, and J. L. O'Brien. Quantum computers. *Nature*, 464(7285):45–53, March 2010.
8. T. B. Pittman, B. C. Jacobs, and J. D. Franson. Single photons on pseudodemand from stored parametric down-conversion. *Physical Review A*, 66(4):042303, October 2002.
9. Evan Jeffrey, Nicholas A. Peters, and Paul G. Kwiat. Towards a periodic deterministic source of arbitrary single-photon states. *New Journal of Physics*, 6:100–100, July 2004.

10. A. L. Migdall, D. Branning, and S. Castelletto. Tailoring single-photon and multiphoton probabilities of a single-photon on-demand source. *Physical Review A*, 66(5):053805, November 2002.
11. Jeffrey H. Shapiro and Franco N. Wong. On-demand single-photon generation using a modular array of parametric downconverters with electro-optic polarization controls. *Optics Letters*, 32(18):2698–2700, 2007.
12. Robert Raussendorf, Daniel E. Browne, and Hans J. Briegel. Measurement-based quantum computation on cluster states. *Phys. Rev. A*, 68:022312, Aug 2003.
13. Cyril Branciard, Eric G. Cavalcanti, Stephen P. Walborn, Valerio Scarani, and Howard M. Wiseman. One-sided device-independent quantum key distribution: Security, feasibility, and the connection with steering. *Physical Review A*, 85(1):010301, 2012.
14. Devin H. Smith, Geoff Gillett, Marcelo P. de Almeida, Cyril Branciard, Alessandro Fedrizzi, Till J. Weinhold, Adriana Lita, Brice Calkins, Thomas Gerrits, Howard M. Wiseman, Sae Woo Nam, and Andrew G. White. Conclusive quantum steering with superconducting transition-edge sensors. *Nature Communications*, 3:625, January 2012.
15. Yong-gang Tang and Qiang Liu. Private communication.
16. F. Selleri and A. Zeilinger. Local deterministic description of Einstein-Podolsky-Rosen experiments. *Foundations of Physics*, 18, 1988.
17. Paul G. Kwiat, Klaus Mattle, Harald Weinfurter, Anton Zeilinger, Alexander V. Sergienko, and Yanhua Shih. New High-Intensity source of Polarization-Entangled photon pairs. *Physical Review Letters*, 75(24):4337, December 1995.
18. Taehyun Kim, Marco Fiorentino, and Franco N. C. Wong. Phase-stable source of polarization-entangled photons using a polarization Sagnac interferometer. *Physical Review A*, 73(1):012316, January 2006.
19. Alessandro Fedrizzi, Thomas Herbst, Andreas Poppe, Thomas Jennewein, and Anton Zeilinger. A wavelength-tunable fiber-coupled source of narrowband entangled photons. *Optics Express*, 15(23):15377–15386, 2007.
20. P. Trojek and H. Weinfurter. Collinear source of polarization-entangled photon pairs at nondegenerate wavelengths. *Applied Physics Letters*, 92(21):211103–211103–3, May 2008.
21. Christoph Söller, Offir Cohen, Brian J. Smith, Ian A. Walmsley, and Christine Silberhorn. High-performance single-photon generation with commercial-grade optical fiber. *Physical Review A*, 83(3):031806, March 2011.
22. Bernhard Wittmann, Sven Ramelow, Fabian Steinlechner, Nathan K. Langford, Nicolas Brunner, Howard M. Wiseman, Rupert Ursin, and Anton Zeilinger. Loophole-free Einstein-Podolsky-Rosen experiment via quantum steering. *New Journal of Physics*, 14(5):053030, May 2012.
23. Adriana E. Lita, Aaron J. Miller, and Sae Woo Nam. Counting near-infrared single-photons with 95% efficiency. *Optics Express*, 16(5):3032–3040, March 2008.
24. Ryan S. Bennink. Optimal collinear gaussian beams for spontaneous parametric down-conversion. *Physical Review A*, 81(5):053805, 2010.
25. Aaron J. Miller, Adriana E. Lita, Brice Calkins, Igor Vayshenker, Steven M. Gruber, and Sae Woo Nam. Compact cryogenic self-aligning fiber-to-detector coupling with losses below one percent. *Opt. Express*, 19(10):9102–9110, May 2011.
26. D. Drung, C. Assmann, J. Beyer, A. Kirste, M. Peters, F. Ruede, and T. Schurig. Highly sensitive and easy-to-use SQUID sensors. *IEEE Transactions on Applied Superconductivity*, 17:699–704, 2007.
27. Danna Rosenberg, Adriana E. Lita, Aaron J. Miller, and Sae Woo Nam. Noise-free high-efficiency photon-number-resolving detectors. *Physical Review A*, 71(6):061803, June 2005.
28. M. Giustina et. al. in preparation.
29. John F. Clauser, Michael A. Horne, Abner Shimony, and Richard A. Holt. Proposed experiment to test local hidden-variable theories. *Phys. Rev. Lett.*, 23:880–884, Oct 1969.

1. Introduction

The controlled and deterministic generation of single-photon states and correlated pairs remains a challenge particularly crucial to a wide variety of emerging optical quantum technologies including metrology [1, 2, 3], quantum communication [4, 5] and optical quantum computing [6, 7], to name just a few. Although they are not inherently deterministic, highly efficient heralded single-photon sources are relevant to this problem. By combining such a heralded source with a photon memory that can store and release photons in a controlled way [8, 9] or by multiplexing several heralded sources and using feed-forward and fast switching to select a channel that contains a single photon [10, 11], it is possible to construct an on-demand single- (and by extension, multi-) photon source. Such a source could be an important ingredient for post-selection-free multi-photon one-way quantum computation [12]. Even without these extensions, a highly-efficient heralded photon source would be valuable. For example, the intrinsically secure one-sided device-independent quantum key distribution protocol requires sources

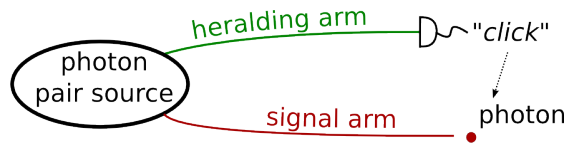


Fig. 1. Heralded single-photon source based on correlated photon pairs. Such sources are a prerequisite to a multitude of quantum optical experiments. In an ideal single-photon source, a photon detected in the heralding arm indicates a partner photon in the signal arm.

of entangled photons with heralding efficiencies (including detection) of at least 66% [13], which have not yet been demonstrated [14]. In addition, such high coupling marks an important step toward a loophole-free Bell test as it is relevant not only to the fair-sampling loophole but also to the freedom-of-choice loophole [15, 16]. Furthermore, any source which heralds the arrival of a known photon number and energy is also useful for coincidence-based detector calibration [1, 2, 3], which promises to overcome the precision limitations of power and attenuation measurements that presently dominate the calibration process for single-photon detectors.

An ideal heralded photon source should provide a heralding signal which indicates the presence of exactly one photon, preferably in a fiber. Over the past decades, spontaneous parametric down-conversion (SPDC) has proven to be a robust, well-understood, and reliable method for generating time-correlated photon pairs which may be split into two spatial modes. SPDC is a promising candidate for high-quality heralded single-photon sources where the detection of a photon in one mode (the heralding or idler mode) indicates a photon in the other (signal mode). Moreover, producing polarization entanglement based on SPDC has been demonstrated with high quality and flexibility, which suggests that such heralding sources are readily extendible to the quantum applications listed above [17, 18, 19]. Although fiber coupling demands additional precision in the construction of the source, it substantially improves the versatility of the source; furthermore the mode selection achieved by the fiber can enhance the heralding efficiency.

In practice, no source is truly ideal and any source may be subject to a “missing photon error,” such that a heralding signal is issued but no photon is present in the signal mode. This may result from background in the heralding signal or photon loss in the source or signal mode, for instance from imperfect optical elements or fiber coupling. Although a limited detector efficiency does not introduce further loss into the source itself, highly efficient detectors are necessary to confirm the quality of the source heralding.

Due to missing photon errors and the low efficiency of the industry standard silicon avalanche photodiodes (APDs), the highest reported heralding values have until recently been in the range between 30% and 50% [20, 21, 22]. However, the recent advent of superconducting bolometric detectors suggests the impending reality of near-unity heralding efficiency, and, utilizing this technology, total heralding efficiencies of up to 62% have already been observed [14]. Here, we combine the nearly-perfect detection efficiency offered by transition-edge sensors (TES) [23] with the ultra-high coupling efficiency of our fiber-coupled photon pair source based on SPDC in a bulk crystal; we achieve a source in which up to 83% heralding efficiency has been observed. In addition, when using polarization-entangled photon pairs we record the only slightly reduced heralding value of 80%. (Note that the efficiencies reported here have been measured *directly*, without correction for dark counts, accidental counts, inefficient detection, or known optical losses.) To our knowledge, these values are the highest directly-observed heralding efficiencies. We analyze the origin of the remaining losses in our system; this analysis confirms the nearly-perfect efficiency of the TES detectors and indicates that it may be feasible to observe heralding values close to 100% with the presented technology based on bulk-crystal down-conversion and TES detectors.

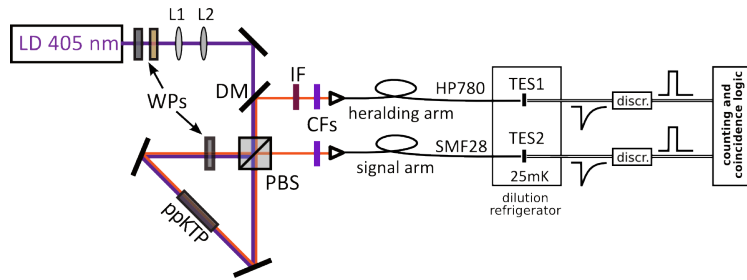


Fig. 2. Experimental setup: The photon pair source is based on a 10 mm long ppKTP crystal pumped by a 405 nm diode laser in a Sagnac configuration [19] with a polarizing beam splitter (PBS). Waveplates (WPs) are used to tune the pump polarization. The pump beam is carefully shaped and focussed by two lenses (L1, L2) and split from the down-converted photon with a dichroic mirror (DM). Cut-off filters (CFs) are used to filter out the remaining 405 nm light and a narrowband interference filter (IF) in the heralding arm further suppresses any photons not originating from the down-conversion. The photon pairs are coupled into optical fibers (HP780, SMF28) that carry them into the dilution refrigerator where they are directly coupled to the TES detectors with their SQUID amplifiers (TES1, TES2) which are held at around 25 mK. The TES output signals are discriminated using threshold discrimination and are counted and analyzed by our coincidence electronics.

2. Experiment

Our source of (entangled) photon pairs (see Fig.2) is based on SPDC in a periodically poled potassium titanyl phosphate (ppKTP) crystal with a poling period of around $10\mu\text{m}$ for the quasi-phase-matched creation of photon pairs at 810 nm with a 405 nm pump diode laser – the design is described in detail in [18, 19]. The crystal can be pumped bi-directionally in a Sagnac-type configuration to produce polarization entanglement. Pumping the crystal in only one direction creates a polarization product state. The emitted photon pairs are split, with each photon entering one of two (separate) single mode (SM) fibers.

Any photon detected in the heralding arm announces (heralds) the presence of a photon in the signal arm. To reach a high heralding efficiency it is crucial to detect in the heralding arm only photons from the SPDC process, while simultaneously minimizing losses in the signal arm. This is achieved in our setup by a number of steps. Tight spectral filtering of the heralding arm, accomplished with a cut-off filter to block pump photons (Semrock longpass filter with cutoff around 650 nm) and a 1 nm bandpass filter centered at the down-converted wavelength, ensures that only photons directly emitted by the SPDC process (intrinsic bandwidth ≈ 0.5 nm FWHM) are coupled to the heralding arm. The inevitable loss introduced by this spectral filtering does not reduce the heralding efficiency, which depends on the transmission in the signal arm. The signal arm is filtered only with a cut-off filter (as used in the heralding arm) to suppress the pump light, which introduced a loss of around 2% for 810 nm. In addition, we optimize the focusing parameters and spatial shaping of the pump beam and heralding arm to maximize the heralding efficiency [19, 24]. By coupling to a standard single mode fiber (Nufern HP780) in the heralding arm, but to a standard telecom fiber (Corning SMF-28) – which is slightly bimodal at 810 nm – in the signal arm, the heralding efficiency can be further increased. The fiber tips were anti-reflection (AR) coated for 810 nm to minimize reflection losses in the fiber coupling.

Photon detection is accomplished in our experiment with transition-edge sensors (TES), which in recent years have attracted considerable attention as highly efficient single-photon counters. For detecting photons in the visible and near-infrared regime, a 25-micron square

of tungsten thin film, cooled to well within a superconducting state and voltage-biased on its transition edge, serves as both absorber and thermometer in this bolometric-style detector. Any photon absorbed by the tungsten will heat it and manifest an increase in resistance, which in turn yields a proportional current drop through the voltage-biased device on the order of 50 nA. Then the heat dissipates through a weak thermal link to the base temperature, and the detector returns to its original resistance. Although the TES film itself has a thickness of only 20 nm, embedding the TES in a wavelength-specific optical cavity yields detectors with peak efficiencies of at least 95% for the selected wavelength [23]. Note that this value includes losses in coupling from a Corning SMF-28 fiber to the TES chip, which is accomplished by a packaging process detailed in [25].

The TES is operated in series with an input coil which is inductively coupled to a superconducting quantum interference device (SQUID) for readout [26]. The signal spike from an incident photon enters the SQUID as a changing flux and may be read out as a voltage. In the relevant bandwidth of our electrical measurements (up to 1 MHz) the SQUID's input-referred current noise is less than 25% of that of the TES output current, so the TES itself dominates the noise of the system. Photons were distilled from the analog electrical output signal according to the following procedure. Individual photon spikes were identified and converted to TTL pulses using a leading-edge discriminator (LeCroy 4608C). We set the threshold of this discriminator to a value which registered a reasonable count rate of 810 nm photons but also minimized the dark count rate when the source was blocked. Although TES detectors have no intrinsic dark counts and only a real energy signal will create a current pulse, a non-zero background level may be registered by the presence of background light in the experimental setup [27]. Even thermal blackbody radiation or infrared photons may be seen by a TES optimized for use in the visible regime, and if the threshold level is set too close to zero, such a thresholding counting method may lead to increased background counts.

To avoid re-triggering and thereby mistakenly counting a non-existent second photon in the noise of the recovering edge of the first, we implemented a "deadtime" by using TTL pulses sufficiently long so as to "re-arm" the discriminator only after the signal's recovery. Thereafter we counted coincidences using an analog logic module (Ortec CO4020) which registered a coincidence for each overlap of greater than 3 ns between the TTL pulses of the two channels. Thus the effective coincidence window is defined as the sum of the TTL pulse lengths for the two channels, which in our case was $1.05 \mu\text{s}$: $1 \mu\text{s}$ for the heralding arm and $0.05 \mu\text{s}$ for the signal arm. Each coincidence was represented by yet another TTL pulse from the logic module, and all three TTL channels were counted with a standard counter connected to a PC, which allowed us to monitor the heralding efficiency in real time.

As an alternative to analog discriminators and logic modules, we also digitized and recorded data for post-processing using an Alazar ATS460. Post-processing facilitates more complicated counting algorithms and finer control over the coincidence window. These algorithms also enable the recovery of photons lost by the analog counting method. More information on post-processing will be detailed in a subsequent paper [28]; more information on the correction of so-called "accidental coincidences" may be found in the appendix.

3. Results

We tuned the pump power to a level suitable for the detectors and pumped the source in only one direction (creating a polarization product state). With the source in this condition, we measured the singles and coincidences for 100 seconds with our analog electronics and digitized 40 seconds of data for post-processing. The results are summarized in Table 1. The raw ratio between heralding counts and directly observed coincidences is $83.05\% \pm 0.15\%$. This represents an unprecedented value for uncorrected heralding efficiency.

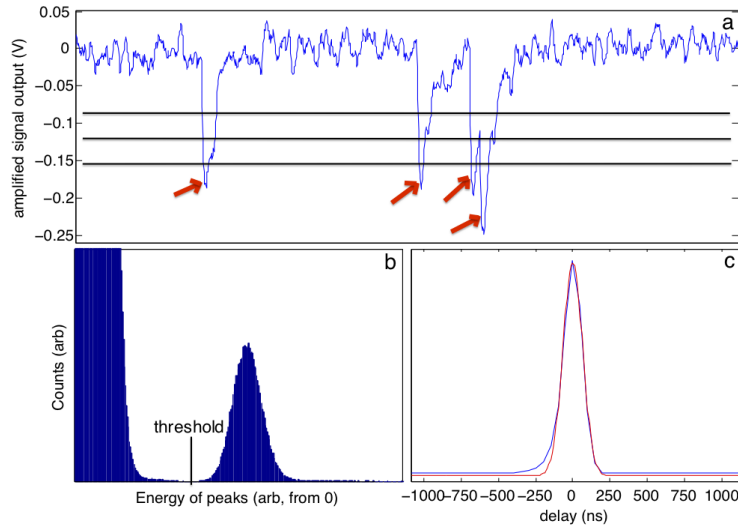


Fig. 3. Photon signals and processed data from transition-edge sensor single-photon detectors. (a) A typical signal from a detector with four photons and different possible thresholds indicated. The top threshold detects only three of the four photons, the middle threshold counts five (one from the wiggle in the recovering edge) and the bottom threshold detects the correct four photons. (b) A “pulse height distribution,” indicating how clearly it is possible to separate the photon signals from the noise by thresholding. (c) Coincidence count rates vs. delay between the two channels. The actual data is plotted in blue with a gaussian fit in red. Asymmetry is attributed to uneven detector jitter.

When determining the heralding efficiency as the ratio of the measured coincidence and single count rates, it is necessary to account for a systematic error known as “accidental coincidences.” An accidental coincidence occurs when two photons which did not originate from the same pair are detected within a coincidence window and are thus counted as a coincidence. If left uncorrected, this effect would lead to an over-estimation of the actual heralding efficiency. Using the formulas explained in the appendix, we find a systematic error for the heralding efficiency of $1.0 \pm 0.1\%$ which leads to a corrected heralding efficiency of $82.0 \pm 0.3\%$. Post-processing, which allows us to choose our coincidence window and includes accidental correction by a method similar to that described in the appendix, yields the heralding value of $81.9\% \pm 0.2\%$ for the same coincidence window of $1.05 \mu\text{s}$, which agrees very well with the directly observed data. We also measured a combined jitter of approximately 155 ns FWHM for the two detectors, which determines an upper limit on the timing precision with which we herald our photons. Note that this could be further improved without affecting the heralding efficiency by replacing the heralding detector with a low-jitter detector.

The system detection efficiency of the TES is expected to be close to unity [23]. In our experiment, the following losses contribute to the reduction of the heralding efficiency from 100%. The estimated total optical losses in the source sum to around 6% [19]. Additionally, there are losses due to fiber coupling; using standard silicon APDs to compare the heralding ratios between large core diameter fibers (multimode, $50 \mu\text{m}$) and the SMF-28 fiber used in the experiment, we concluded that the loss introduced by the fiber coupling is around 10%. Combining these estimations with the measured and accidental-corrected heralding efficiency of 82%, we find that the system efficiency of the TES (including fiber splices, interface between fiber and

	signal arm	heralding arm	coincidences
analog-processed counts	$46855 \pm 22 \text{ s}^{-1}$	$6525 \pm 8 \text{ s}^{-1}$	$5419 \pm 7 \text{ s}^{-1}$
analog arm efficiency	$83.0\% \pm 0.2\%$	$11.57\% \pm 0.02\%$	
acc.-corrected eff.	$82.0\% \pm 0.3\%$	$11.39\% \pm 0.03\%$	
post-processed counts	$49882 \pm 35 \text{ s}^{-1}$	$7696 \pm 14 \text{ s}^{-1}$	$6278 \pm 13 \text{ s}^{-1}$

Table 1. Tabulated experimental results from both the analog electronics counting method and the post-processing. The lower efficiency in the second arm is a consequence of the higher loss caused by the limited transmission efficiency of the narrow bandpass filter as well as a high rate of background photons in the signal arm not rejected by the cut-off filters. The post-processing method can recover counts not registered by the analog method. The one standard deviation errors are determined by Poissonian counting statistics and error propagation.

detector, and quantum efficiency of the absorptive area of the TES) is with high certainty above 95% [23]. This represents the first verification of the transition-edge sensor’s near-unity detection efficiency using a method based on the quantum nature of light and thus differing from the standard approaches based on calibrated power and attenuation measurements.

Entanglement is a necessary ingredient in the system if one wants to prepare heralded single photons in a remotely chosen basis or utilize the high heralding efficiency for one-sided device-independent QKD [14]. To generate entanglement in our source, we pumped it in both directions to produce a nearly maximally-entangled state [19]. In this state, the directly-measured heralding efficiency decreased to $79.70\% \pm 0.16\%$. We believe the reduction is mainly a consequence of imperfect overlap between the two pump directions when the source is pumped bi-directionally. To verify a high degree of entanglement we tested a CHSH inequality [29]. For the necessary polarization measurements we inserted plate polarizers with an additional loss of around 15% and measured the polarization correlations for all necessary setting combinations for the CHSH inequality, integrating for 10 s per setting. This resulted in a Bell parameter of $S = 2.51 \pm 0.01$ which is more than 50 standard deviations above the classical bound of 2 and shows a high fidelity of the entangled state. Note that the presence of entanglement confirms the single-photon nature of our source.

4. Conclusion and Outlook

In conclusion, using TES detectors we demonstrated a heralded single-photon source with an unprecedented high efficiency in bulk optics, achieving a single-photon heralding efficiency of 83% without any correction for background, detection efficiency or other losses. Moreover, it was possible to produce heralded entangled photons, useful for one-sided device-independent QKD, with only minimal decrease in efficiency.

To compensate for the systematic accidental coincidences which would otherwise lead to an overestimation of heralding efficiency, we developed an extended accidental correction model. This takes into account the very high coupling efficiencies, which are typically assumed to be small to justify neglecting several terms in the expression quantifying the expected accidentals.

Moreover, we would like to point out that our source facilitated the use of heralded single photons to infer a system detection efficiency of over 95% for a TES detector. It is important to

note that for a detector-calibration method such as this, which is based on correlated photons, the accuracy of the measurement improves with the heralding ratio.

Finally, we note that while very promising fiber-based realizations of heralded single photon sources have already been demonstrated [21], our results indicate that with further optimization of losses and focusing conditions, it should be possible to reach near-unity heralding efficiencies in a bulk optics configuration.

5. Acknowledgement

The authors would like to acknowledge the help of Jörn Beyer and Marco Schmidt at the Physikalisch-Technische Bundesanstalt in Berlin, Germany for providing SQUID amplifiers and assistance with the TES-SQUID system setup. In addition, we thank Markus Aspelmeyer for the use of his dilution refrigerator.

This work was supported by the Austrian Science Foundation (FWF) under projects SFB F4008 and CoQuS, the grant Q-ESSENCE (no. 248095), and the John Templeton Foundation.

6. Appendix

6.1. Accidental effects

For determining the systematic effects of accidental coincidences a careful analysis is required. Accidental coincidences occur when two photons that are not from the same pair are detected and counted as a real coincidence. Their rate depends on the length of the coincidence window τ_w , the rate of produced pairs R_0 , and the two total arm efficiencies η_1 and η_2 .

Assuming dark counts are negligible, the two singles rates (total rate of detected clicks per detector) for each arm S_1 and S_2 are given by:

$$S_1 = R_0 \eta_1 \quad (1)$$

$$S_2 = R_0 \eta_2 \quad (2)$$

If the detectors have a dead-time τ_d (time interval after a detection event in which the detectors are blind) this will create a saturation effect which, for dead-times much smaller than the inverse detection rates, leads to singles rates given by the following:

$$S_1 = R_0 \eta_1 (1 - S_1 \tau_d) \quad (3)$$

$$S_2 = R_0 \eta_2 (1 - S_2 \tau_d) \quad (4)$$

These can be derived by the following argument: for any detected photon (detected at a rate S) there is a probability of $S\tau_d$ that a second photon appears within τ_d after the detection of the first. Such a photon would be lost because of the blind detector. Therefore, the rate of lost detections is $S^2\tau_d$ or equivalently a correction factor of $(1 - S\tau_d)$ must be used. Note that, in general, there can be different dead-times for the two detectors.

A coincidence is defined as the detection of two photons, one in each arm, separated by a time difference of less than half the given coincidence window, i.e. with a time difference between $-\tau_w/2$ and $+\tau_w/2$ (resulting in a full window of τ_w). With negligible accidental coincidences (e.g. in the limit of very small pair creation probabilities per coincidence window) one would detect the following (unmodified) rate of coincidences CC_0 :

$$CC_0 = R_0 \eta_1 \eta_2 \quad (5)$$

However, as described above, sometimes two (unrelated) pairs are *accidentally* created so close to each other that photons from different pairs may be detected as a coincidence. These are generally called *accidental coincidences*. Note that in most cw photon pair source implementations, the coherence time of the produced photons will be much shorter (order of ps) than the coincidence window. Thus for cw down-conversion, higher order contributions (genuine multi-pair emission) are typically negligible.

There are now two possibilities by which accidental coincidences may occur. First, the first photon of the accidental coincidence is detected in arm 1, while its partner photon in arm 2 is lost – this happens with a rate of $R_0 \eta_1 (1 - \eta_2)$. In order to lead to an accidental coincidence a second pair needs to be created within half the coincidence window after the detection of the first photon, which happens with a probability of $R_0 * \tau_w/2$. To cause a coincidence, the photon in arm 2 must be detected, which happens with efficiency η_2 . Importantly, the rate of coincidences is increased only if this second pair would not have otherwise been detected as a coincidence on its own, meaning that its partner photon in arm 1 must not have been detected. The probability for this is given by $(1 - \eta_1)$. Collecting all the terms, the rate R_{10} by which the detected coincidences are increased for this case is given by:

$$R_{10} = \frac{1}{2} R_0^2 \tau_w \eta_1 (1 - \eta_2) \eta_2 (1 - \eta_1) \quad (6)$$

In the same way one can derive the rate increase R_{01} caused by the second possibility – where the first photon of the accidental coincidence is detected in the arm 2, while its partner is not detected in arm 1, and simultaneously a photon in arm 1 is detected from a second pair that is created within half a coincidence window after the detection of the first photon and would not have been detected as a coincidence on its own:

$$R_{01} = \frac{1}{2}R_0^2\tau_w\eta_2(1-\eta_1)\eta_1(1-\eta_2) \quad (7)$$

R_{10} and R_{01} are actually the same, as one would of course expect since only the time ordering of the respective events is reversed and this does not change their probability. However, dividing the cases into these two distinct possibilities makes the logic of the argument easier to follow.

There is also an effect that reduces the number of detected coincidences. This is a saturation effect that also depends on how exactly the coincidence logic is technically implemented. A commonly used method is to create a pulse or bin with a length of half the coincidence window for each of the detector channels. A coincidence is then counted for each overlap of pulses from the two different channels – i.e. when the two detection events happen with a time-difference between $-\tau_w/2$ and $+\tau_w/2$. When two pairs are created within a time span of $\tau_w/2$ and both photons of the first pair are detected (which happens with a rate of $R_0\eta_1\eta_2$), the second pair (which occurs with probability $R_0\tau_w/2$ and is detected with probability $\eta_1\eta_2$) cannot be detected as a coincidence anymore. This is similar to the dead-time effect for the singles rate. The rate of coincidences is therefore reduced by the number of events that would have been detected without this effect. This reduction of coincidences is given by:

$$R_{11} = -\frac{1}{2}\tau_w R_0^2\eta_1^2\eta_2^2 \quad (8)$$

If the pulse or bin lengths for the two arms are different, the longer of the two (τ_{max}) will be the effective dead-time instead of $\tau_w/2$. Importantly, if the intrinsic dead-time of the detectors is greater than τ_{max} or $\tau_w/2$ then τ_d must be used for R_{11} instead of τ_{max} or $\tau_w/2$.

Taking now all three contributions (R_{10} , R_{01} and R_{11}) into account, the rate of observed coincidences $CC = CC_0 + R_{10} + R_{01} + R_{11}$ is given by:

$$CC = R_0\eta_1\eta_2 + \tau_w R_0^2\eta_1\eta_2(1-\eta_1)(1-\eta_2) - \frac{1}{2}\tau_w R_0^2\eta_1^2\eta_2^2 \quad (9)$$

or more compactly written:

$$CC = CC_0(1 + \tau_w R_0(1-\eta_1)(1-\eta_2) - \frac{1}{2}\tau_w R_0\eta_1\eta_2) \quad (10)$$

and if the pulse lengths differ between the two arms,

$$CC = CC_0(1 + \tau_w R_0(1-\eta_1)(1-\eta_2) - \tau_{max} R_0\eta_1\eta_2). \quad (11)$$

The last equation and the two equations for the singles rates $S1$ and $S2$ form a set of three equations for the three unknown quantities η_1 , η_2 and R_0 . These can be determined by solving this set of equations given the experimental parameters (the τ 's) and measured rates $S1$, $S2$ and R_0 to yield the accidental (and dead-time) corrected values for η_1 and η_2 . The general full solutions for these are rather long formulas, however these can be easily handled by mathematics software.

Using the measured rates of $S1 = 46855.2 \text{ s}^{-1}$, $S2 = 6525.0 \text{ s}^{-1}$, and $CC = 5418.8 \text{ s}^{-1}$ as well as $\tau_w = 1.05 \mu\text{s}$ and $\tau_{max} = 1 \mu\text{s}$ yields for η_1 the accidental corrected value of $82.0\% \pm 0.3\%$.

References

- [1] A. Einstein, B. Podolsky, N. Rosen, Can quantum-mechanical description of physical reality be considered complete?, *Phys. Rev.* **47**, 777 (1935).
- [2] J. S. Bell, On the Einstein-Podolsky-Rosen paradox, *Physics* **1**, 195 (1964), reprinted in J.S. Bell, (1987), *Speakable and Unspeakable in Quantum Mechanics*, Cambridge University Press.
- [3] C. S. Wu, I. Shaknov, The angular correlation of scattered annihilation radiation, *Phys. Rev.* **77**, 136 (1950).
- [4] C. A. Kocher, E. D. Commins, Polarization correlation of photons emitted in an atomic cascade, *Phys. Rev. Lett.* **18**, 575 (1967).
- [5] S. J. Freedman, J. F. Clauser, Experimental test of local hidden-variable theories, *Phys. Rev. Lett.* **28**, 938 (1972).
- [6] J. F. Clauser, Experimental investigation of a polarization correlation anomaly, *Phys. Rev. Lett.* **36**, 1223 (1976).
- [7] E. S. Fry, R. C. Thompson, Experimental test of local hidden-variable theories, *Phys. Rev. Lett.* **37**, 465 (1976).
- [8] L. Kasday, J. Ullman, C. Wu, Angular correlation of Compton-scattered annihilation photons and hidden variables, *Il Nuovo Cimento B (1971-1996)* **25**, 633 (1975).
- [9] A. R. Wilson, J. Lowe, D. K. Butt, Measurement of the relative planes of polarization of annihilation quanta as a function of separation distance, *Journal of Physics G: Nuclear Physics* **2**, 613 (1976).
- [10] M. Bruno, M. D'Agostino, C. Maroni, Measurement of linear polarization of positron annihilation photons, *Il Nuovo Cimento B (1971-1996)* **40**, 143

- (1977).
- [11] M. Lamehi-Rachti, W. Mittig, Quantum mechanics and hidden variables: A test of Bell's inequality by the measurement of the spin correlation in low-energy proton-proton scattering, *Phys. Rev. D* **14**, 2543 (1976).
 - [12] J. Barrett, L. Hardy, A. Kent, No signaling and quantum key distribution, *Phys. Rev. Lett.* **95**, 010503 (2005).
 - [13] A. Acín, N. Brunner, N. Gisin, S. Massar, S. Pironio, V. Scarani, Device-independent security of quantum cryptography against collective attacks, *Phys. Rev. Lett.* **98**, 230501 (2007).
 - [14] L. Masanes, S. Pironio, A. Acín, Secure device-independent quantum key distribution with causally independent measurement devices, *Nat Commun* **2**, 238 (2011).
 - [15] S. Pironio, A. Acin, S. Massar, A. B. de la Giroday, D. N. Matsukevich, P. Maunz, S. Olmschenk, D. Hayes, L. Luo, T. A. Manning, C. Monroe, Random numbers certified by bell's theorem, *Nature* **464**, 1021 (2010).
 - [16] A. Aspect, J. Dalibard, G. Roger, Experimental test of Bell's inequalities using time-varying analyzers, *Phys. Rev. Lett.* **49**, 1804 (1982).
 - [17] G. Weihs, T. Jennewein, C. Simon, H. Weinfurter, A. Zeilinger, Violation of Bell's inequality under strict Einstein locality conditions, *Phys. Rev. Lett.* **81**, 5039 (1998).
 - [18] T. Scheidl, R. Ursin, J. Kofler, S. Ramelow, X. Ma, T. Herbst, L. Ratschbacher, A. Fedrizzi, N. Langford, T. Jennewein, A. Zeilinger, Violation of local realism with freedom of choice, *Proceedings of the National Academy of Sciences* **107**, 19708 (2010).
 - [19] A. Garg, N. D. Mermin, Detector inefficiencies in the Einstein-Podolsky-Rosen experiment, *Phys. Rev. D* **35**, 3831 (1987).
 - [20] M. A. Rowe, D. Kielpinski, V. Meyer, C. A. Sackett, W. M. Itano, C. Monroe, D. J. Wineland, Experimental violation of a Bell's inequality with efficient detection, *Nature* **409**, 791 (2001).
 - [21] M. Ansmann, H. Wang, R. C. Bialczak, M. Hofheinz, E. Lucero, M. Neeley, A. D. O'Connell, D. Sank, M. Weides, J. Wenner, A. N. Cleland, J. M. Martinis, Violation of Bell's inequality in Josephson phase qubits, *Nature* **461**, 504 (2009).

- [22] D. N. Matsukevich, P. Maunz, D. L. Moehring, S. Olmschenk, C. Monroe, Bell inequality violation with two remote atomic qubits, *Phys. Rev. Lett.* **100**, 150404 (2008).
- [23] J. Hofmann, M. Krug, N. Ortegel, L. Gérard, M. Weber, W. Rosenfeld, H. Weinfurter, Heralded entanglement between widely separated atoms, *Science* **337**, 72 (2012).
- [24] A. E. Lita, A. J. Miller, S. W. Nam, Counting near-infrared single-photons with 95% efficiency, *Opt. Express* **16**, 3032 (2008).
- [25] D. Fukuda, G. Fujii, T. Numata, K. Amemiya, A. Yoshizawa, H. Tsuchida, H. Fujino, H. Ishii, T. Itatani, S. Inoue, T. Zama, Titanium-based transition-edge photon number resolving detector with 98% detection efficiency with index-matched small-gap fiber coupling, *Opt. Express* **19**, 870 (2011).
- [26] A. E. Lita, B. Calkins, L. A. Pellouchoud, A. J. Miller, S. Nam, Superconducting transition-edge sensors optimized for high-efficiency photon-number resolving detectors, *Advanced Photon Counting Techniques IV* **7681**, 76810D (2010).
- [27] P. H. Eberhard, Background level and counter efficiencies required for a loophole-free Einstein-Podolsky-Rosen experiment, *Phys. Rev. A* **47**, R747 (1993).
- [28] A. Fedrizzi, T. Herbst, A. Poppe, T. Jennewein, A. Zeilinger, A wavelength-tunable fiber-coupled source of narrowband entangled photons, *Opt. Express* **15**, 15377 (2007).
- [29] E. Schrödinger, Die gegenwärtige Situation in der Quantenmechanik, *Naturwissenschaften* **23**, 823 (1935).
- [30] D. Bohm, *Quantum Theory*. Prentice Hall, New York (1951).
- [31] J. F. Clauser, M. A. Horne, Experimental consequences of objective local theories, *Phys. Rev. D* **10**, 526 (1974).
- [32] A. Fine, Hidden variables, joint probability, and the Bell inequalities, *Phys. Rev. Lett.* **48**, 291 (1982).
- [33] J. S. Bell, *Speakable and Unsayable in Quantum Mechanics*, pp. 232–248. Cambridge University Press (2004).
- [34] J. F. Clauser, M. A. Horne, A. Shimony, R. A. Holt, Proposed experiment to test local hidden-variable theories, *Phys. Rev. Lett.* **23**, 880 (1969).

- [35] J.-A. Larsson, J. Semitecolos, Strict detector-efficiency bounds for n-site Clauser-Horne inequalities, *Phys. Rev. A* **63**, 022117 (2001).
- [36] L. Hardy, Nonlocality for two particles without inequalities for almost all entangled states, *Phys. Rev. Lett.* **71**, 1665 (1993).
- [37] D. M. Greenberger, M. A. Horne, A. Zeilinger, *Bell's theorem, Quantum Theory, and Conceptions of the Universe*, chap. Going beyond Bell's Theorem. Kluwer Academic Publishers (1989).
- [38] A. Garuccio, Hardy's approach, Eberhard's inequality, and supplementary assumptions, *Phys. Rev. A* **52**, 2535 (1995).
- [39] G. Garbarino, Minimum detection efficiencies for a loophole-free observable-asymmetric Bell-type test, *Phys. Rev. A* **81**, 032106 (2010).
- [40] J. F. Clauser, A. Shimony, Bell's theorem. Experimental tests and implications, *Reports on Progress in Physics* **41**, 1881 (1978).
- [41] G. Weihs, *Ein Experiment zum Test der Bellschen Ungleichung unter Einsteinscher Lokalität*, Ph.D. thesis, Universität Wien (1999).
- [42] D. Bohm, Y. Aharonov, Discussion of experimental proof for the paradox of Einstein, Rosen, and Podolsky, *Phys. Rev.* **108**, 1070 (1957).
- [43] R. A. Holt, F. M. Pipkin, unpublished.
- [44] R. A. Holt, *Atomic Cascade Experiments*, Ph.D. thesis, Harvard University, Cambridge, Massachusetts (1973).
- [45] G. Faraci, D. Gutkowski, S. Notarrigo, A. Pennisi, An experimental test of the EPR paradox, *Lettere Al Nuovo Cimento (1971-1985)* **9**, 607 (1974).
- [46] A. Aspect, P. Grangier, G. Roger, Experimental tests of realistic local theories via Bell's theorem, *Phys. Rev. Lett.* **47**, 460 (1981).
- [47] A. Aspect, P. Grangier, G. Roger, Experimental realization of Einstein-Podolsky-Rosen-Bohm *Gedankenexperiment*: A new violation of Bell's inequalities, *Phys. Rev. Lett.* **49**, 91 (1982).
- [48] W. Perrie, A. J. Duncan, H. J. Beyer, H. Kleinpoppen, Polarization correlation of the two photons emitted by metastable atomic deuterium: A test of Bell's inequality, *Phys. Rev. Lett.* **54**, 1790 (1985).
- [49] T. Haji-Hassan, A. Duncan, W. Perrie, H. Beyer, H. Kleinpoppen, Experimental investigation of the possibility of enhanced photon detection in epr type

- experiments, *Physics Letters A* **123**, 110 (1987).
- [50] Y. H. Shih, C. O. Alley, New type of Einstein-Podolsky-Rosen-Bohm experiment using pairs of light quanta produced by optical parametric down conversion, *Phys. Rev. Lett.* **61**, 2921 (1988).
- [51] Z. Y. Ou, L. Mandel, Violation of Bell's inequality and classical probability in a two-photon correlation experiment, *Phys. Rev. Lett.* **61**, 50 (1988).
- [52] J. G. Rarity, P. R. Tapster, Experimental violation of Bell's inequality based on phase and momentum, *Phys. Rev. Lett.* **64**, 2495 (1990).
- [53] J. Brendel, E. Mohler, W. Martienssen, Experimental test of Bell's inequality for energy and time, *EPL (Europhysics Letters)* **20**, 575 (1992).
- [54] P. G. Kwiat, A. M. Steinberg, R. Y. Chiao, High-visibility interference in a Bell-inequality experiment for energy and time, *Phys. Rev. A* **47**, R2472 (1993).
- [55] E. Santos, Critical analysis of the empirical tests of local hidden-variable theories, *Phys. Rev. A* **46**, 3646 (1992).
- [56] P. G. Kwiat, P. H. Eberhard, A. M. Steinberg, R. Y. Chiao, Proposal for a loophole-free Bell inequality experiment, *Phys. Rev. A* **49**, 3209 (1994).
- [57] J. Clarke, F. K. Wilhelm, Superconducting quantum bits, *Nature* **453**, 1031 (2008).
- [58] M. Żukowski, A. Zeilinger, M. A. Horne, A. K. Ekert, "Event-ready-detectors" Bell experiment via entanglement swapping, *Phys. Rev. Lett.* **71**, 4287 (1993).
- [59] P. M. Pearle, Hidden-variable example based upon data rejection, *Phys. Rev. D* **2**, 1418 (1970).
- [60] N. Gisin, B. Gisin, A local hidden variable model of quantum correlation exploiting the detection loophole, *Physics Letters A* **260**, 323 (1999).
- [61] N. Brunner, N. Gisin, V. Scarani, C. Simon, Detection loophole in asymmetric Bell experiments, *Phys. Rev. Lett.* **98**, 220403 (2007).
- [62] A. Cabello, J.-A. Larsson, Minimum detection efficiency for a loophole-free atom-photon Bell experiment, *Phys. Rev. Lett.* **98**, 220402 (2007).
- [63] W. Rosenfeld, M. Weber, J. Volz, F. Henkel, M. Krug, A. Cabello, M. Żukowski, H. Weinfurter, Towards a loophole-free test of Bell's inequality with entangled pairs of neutral atoms, *Advanced Science Letters* **2**, 469 (2009).

- [64] H. Weinfurter, Experimental Bell-state analysis, *EPL (Europhysics Letters)* **25**, 559 (1994).
- [65] S. L. Braunstein, A. Mann, Measurement of the Bell operator and quantum teleportation, *Phys. Rev. A* **51**, R1727 (1995).
- [66] M. Michler, K. Mattle, H. Weinfurter, A. Zeilinger, Interferometric Bell-state analysis, *Phys. Rev. A* **53**, R1209 (1996).
- [67] J. S. Bell, *Speakable and Unspeakable in Quantum Mechanics*, pp. 105–110. Cambridge University Press (2004).
- [68] M. Freyberger, P. K. Aravind, M. A. Horne, A. Shimony, Proposed test of Bell's inequality without a detection loophole by using entangled Rydberg atoms, *Phys. Rev. A* **53**, 1232 (1996).
- [69] B. J. Oliver, C. R. J. Stroud, Bell's inequalities for Rydberg atoms, *J. Opt. Soc. Am. B* **4**, 1426 (1987).
- [70] E. S. Fry, T. Walther, S. Li, Proposal for a loophole-free test of the Bell inequalities, *Phys. Rev. A* **52**, 4381 (1995).
- [71] D. L. Moehring, M. J. Madsen, B. B. Blinov, C. Monroe, Experimental Bell inequality violation with an atom and a photon, *Phys. Rev. Lett.* **93**, 090410 (2004).
- [72] C. Simon, W. T. M. Irvine, Robust long-distance entanglement and a loophole-free Bell test with ions and photons, *Phys. Rev. Lett.* **91**, 110405 (2003).
- [73] N. Sangouard, J.-D. Bancal, N. Gisin, W. Rosenfeld, P. Sekatski, M. Weber, H. Weinfurter, Loophole-free Bell test with one atom and less than one photon on average, *Phys. Rev. A* **84**, 052122 (2011).
- [74] R. García-Patrón, J. Fiurášek, N. J. Cerf, Loophole-free test of quantum nonlocality using high-efficiency homodyne detectors, *Phys. Rev. A* **71**, 022105 (2005).
- [75] R. García-Patrón, J. Fiurášek, N. J. Cerf, J. Wenger, R. Tualle-Brouri, P. Grangier, Proposal for a loophole-free Bell test using homodyne detection, *Phys. Rev. Lett.* **93**, 130409 (2004).
- [76] H. Nha, H. J. Carmichael, Proposed test of quantum nonlocality for continuous variables, *Phys. Rev. Lett.* **93**, 020401 (2004).

- [77] T. Vértesi, S. Pironio, N. Brunner, Closing the detection loophole in Bell experiments using qudits, *Phys. Rev. Lett.* **104**, 060401 (2010).
- [78] N. Brunner, N. Gisin, Partial list of bipartite Bell inequalities with four binary settings, *Physics Letters A* **372**, 3162 (2008).
- [79] G. Brida, M. Genovese, C. Novero, E. Predazzi, New experimental test of Bell inequalities by the use of a non-maximally entangled photon state, *Physics Letters A* **268**, 12 (2000).
- [80] J. R. Torgerson, D. Branning, C. H. Monken, L. Mandel, Experimental demonstration of the violation of local realism without Bell inequalities, *Physics Letters A* **204**, 323 (1995).
- [81] A. G. White, D. F. V. James, P. H. Eberhard, P. G. Kwiat, Nonmaximally entangled states: Production, characterization, and utilization, *Phys. Rev. Lett.* **83**, 3103 (1999).
- [82] N. D. Mermin, Quantum mysteries refined, *American Journal of Physics* **62**, 880 (1994).
- [83] L. Hardy, Nonlocality of a single photon revisited, *Phys. Rev. Lett.* **73**, 2279 (1994).
- [84] D. Boschi, F. D. Martini, G. D. Giuseppe, Test of the violation of local realism in quantum mechanics without Bell inequalities, *Physics Letters A* **228**, 208 (1997).
- [85] G. Di Giuseppe, F. De Martini, D. Boschi, Experimental test of the violation of local realism in quantum mechanics without Bell inequalities, *Phys. Rev. A* **56**, 176 (1997).
- [86] M. Barbieri, F. D. Martini, G. D. Nepi, P. Mataloni, Towards a test of non-locality without “supplementary assumptions”, *Physics Letters A* **334**, 23 (2005).
- [87] M. Barbieri, C. Cinelli, F. De Martini, P. Mataloni, Test of quantum nonlocality by full collection of polarization entangled photon pairs, *The European Physical Journal D - Atomic, Molecular, Optical and Plasma Physics* **32**, 261 (2005).
- [88] T. Kim, M. Fiorentino, F. N. C. Wong, Phase-stable source of polarization-entangled photons using a polarization Sagnac interferometer, *Phys. Rev. A* **73**, 012316 (2006).

- [89] R. Boyd, *Nonlinear Optics*. Academic Press, 2nd edn. (1991).
- [90] T. H. Maiman, Stimulated optical radiation in ruby, *Nature* **187**, 493 (1960).
- [91] J. A. Armstrong, N. Bloembergen, J. Ducuing, P. S. Pershan, Interactions between light waves in a nonlinear dielectric, *Phys. Rev.* **127**, 1918 (1962).
- [92] P. A. Franken, J. F. Ward, Optical harmonics and nonlinear phenomena, *Rev. Mod. Phys.* **35**, 23 (1963).
- [93] K. Kato, E. Takaoka, Sellmeier and thermo-optic dispersion formulas for KTP, *Appl. Opt.* **41**, 5040 (2002).
- [94] S. Emanuelli, A. Arie, Temperature-dependent dispersion equations for KTiOPO_4 and KTiOAsO_4 , *Appl. Opt.* **42**, 6661 (2003).
- [95] W. P. Risk, T. R. Gosnell, A. V. Nurmikko, *Compact Blue-Green Lasers*. Cambridge University Press (2003).
- [96] M. M. Fejer, G. A. Magel, D. H. Jundt, R. L. Byer, Quasi-phase-matched second harmonic generation: tuning and tolerances, *IEEE Journal of Quantum Electronics* **28**, 2631 (1992).
- [97] H. Karlsson, *Fabrication of periodically poled crystals from the KTP family and their applications in nonlinear optics*, Ph.D. thesis, The Royal Institute of Technology, Stockholm, Sweden (1999).
- [98] A. Fedrizzi, *Fundamental experiments with a high brightness source of entangled photons*, Ph.D. thesis, Universität Wien (2008).
- [99] O. Gühne, G. Tóth, Entanglement detection, *Physics Reports* **474**, 1 (2009).
- [100] R. Horodecki, P. Horodecki, M. Horodecki, K. Horodecki, Quantum entanglement, *Rev. Mod. Phys.* **81**, 865 (2009).
- [101] S. Hill, W. K. Wootters, Entanglement of a pair of quantum bits, *Phys. Rev. Lett.* **78**, 5022 (1997).
- [102] W. K. Wootters, Entanglement of formation of an arbitrary state of two qubits, *Phys. Rev. Lett.* **80**, 2245 (1998).
- [103] W. K. Wootters, Entanglement of formation and concurrence, *Quantum Information and Computation* **1**, 27 (2001).
- [104] G. G. Stokes, On the composition and resolution of streams of polarized light from different sources, *Trans. Cambridge Philos. Soc.* **9**, 399 (1852).

- [105] D. F. V. James, P. G. Kwiat, W. J. Munro, A. G. White, Measurement of qubits, *Phys. Rev. A* **64**, 052312 (2001).
- [106] R. H. Hadfield, Single-photon detectors for optical quantum information applications, *Nat Photon* **3**, 696 (2009).
- [107] M. D. Eisaman, J. Fan, A. Migdall, S. V. Polyakov, Invited review article: Single-photon sources and detectors, *Review of Scientific Instruments* **82**, 071101 (2011).
- [108] C. M. Natarajan, M. G. Tanner, R. H. Hadfield, Superconducting nanowire single-photon detectors: physics and applications, *Superconductor Science and Technology* **25**, 063001 (2012).
- [109] K. Irwin, G. Hilton, In: *Cryogenic Particle Detection*, ed. C. Enss, vol. 99 of *Topics in Applied Physics*, pp. 81–97. Springer Berlin / Heidelberg (2005).
- [110] F. Marsili, F. Najafi, E. Dauler, F. Bellei, X. Hu, M. Csete, R. J. Molnar, K. K. Berggren, Single-photon detectors based on ultranarrow superconducting nanowires, *Nano Letters* **11**, 2048 (2011).
- [111] V. Verma, F. Marsili, B. Baek, A. Lita, T. Gerrits, J. Stern, R. Mirin, S. W. Nam, 55% system detection efficiency with self-aligned WSi superconducting nanowire single photon detectors, *CLEO: QELS-Fundamental Science* p. QTu1E.5 (2012).
- [112] E. A. Dauler, A. J. Kerman, B. S. Robinson, J. K. W. Yang, B. Voronov, G. Gol'tsman, S. A. Hamilton, K. K. Berggren, Photon-number-resolution with sub-30-ps timing using multi-element superconducting nanowire single photon detectors, *Journal of Modern Optics* **56**, 364 (2009).
- [113] K. M. Rosfjord, J. K. W. Yang, E. A. Dauler, A. Kerman, V. Anant, B. M. Voronov, G. N. Gol'tsman, K. K. Berggren, Nanowire single-photon detector with an integrated optical cavity and anti-reflection coating, *Opt. Express* **14**, 527 (2006).
- [114] F. Marsili, V. B. Verma, J. A. Stern, S. Harrington, A. E. Lita, T. Gerrits, I. Vayshenker, B. Baek, M. D. Shaw, R. P. Mirin, S. W. Nam, Detecting single infrared photons with 93% system efficiency, *arXiv:1209.5774* (2012).
- [115] W. Pernice, C. Schuck, O. Minaeva, M. Li, G. N. Gol'tsman, A. V. Sergienko, H. X. Tang, High speed and high efficiency travelling wave single-photon detectors embedded in nanophotonic circuits, *arXiv:1108.5299v2* (2011).

- [116] H. K. Onnes, The resistance of pure mercury at helium temperatures, *Commun. Phys. Lab. Univ. Leiden* **12**, 120 (1911).
- [117] J. Bardeen, L. N. Cooper, J. R. Schrieffer, Microscopic theory of superconductivity, *Phys. Rev.* **106**, 162 (1957).
- [118] J. Bardeen, L. N. Cooper, J. R. Schrieffer, Theory of superconductivity, *Phys. Rev.* **108**, 1175 (1957).
- [119] C. Poole, H. Farach, R. Creswick, R. Prozorov, *Superconductivity*. Elsevier Science & Technology (2007).
- [120] W. Meissner, R. Ochsenfeld, Ein neuer Effekt bei Eintritt der Supraleitfähigkeit, *Naturwissenschaften* **21**, 787 (1933).
- [121] D. Fukuda, G. Fujii, T. Numata, A. Yoshizawa, H. Tsuchida, H. Fujino, H. Ishii, T. Itatani, S. Inoue, T. Zama, Photon number resolving detection with high speed and high quantum efficiency, *Metrologia* **46**, S288 (2009).
- [122] L. Lolli, E. Taralli, M. Rajteri, Ti/Au TES to discriminate single photons, *Journal of Low Temperature Physics* **167**, 803 (2012).
- [123] A. E. Lita, B. Calkins, L. A. Pellochoud, A. J. Miller, S. Nam, High-efficiency photon-number-resolving detectors based on hafnium transition-edge sensors, *AIP Conference Proceedings* **1185**, 351 (2009).
- [124] S. Smith, J. Adams, C. Bailey, S. Bandler, J. Chervenak, M. Eckart, F. Finkbeiner, R. Kelley, C. Kilbourne, F. Porter, J. Sadleir, Small pitch transition-edge sensors with broadband high spectral resolution for solar physics, *Journal of Low Temperature Physics* **167**, 168 (2012).
- [125] S. Hatakeyama, M. Ohno, R. T. Damayanthi, H. Takahashi, Y. Kuno, N. Iyomoto, K. Maehata, C. Otani, T. Usui, T. Onishi, H. Obayashi, K. Takasaki, Development of hard X-ray and gamma-ray spectrometer using superconducting transition edge sensor, *Radiation Measurements* (2012), in press.
- [126] A. J. Miller, S. W. Nam, J. M. Martinis, A. V. Sergienko, Demonstration of a low-noise near-infrared photon counter with multiphoton discrimination, *Applied Physics Letters* **83**, 791 (2003).
- [127] D. Fukuda, G. Fujii, T. Numata, K. Amemiya, A. Yoshizawa, H. Tsuchida, H. Fujino, H. Ishii, T. Itatani, S. Inoue, T. Zama, Titanium superconducting photon-number-resolving detector, *IEEE Transactions on Applied Superconductivity* **21**, 241 (2011).

- [128] D. Rosenberg, S. W. Nam, A. J. Miller, A. Salminen, E. Grossman, R. E. Schwall, J. M. Martinis, Near-unity absorption of near-infrared light in tungsten films, *Nuclear Instruments and Methods in Physics Research Section A: Accelerators, Spectrometers, Detectors and Associated Equipment* **520**, 537 (2004), Proceedings of the 10th International Workshop on Low Temperature Detectors.
- [129] D. Rosenberg, A. Lita, A. Miller, S. Nam, R. Schwall, Performance of photon-number resolving transition-edge sensors with integrated 1550 nm resonant cavities, *IEEE Transactions on Applied Superconductivity* **15**, 575 (2005).
- [130] K. D. Irwin, An application of electrothermal feedback for high resolution cryogenic particle detection, *Applied Physics Letters* **66**, 1998 (1995).
- [131] B. Calkins, A. E. Lita, A. E. Fox, S. W. Nam, Faster recovery time of a hot-electron transition-edge sensor by use of normal metal heat-sinks, *Applied Physics Letters* **99**, 241114 (2011).
- [132] A. Lamas-Linares, N. Tomlin, B. Calkins, A. E. Lita, T. Gerrits, J. Beyer, R. Mirin, S. W. Nam, Transition edge sensors with low jitter and fast recovery times, p. 203 (2012), 11th International Conference on Quantum Communication, Measurement and Computing.
- [133] D. Fukuda, G. Fujii, T. Numata, A. Yoshizawa, H. Tsuchida, S. Inoue, T. Zama, Titanium TES based photon number resolving detectors with 1 MHz counting rate and 65 % quantum efficiency, vol. 7236, p. 72360C. SPIE (2009).
- [134] D. F. Santavicca, F. W. Carter, D. E. Prober, Proposal for a GHz count rate near-IR single-photon detector based on a nanoscale superconducting transition edge sensor, *Proc. SPIE* **8033**, 80330W (2012).
- [135] A. J. Miller, A. E. Lita, B. Calkins, I. Vayshenker, S. M. Gruber, S. W. Nam, Compact cryogenic self-aligning fiber-to-detector coupling with losses below one percent, *Opt. Express* **19**, 9102 (2011).
- [136] J. Clarke, A. I. Braginski (eds.), *The SQUID Handbook: Fundamentals and Technology of SQUIDs and SQUID Systems, Volume I*. Wiley-VCH Verlag GmbH & Co. KGaA (2005).
- [137] J.-H. Storm, *Untersuchung der Hochfrequenzeigenschaften von SQUID-Stromsensoren*, Diploma thesis, Fachhochschule Brandenburg, Germany (2008).

- [138] R. C. Jaklevic, J. Lambe, A. H. Silver, J. E. Mercereau, Quantum interference effects in Josephson tunneling, *Phys. Rev. Lett.* **12**, 159 (1964).
- [139] A. H. Silver, J. E. Zimmerman, Quantum states and transitions in weakly connected superconducting rings, *Phys. Rev.* **157**, 317 (1967).
- [140] B. Josephson, Possible new effects in superconductive tunnelling, *Physics Letters* **1**, 251 (1962).
- [141] P. W. Anderson, J. M. Rowell, Probable observation of the Josephson superconducting tunneling effect, *Phys. Rev. Lett.* **10**, 230 (1963).
- [142] S. Shapiro, Josephson currents in superconducting tunneling: The effect of microwaves and other observations, *Phys. Rev. Lett.* **11**, 80 (1963).
- [143] R. Feynman, R. Leighton, M. Sands, In: *The Feynman lectures on physics*, vol. 3. Addison-Wesley (1965).
- [144] D. Drung, C. Assmann, J. Beyer, A. Kirste, M. Peters, F. Ruede, T. Schurig, Highly sensitive and easy-to-use SQUID sensors, *IEEE Transactions on Applied Superconductivity* **17**, 699 (2007).
- [145] J. Beyer, D. Drung, A SQUID series array dc current sensor, *Superconductor Science and Technology* **21**, 095012 (2008).
- [146] D. Drung, High-performance dc SQUID read-out electronics, *Physica C: Superconductivity* **368**, 134 (2002).
- [147] D. Drung, C. Hinrichs, H.-J. Barthelmeß, Low-noise ultra-high-speed dc SQUID readout electronics, *Superconductor Science and Technology* **19**, S235 (2006).
- [148] K. Uhlig, $^3\text{He}/^4\text{He}$ dilution refrigerator with pulse-tube refrigerator precooling, *Cryogenics* **42**, 73 (2002).
- [149] V. K. Pecharsky, K. A. Gschneidner Jr, Magnetocaloric effect and magnetic refrigeration, *Journal of Magnetism and Magnetic Materials* **200**, 44 (1999).
- [150] E. Warburg, Magnetische Untersuchungen, *Annalen der Physik* **249**, 141 (1881).
- [151] P. Debye, Einige Bemerkungen zur Magnetisierung bei tiefer Temperatur, *Annalen der Physik* **386**, 1154 (1926).
- [152] W. F. Giaque, A thermodynamic treatment of certain magnetic effects. a proposed method of producing temperatures considerably below 1° absolute,

Journal of the American Chemical Society **49**, 1864 (1927).

- [153] M. Giustina, et al. in preparation.
- [154] R. Jozsa, Fidelity for mixed quantum states, *Journal of Modern Optics* **41**, 2315 (1994).
- [155] R. F. Werner, Quantum states with Einstein-Podolsky-Rosen correlations admitting a hidden-variable model, *Phys. Rev. A* **40**, 4277 (1989).
- [156] B. Lounis, M. Orrit, Single-photon sources, *Reports on Progress in Physics* **68**, 1129 (2005).
- [157] S. A. Castelletto, R. E. Scholten, Heralded single photon sources: a route towards quantum communication technology and photon standards, *The European Physical Journal - Applied Physics* **41**, 181 (2008).
- [158] N. Gisin, G. Ribordy, W. Tittel, H. Zbinden, Quantum cryptography, *Rev. Mod. Phys.* **74**, 145 (2002).
- [159] V. Scarani, H. Bechmann-Pasquinucci, N. J. Cerf, M. Dušek, N. Lütkenhaus, M. Peev, The security of practical quantum key distribution, *Rev. Mod. Phys.* **81**, 1301 (2009).
- [160] E. Knill, R. Laflamme, G. J. Milburn, A scheme for efficient quantum computation with linear optics, *Nature* **409**, 46 (2001).
- [161] H. J. Briegel, D. E. Browne, W. Dur, R. Raussendorf, M. Van den Nest, Measurement-based quantum computation, *Nat Phys* pp. 19–26 (2009).
- [162] P. Kok, W. J. Munro, K. Nemoto, T. C. Ralph, J. P. Dowling, G. J. Milburn, Linear optical quantum computing with photonic qubits, *Rev. Mod. Phys.* **79**, 135 (2007).
- [163] J. Rarity, P. Owens, P. Tapster, Quantum random-number generation and key sharing, *Journal of Modern Optics* **41**, 2435 (1994).
- [164] A. Stefanov, N. Gisin, O. Guinnard, L. Guinnard, H. Zbinden, Optical quantum random number generator, *Journal of Modern Optics* **47**, 595 (2000).
- [165] J. G. Rarity, K. D. Ridley, P. R. Tapster, Absolute measurement of detector quantum efficiency using parametric downconversion, *Appl. Opt.* **26**, 4616 (1987).
- [166] A. L. Migdall, R. U. Datla, A. Sergienko, J. S. Orszak, Y. H. Shih, Absolute detector quantum-efficiency measurements using correlated photons, *Metrologia*

- 32**, 479 (1995).
- [167] T. B. Pittman, B. C. Jacobs, J. D. Franson, Single photons on pseudodemand from stored parametric down-conversion, *Phys. Rev. A* **66**, 042303 (2002).
- [168] E. Jeffrey, N. A. Peters, P. G. Kwiat, Towards a periodic deterministic source of arbitrary single-photon states, *New Journal of Physics* **6**, 100 (2004).
- [169] A. L. Migdall, D. Branning, S. Castelletto, Tailoring single-photon and multiphoton probabilities of a single-photon on-demand source, *Phys. Rev. A* **66**, 053805 (2002).
- [170] J. H. Shapiro, F. N. Wong, On-demand single-photon generation using a modular array of parametric downconverters with electro-optic polarization controls, *Opt. Lett.* **32**, 2698 (2007).
- [171] E. R. Abraham, E. A. Cornell, Teflon feedthrough for coupling optical fibers into ultrahigh vacuum systems, *Appl. Opt.* **37**, 1762 (1998).
- [172] S. Gröblacher, *Quantum opto-mechanics with micromirrors: combining nano-mechanics with quantum optics*, Ph.D. thesis, Universität Wien (2010).
- [173] D. H. Smith, G. Gillett, M. P. de Almeida, C. Branciard, A. Fedrizzi, T. J. Weinhold, A. Lita, B. Calkins, T. Gerrits, H. M. Wiseman, S. W. Nam, A. G. White, Conclusive quantum steering with superconducting transition-edge sensors, *Nat Commun* **3**, 625 (2012).
- [174] D. Drung, M. Mück, *SQUID Electronics*, pp. 127–170. Wiley-VCH Verlag GmbH & Co. KGaA (2005).
- [175] Magnicon GmbH, Lemsahler Landstr. 171, 22397 Hamburg, Germany, *High performance dc SQUID electronics XXF-1 Manual* (2010).
- [176] B. Wittmann, S. Ramelow, F. Steinlechner, N. K. Langford, N. Brunner, H. M. Wiseman, R. Ursin, A. Zeilinger, Loophole-free Einstein-Podolsky-Rosen experiment via quantum steering, *New Journal of Physics* **14**, 053030 (2012).
- [177] T. Jennewein, U. Achleitner, G. Weihs, H. Weinfurter, A. Zeilinger, A fast and compact quantum random number generator, *Review of Scientific Instruments* **71**, 1675 (2000).

Acknowledgments

It would not have been possible to write this dissertation without the help and support of the people around me. I would especially like to thank:

The Austrian Science Foundation (FWF) under projects SFB-FOQUS (No. F4008-N16) and CoQuS (No. W1210-N16), the European Commission under the projects QIT4QAD (ERC Advanced Grant No. 227844), QAP (No. 15848) and the Marie Curie Research Training Network EMALI (No. MRTN-CT-2006-035369) for the financial support.

Professor Zeilinger for the opportunity to join his interesting group and to work on this challenging project. I am grateful for his support and advice, but also for the offered chances to meet outstanding people within and outside physics.

Many for their administrative help, amongst them: Daniela Charlesworth, Verena Bock, Alexander Gutschner, Manuela Csapo, Andrea Aglibut, Ursula Machold, Aylin Majetic, Petra Beckmannova, Sonja Redl, Martina Monghy, Miriam Lotz-Scheibenpflug.

The people behind the CoQuS program, especially Professor Markus Arndt, Christiane M. Losert-Valiente Kroon and Canan Göser for their help and support.

Michael Taraba, Gerhard Mondl, and Martin Aspöck for their technical help.

The excellent one man workshop of the IQOQI Roland Blach for his work.

Jörn Beyer and Marco Schmidt from PTB Berlin, Germany and Sae Woo Nam, Adriana Lita, Thomas Gerrits, and many more from NIST, Boulder, USA for providing the SQUIDs and transition-edge sensors as well as for their support on the detection system.

Professor Aspelmeyer and his group, especially Simon Gröblacher and Witlef Wieczorek, for the time in their lab and support with the dilution refrigerator.

My colleagues for helpful discussions and assistance, especially:

Bernhard Wittmann for his invaluable support, his patient work on the source and the measurement of the fluorescence; Marissa Giustina for her counting programs, her assistance in installation of the ADR, TESs and SQUIDs and the cooperation on the publication on heralding; Sven Ramelow for the assistance on the optimization program for nonmaximally entangled states and cooperation on the publication on heralding; Xiaosong Ma, Thomas Herbst and co-authors of the publication on teleportation for the opportunity to be a free-spacer; Rupert Ursin for his help and advice.

My family, friends and colleagues for the cumbersome proof-reading.

My colleagues from IQOQI and university who were more than just colleagues not only for all the talking, laughing, morning meetings, movies, Easter walks and picnics, opera visits and parties but also their support at work.

All my friends for what they are for me.

My family for being ready to help at any time and for their unceasing encouragement.

Jan Macke for sharing the good and the bad times.

CURRICULUM VITAE

EDUCATION

- 2008 – Doctoral studies of Natural Sciences
Universität Wien, Austria
- 2000 – 2008 Diploma studies of Physics
Technische Universität Darmstadt, Germany
- 1999 – 2000 Diploma studies of Physics
Johannes Gutenberg-Universität Mainz, Germany
- 1996 – 1999 Abitur (comparable to A-levels) in Darmstadt, Germany

FELLOWSHIPS

- 2008 – Vienna Doctoral Program on Complex Quantum Systems
(CoQuS)
- 2010 – 2011 Marie Curie Research Training Network “Engineering, Manipulation and Characterization of Quantum States of Matter and Light” (EMALI)

PUBLICATIONS

Published

X.-S. Ma, T. Herbst, T. Scheidl, D. Wang, S. Kropatschek, W. Naylor, B. Wittmann, A. Mech, J. Kofler, E. Anisimova, V. Makarov, T. Jennewein, R. Ursin, A. Zeilinger, Quantum teleportation over 143 kilometres using active feed-forward, *Nature* **489**, 269 (2012).

In preparation

S. Ramelow, A. Mech, M. Giustina, S. Groöblacher, W. Wiczorek, A. Lita, B. Calkins, T. Geritts, S. W. Nam, A. Zeilinger, and R. Ursin, Highly-efficient heralding of entangled single photons.